nature portfolio

Peer Review File

Enhancing Film Bulk Acoustic Resonators Performance by Optimizing AlN Seed Layer Crystallinity and Polarity Alignment

Corresponding Author: Dr Yao Cai

This file contains all reviewer reports in order by version, followed by all author rebuttals in order by version.

Version 0:

Reviewer comments:

Reviewer #1

(Remarks to the Author)
In this work, the authors present an approach to improve the overall filter performance of ScAlN based FBAR filters by first adding a MOCVD seed layer of AlN to enhance the ScAlN thin film quality and then subsequently removing the layer to increase the electromechanical coupling. Overall, the work does have merit and the results are interesting, however I recommend transfer of the manuscript to a more topical journal after a revision.

In any case, there are several issues I have with this work that would need to be addressed prior to publication (major revision, as additional experimental data is needed):

1) Multiple claims in need of references: lines 62-64, 76-77 (polariy inversion), 103, 114-117
2) The authors use a stack of Mo/AlN/ScAlN, which leads to a decrease in coupling since the contribution of AlN will bring the coupling down compared to a pure ScAlN layer (in addition to the claimed polarity inversion). Why not use a stack of AlN/Mo/ScAlN, which is quite common and would remove the issue of AlN removal completely?
3) Line 155 "destructive interference" is the wrong wording in this context
4) Line 157: "When _ exceeds..." - there is a symbol or word missing
5) Line 181: A FWHM of 4.5° is quite bad and well below the state of the art, so it is not suitable for a comparison with the MOCVD layers. Either remove the PVD samples completely or improve the quality of the samples for a more fair comparison.
6) Lines 202-205: The claim about the grain structure is not really supported by the SEM images due to the blurry image. A FIB cut might be a better choice here. Also, both figures should be taken at the same sample angle.
7) Line 211: What is meant by "no significant abrupt changes in stress..."?
8) Fig. 3b: While the polarity is nicely visible for the ScAlN, in the AlN, the case is not so clear. Arguably, the opposite polarisation would also fit the image as shown. The rest of the data supports the claim of polarity inversion, however, the TEM image by itself does not. Is there any other data to support this? What is the reason for this inversion (see above, missing references)?
9) Optimization strategy: Removal of the AlN layer is used to optimize the device, however this step requires a layer transfer step, which is typically something to avoid. Why not target different optimization routes such as minimizing AlN seed layer thickness as much as possible and optimizing the AlN/ScAlN interface to avoid polarity inversion? What is the benefit of this approach for applications (since 5G and 6G are specifically mentioned as application scenarios)?
10) FBAR1 - 3: FBAR1 is MOCVD AlN + ScAlN, FBAR2 is ScAlN with the PVD AlN seed removed and FBAR3 is ScAlN with the MOCVD AlN seed removed. A sample with PVD AlN seed + ScAlN is missing, especially if the impact of poly vs. single crystalline seeds is to be studied.
11) Poly vs. single crystalline: This is claimed, but not supported by the data. Why is the MOCVD AlN layer single crystalline, a FWHM of 0.94° does not imply this without other supporting data.
12) Lines 335-337: Acoustic confinement by the AlN layer: Please elaborate, as the acoustic impedance mismatch between AlN and ScAlN is not large. Why would there be any relevant acoustic confinement. In fact, would this not be bad, as it might deterioate the frequency response?
13) Fig 5: Why are there 2 S ports? The device schematic shows a single input port. Are both S ports connected?
14) Line 520: How is selectivity achieved for etching AlN on top of ScAlN? Is an etch monitoring method used to stop the

process as soon as the ScAlN layer is reached?
15) Fig. S2: The rocking curve of AlN barely shows any signal, are you sure, the layer is crystalline at all? Show the Bragg Brentano spectrum.

Reviewer #2

(Remarks to the Author)
Comments:
The manuscript entitled “Enhancing ScAlN-Based FBAR Performance via MOCVD-AlN Seed Layer Crystallinity Optimization and Polarity Inversion Elimination for Sub-7GHz Applications”introduced a dual-optimization strategy aimed at improving the performance of ScAlN-based Film Bulk Acoustic Resonators (FBARs) by addressing both crystal quality and polarity alignment. First, the single
crystalline AlN seed layer was introduced MOCVD to significantly improve the microstructure of Sc0.2Al0.8N film and the AlN seed layer was removed subsequently in post-processing to eliminate the polarity inversion at the AlN/ScAlN interface. While the core concept of eliminating polarization reversal through the removal of the AlN seed layer is innovative, several critical issues within the manuscript necessitate thorough revision prior to consideration for publication. The current submission suffers from a lack of methodological clarity, insufficient experimental validation for pivotal claims, and a need for more comprehensive data presentation.

Specific Points Requiring Major Revision:
1. Removal of AlN Seed Layer: The central claim of the manuscript revolves around removing the single-crystal AlN seed layer to enhance the piezoelectric properties of the ScAlN layer due to the cancellation of piezoelectricity when both layers with opposite polarization are present. However, the manuscript fails to describe the methodology or process used for the removal of this single
crystal AlN seed layer. This is a critical omission that undermines the reproducibility and understanding of the presented work. This process also appears to be missing from the fabrication process flow in Figure S5 and the corresponding optical microscopy images in Figure S6.

2. Experimental Validation of Piezoelectric Properties Model: The manuscript presents a simplified model calculating the piezoelectric characteristics as a function of layer thickness for the AlN/ScAlN bilayer structure. However, there is a significant lack of experimental data to support and validate this model. The manuscript claims that integrating ScAlN on an AlN seed layer with opposite polarity causes a pronounced degradation in d33, Kt2,and keff2,and that even with aligned polarization, performance declines with an increasing AlN fraction. This core assertion requires robust experimental validation, not just calculation results.

3. Filter Data and Comparability: The manuscript introduces three stacked filter structures but does not provide specific structural parameters for each layer of FBARs. Furthermore,there is no comparison with simulation data of filters.The manuscript needs to provide detailed layer parameters for the three compared filters in Figure 5 and explain the large frequency discrepancies observed. Additionally, a comparison between simulated and measured results for the fabricated filters in Figure 5 is missing.

4. Calculation of Piezoelectric Coefficients: The manuscript needs to clearly describe the process for calculating the piezoelectric stress coefficient shown in Figure 1c. Additionally, as Equation 10 indicates that the calculation of the effective electromechanical coupling coefficient (keff2) requires resonant and anti-resonant frequencies, the method for obtaining these values must be
detailed.

5. Euler Angles and Polarization: In line 488, the manuscript states, "Polarization orientation is controlled by assigning Euler angles to each layer." A clear explanation of how Euler angles affect polarization orientation isrequired. Furthermore, the role and meaning of the (0,180°,0) Euler angles depicted on the right side of Figure S1c need to be clarified, as the 180° rotation is not evident from the figure.

6. Acoustic Confinement by AlN Seed Layer: Figure 4e's caption mentions, "The presence of the intact AlN seed layer provides additional acoustic confinement, thereby suppressing energy dissipation." It is recommended to include simulation results in the manuscript to substantiate the claim that the
single-crystal AlN layer confines energy dissipation.

7. Discrepancy in Electromechanical Coupling Coefficients and Filter Bandwidth: In Figure 4d, FBAR 2 and FBAR 3, which correspond to resonators with the polycrystalline AlN and single-crystalline AlN seed layer removed respectively, exhibit almost identical effective electromechanical coupling coefficients. However, the filters based on these resonators (Figures 5e and 5f, corresponding to the removal of polycrystalline AlN and single crystalline AlN, respectively) show a very large difference in bandwidth. The reasons for this significant discrepancy need to be thoroughly explained.

8. Polarity Inversion in ScAlN: Regarding Figure 1 (Crystal structure, polarization characteristics, and piezoelectric properties of AlN and ScAlN films), the manuscript should clarify the conditions under which the polarity of ScAlN inverts. The implication that any minor Sc doping would cause polarity flipping requires further physical justification.

9. Comparison of AlN Seed Layers: For Figure S2, which compares X-ray rocking curves of AlN seed layers deposited by PVD and MOCVD, it would be beneficial to also compare the crystallinity of MOCVD-grown AlN with thin Mo electrode as

the guide layer versus MOCVD-grown AlN directly on Si.

10. Filter Performance Benchmarking: The reported lattice-type filter demonstrates a center frequency of 6.4 GHz, a minimum insertion loss of -2.6 dB, a 3 dB bandwidth of 740 MHz, and out-of-band rejection exceeding 40 dB. When compared to the metrics of existing ScAlN filter, the insertion loss and bandwidth of the presented device do not appear to offer a significant advantage. This should be discussed.

Specific Points Requiring Minor Revision:
1. Atomic Structure Labeling: The atomic structure of ScAlN labeled in Fig. 1b appears to be that of ScN. This needs to be corrected.

Reviewer #3 (Remarks to the Author):

In this manuscript, the authors significantly improved the crystalline quality of low-temperature PVD-grown ScAlN films by introducing an AlN single-crystal seed layer grown by MOCVD. Combined with theoretical model analysis, film characterization, and FBAR device verification, they elucidate the effects of the quality and polarity of the AlN seed layer on the microstructure and electromechanical coupling characteristics of the ScAlN films. This work provides a feasible and scalable technical path for realizing high-performance wideband filters in the frequency band below 7 GHz. This manuscript needs to be revised before it can be accepted for publication. The questions are as follows:

1. For the variation of piezoelectric constants in ScAlN films with Sc concentration shown in Figure 1c, please explain the calculation method used.

2. Note that in Figure 1e, for antiparallel polarization, the electromechanical coupling coefficient K^2_t of the composite film approaches zero near v1/v2=0.6, while the simulated effective electromechanical coupling coefficient k^2_{eff} of the FBAR remains non-zero. Conversely, at v1/v2=1.0, K^2_t increases to 6%, yet the simulated k^2_{eff} of the FBAR is nearly zero. Please explain the relationship between k^2_{eff} and K^2_t, and the reasons for the above contradiction.

3. For Figure 2i, it is recommended to include comparative data with the results reported in: "Chen, Zhipeng, et al. High-Performance Film Bulk Acoustic Resonator and Filter Based on an Al0.8Sc0.2N Film Prepared by a Low-Temperature Staged Deposition Method. IEEE Transactions on Electron Devices 72.1, 383-389(2025). ".

4. On Line 293, "obtained by cutting along the slice line in Fig. 5a" should be corrected to "obtained by cutting along the slice line in Fig. 4b".

5. During the fabrication of FBAR2 and FBAR3, when removing the AlN seed layer via ICP etching, how was over-etching into the AlScN layer prevented?

6. For FBAR1 with v1/v2=50/280=0.18 in the final test results (in Fig. 4d), the measured k^2_{eff} is 6%, while the FEM simulation in Figure 1e predicts $k^2_{eff} \approx 9\%$. Please explain why the experimentally measured k^2_{eff} is lower than the simulated value.

Version 1:

REVIEWERS' COMMENTS

Reviewer #1 (Remarks to the Author):

The authors have addressed all issues voiced by myself and the other reviewers in a very extensive and in my opinion sufficient and complete way. The manuscript has improved significantly and is now much clearer. I do not have addiitonal objections against a publication in the current state.

I recommend to accept the manuscript for publication.

Reviewer #2 (Remarks to the Author):

The authors have provided detailed and targeted responses to the comments raised by this reviewer (Reviewer 2). In particular, their explanations for comments 7 and 8 are reasonable and sufficient, and the remaining points have been appropriately revised and supplemented. Overall, the authors have adequately addressed the review comments, and the quality of the manuscript has been significantly improved. I recommend acceptance of the manuscript.

Reviewer #3 (Remarks to the Author):

I have reviewed the revised manuscript and find that the authors have adequately addressed my previous comments. I have no additional suggestions and recommend the manuscript for acceptance.

Reviewer #4 (Remarks to the Author):

The authors have addressed all my concerns in detail and revised the manuscript accordingly. Therefore, I recommend to accept the paper in the actual version.

Response to reviewers for the manuscript (NCOMMS-25-29647)

Dear Reviewers,

We sincerely thank all reviewers for their thorough reading of our manuscript and their constructive comments and concerns. These have been diligently addressed point-by-point below. For the reviewers' convenience, **comments and suggestions** are listed in **standard black font**, followed by **our responses** in **blue font**. **Corresponding modifications in the revised manuscript** are tracked in **red font**. We believe the reviewers' questions highlighted areas requiring further attention, and our modifications have significantly improved the manuscript. We sincerely appreciate the opportunity to revise our manuscript and believe the revised version now meets the high standards of ***Nature Communications***.

Best regards,

Dr. Yao Cai On behalf of all authors

Reviewer's Comments and Author's Response

Reviewer #1 (Remarks to the Author):

Expertise: piezo thin films, resonators, AlN and SiC based devices

In this work, the authors present an approach to improve the overall filter performance of ScAlN based FBAR filters by first adding a MOCVD seed layer of AlN to enhance the ScAlN thin film quality and then subsequently removing the layer to increase the lectromechanical coupling. Overall, the work does have merit and the results are interesting, however I recommend transfer of the manuscript to a more topical journal after a revision.

In any case, there are several issues I have with this work that would need to be addressed prior to publication (major revision, as additional experimental data is needed).

Response to Reviewer:

We sincerely appreciate the reviewer's recognition of our work's merit and interesting results. With regard to the suggestion to transfer the manuscript to a more specialized journal, we respectfully believe that the fundamental breakthrough of this work, which resolves the inherent conflict between crystallinity optimization and polarity-induced performance degradation, has broad implications for piezoelectric devices beyond FBARs (e.g., MEMS resonators, energy harvesters).

To further support this, 1) we enhanced our original model with DFT-calculated characteristics and Mori-Tanaka modeling, quantitatively predicting K_t^2 degradation due to polarity mismatch. 2) Newly added cross-sectional HRTEM directly visualizes polarity inversion at the AlN/ScAlN layers confirming theoretical predictions. 3) And our methodology establishes a rigorous multiscale validation framework that integrates theoretical prediction, atomic-scale characterization, and device-level verification. Theoretical modeling quantitatively predicts polarization-induced degradation, which is confirmed by atomic-resolution cross-sectional STEM revealing the polarity reversal from Al-polar AlN to N-polar ScAlN. At the device level, FBAR-3 achieves a k_{eff}^2 of 13.2% and a FOM of 97, both in close agreement with the theoretical recovery threshold. This end-to-end integration of predictive modeling, interfacial analysis, and experimental validation bridges fundamental materials design with device optimization, providing a general framework for piezoelectric heterostructure engineering.

We emphasize that our dual-optimization strategy represents a new paradigm for addressing the fundamental trade-offs in piezoelectric heterostructures by integrating theoretical insight, atomic-scale structural validation, and device-level demonstration. This interdisciplinary approach aligns precisely with ***Nature Communications***' scope of publishing high-impact research bridging materials science and device engineering. Notably, several related studies on AlN/ScAlN films or acoustic resonators and filters have also been published in ***Nature Communications*** in recent years, underscoring the relevance of our work to the journal's readership.

1. Mondal, S., et al. Unprecedented enhancement of piezoelectricity of wurtzite nitride semiconductors via thermal annealing. ***Nature Communications*** 16, 4130 (2025).
2. Wang, J., *et al*. Unveiling interfacial dead layer in wurtzite ferroelectrics. ***Nature Communications*** 16, 6069 (2025).
3. Giribaldi, Gabriel, *et al*. Compact and wideband nanoacoustic pass-band filters for future 5G and 6G cellular radios. ***Nature communications*** 15, 304 (2024).
4. Gokhale, Vikrant J., *et al*. Epitaxial bulk acoustic wave resonators as highly coherent multi-phonon sources for quantum acoustodynamics. ***Nature communications*** 11, 2314 (2020).

1) Multiple claims in need of references: lines 62-64, 76-77 (polariy inversion), 103, 114-117

Response to Reviewer:

We appreciate the reviewer's constructive comment. The corresponding references have been added to support the related statements, and the descriptions have been revised accordingly. In addition, more literature relevant to this study has been incorporated to further strengthen the discussion.

Revised Main Text:

Line 70 (original Line 62-64): Despite these advantages, the addition of Sc leads to increased surface roughness and degraded crystallographic orientation, which adversely affect device performance[17,18].

Line 77 (original Line 76-77): Film polarity is a key factor that strongly affects the atomic arrangement and interfacial quality of piezoelectric layers, thereby influencing device performance[26,28]. Although polarity control has been demonstrated, it remains a complex process influenced by multiple growth parameters[23–25,27,29,30].

Line 110 (original Line 103): The substitution of smaller Al atoms with larger Sc atoms induces anisotropic lattice distortion, primarily manifested as an expansion of the *a*-axis and a concurrent contraction of the *c*-axis[16].

Line 119 (original Line 114-117): In AlN and ScAlN films, especially AlN/ScAlN bilayer structures essential for FBARs, the piezoelectric response is critically dependent on the polarity alignment between layers[26,30].

2) The authors use a stack of Mo/AlN/ScAlN, which leads to a decrease in coupling since the contribution of AlN will bring the coupling down compared to a pure ScAlN layer (in addition to the claimed polarity inversion). Why not use a stack of AlN/Mo/ScAlN, which is quite common and would remove the issue of AlN removal completely?

Response to Reviewer:

We acknowledge that in the Mo/AlN/ScAlN stack configuration with retained AlN, the interfacial AlN layer inevitably reduces effective electromechanical coupling (k_{eff}^2) versus a pure ScAlN structure. However, this architecture is essential for leveraging MOCVD-grown epitaxial single-crystalline AlN seed layers on Si (111), which enable high-quality *c*-axis oriented ScAlN growth and consequently high-*Q* FBARs. Critically, AlN's hexagonal symmetry achieves excellent lattice matching with Si (111) triangular surface lattice (**Fig. R1**), whereas Mo bcc structure exhibits rectangular symmetry in its (110) plane. This structural incompatibility prevents commensurate epitaxial alignment for wurtzite AlN/ScAlN. Direct ScAlN nucleation on polycrystalline Mo, which would occur if Mo were positioned between AlN and ScAlN, resulting in significantly degraded crystallinity.

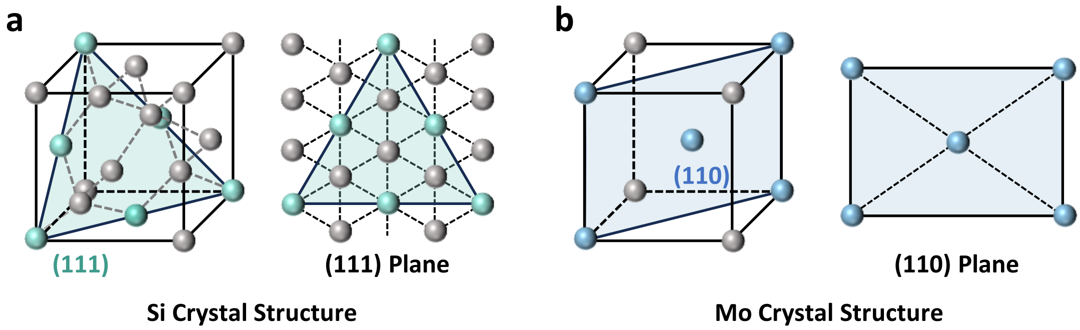

Fig. R1 Crystal structures of Si (111) and Mo (110) planes. a Si has a diamond-cubic structure, and the (111) plane exhibits an equilateral triangular lattice. **b** Mo has a body-centered cubic (bcc) structure, and the (110) plane exhibits a rectangular lattice.

(1) Thin-film quality comparison

During the initial stage of thin-film development we systematically examined the influence of Mo and AlN seed layers on the crystalline quality of ScAlN.

As shown in **Fig. R2**, four samples were fabricated for comparison. In Sample 1 (**Fig. R2a**), a 60 nm-thick Mo electrode was sputtered on Si, followed by 280 nm-thick ScAlN. In Sample 2 (**Fig. R2b**), a 50 nm-thick PVD AlN seed layer and a 60 nm-thick Mo electrode were sputtered sequentially on Si, followed by 280 nm-thick ScAlN. In Sample 3 (**Fig. R2c**), a 50 nm-thick MOCVD AlN seed layer was epitaxially grown on Si, on top of which a 60 nm-thick Mo electrode and 280 nm-thick ScAlN were deposited. In Sample 4 (**Fig. R2d**), a 50 nm-thick MOCVD AlN seed layer was epitaxially grown on Si, followed directly by 280 nm ScAlN without Mo. The X-ray rocking-curve FWHM values were 2.6°, 2.3°, 1.4°, and 0.94°, respectively. These results clearly show that direct epitaxy of ScAlN on MOCVD AlN yields the best crystalline quality (FWHM 0.94°), which is the approach adopted in this work.

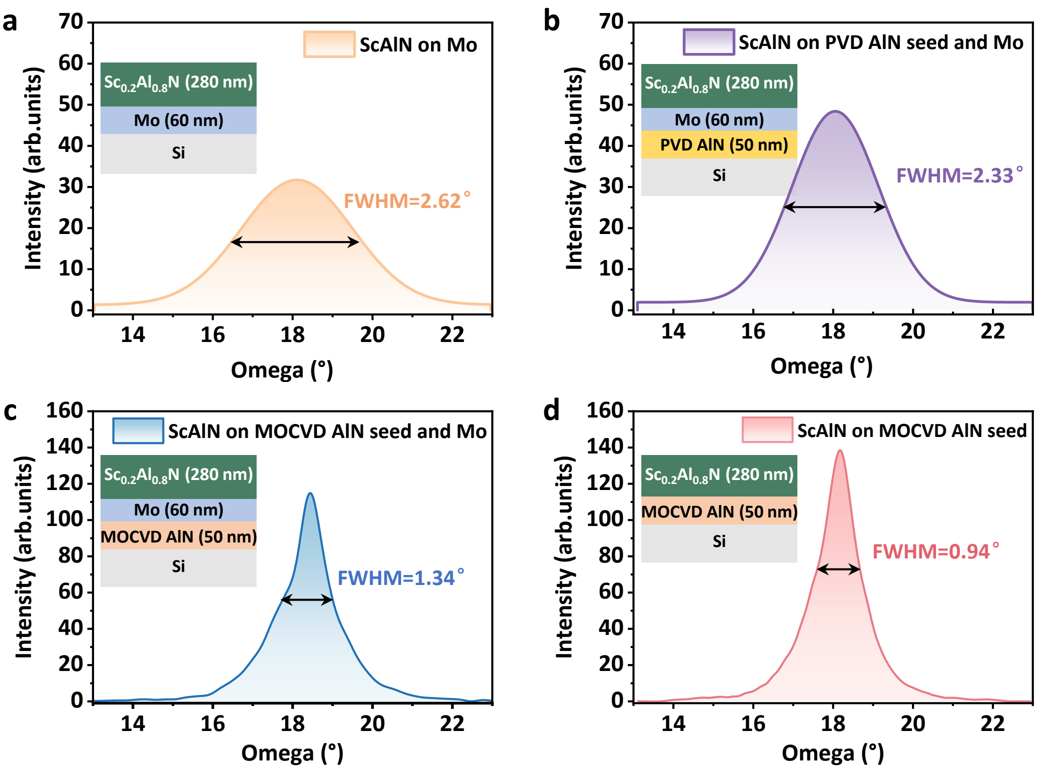

Fig. R2 (Fig. S6 in the newly revised Supplementary Information) Rocking curve of the 280 nm-thick $Sc_{0.2}Al_{0.8}N$ film. a 280 nm-thick $Sc_{0.2}Al_{0.8}N$ deposited on a 60 nm-thick Mo layer on Si, FWHM = 2.62°. **b** 280 nm-thick $Sc_{0.2}Al_{0.8}N$ deposited on 60 nm-thick Mo with a 50 nm-thick PVD AlN seed layer on Si, FWHM = 2.33°. **c** 280 nm-thick $Sc_{0.2}Al_{0.8}N$ deposited on 60 nm-thick Mo with a 50 nm-thick MOCVD AlN seed layer on Si, FWHM = 1.34°. **d** 280 nm-thick $Sc_{0.2}Al_{0.8}N$ deposited directly on a 50 nm-thick MOCVD AlN seed layer on Si without Mo, FWHM = 0.94°.

(2) Device performance comparison

Our prior work explored FBARs based on the AlN/Mo/ScAlN stack, yet their quality factors remained constrained. For instance, Ref. [1] reported a 4.3 GHz FBAR with this configuration achieving Q_s=150, Q_p=318, and a figure of merit (FOM) of 62. In contrast, by leveraging epitaxial AlN/ScAlN films and a thin-film transfer process, our optimized FBAR-3 devices operating at 6.4 GHz attained significantly enhanced values of Q_s=192, Q_p=719, and a FOM of 97. These results confirm that single-crystalline AlN films provide superior epitaxial templating, thereby improving ScAlN crystalline quality and ultimately enhancing resonator Q factors.

To avoid a decrease in K_t^2 while obtaining a higher Q value, we developed and validated an etching process to selectively remove the AlN seed layer after transfer when required. Using inductively coupled plasma (ICP) etching with in-situ optical emission spectroscopy (OES) endpoint detection, we reliably identify the transition from AlN to ScAlN through the change in reaction-product emission intensity. This non-destructive method ensures precise termination at the interface without damaging the underlying ScAlN, and has been demonstrated to be both repeatable and reliable.

In conclusion, the single-crystalline AlN seed layer enables high-quality ScAlN growth with enhanced Q factors, while selective removal of this seed layer achieves favorable polarity alignment and restores high k_{eff}^2 and Q values. This dual-optimization approach provides an effective and reliable pathway for optimizing high-frequency FBAR performance.

Relevant thin film development data and corresponding descriptions for AlN/Mo/ScAlN stacks have been incorporated in both the main text and Supplementary Information.

Revised Supplementary Information:

Line 255:

Effect of Mo electrode and AlN seed layers on ScAlN crystallinity

As shown in **Fig. S6**, XRD rocking curves of the (002) reflection exhibit variations in the FWHM values among the samples. The ScAlN film grown directly on Mo exhibits a broad FWHM of 2.62°, indicating relatively poor crystallinity due to the polycrystalline nature and lattice mismatch at the Mo/ScAlN interface. When a PVD AlN seed layer is introduced between Mo and ScAlN, the FWHM decreases to 2.33°, suggesting partial improvement in orientation. A more substantial enhancement is observed for ScAlN deposited on a MOCVD AlN seed layer. The FWHM is reduced to 1.34° when a Mo electrode is present, and further decreases to 0.94° when ScAlN is directly grown on MOCVD AlN without Mo. These results demonstrate that the presence and crystallinity of the AlN seed layer play a decisive role in promoting highly *c*-axis oriented ScAlN growth. In particular, the single-crystalline MOCVD AlN template provides an optimal lattice environment and effectively suppresses grain-tilt dispersion, leading to the best overall film quality. Therefore, the subsequent section investigates the crystalline quality of AlN seed layers prepared by PVD and MOCVD.

References

1. Zou, Y., Gao, C., Zhou, J., Liu, Y., Xu, Q., Qu, Y., Liu, W., Woon Soon, J. B., Cai, Y. & Sun, C. Aluminum scandium nitride thin-film bulk acoustic resonators for 5G wideband applications. *Microsyst. Nanoeng.* 8, 124 (2022).

3) Line 155 "destructive interference" is the wrong wording in this context

Response to Reviewer:

The corresponding descriptions in the main text have been revised. Indeed, the term "destructive interference" may lead to misinterpretation. It refers specifically to phase cancellation phenomena. The relevant sections have been modified to "…cause partial cancellation of the electric field, thereby diminishing electromechanical coupling efficiency…"

Revised main text:

Line 322:

…In FBAR-1, the opposing polarities between the AlN seed layer and the $Sc_{0.2}Al_{0.8}N$ film cause partial cancellation of the electric field, thereby diminishing electromechanical coupling efficiency. Conversely, removing the AlN seed layer in FBAR-2 and FBAR-3 effectively alleviates the detrimental effects of polarity mismatch….

4) Line 157: “When _ exceeds...” - there is a symbol or word missing

Response to Reviewer:

We thank the reviewer for these constructive comments. A formula reference (v_1/v_2) appears to have been inadvertently omitted here, as we have modified all horizontal axis labels to $v_1/(v_1+v_2)$ in **Fig. 1d** and 1e accordingly. We are rigorously scrutinizing the revised manuscript to ensure no similar typographical errors remain.

Revised Main Text:

Line 147: …Conversely, antiparallel polarity induces the mutual cancellation of piezoelectric effects, causing d_{33}^{*} to decline sharply and even reverse sign when $v_1/(v_1+v_2)$ exceeds around 0.7…

5) Line 181: A FWHM of 4.5° is quite bad and well below the state of the art, so it is not suitable for a comparison with the MOCVD layers. Either remove the PVD samples completely or improve the quality of the samples for a more fair comparison.

Response to Reviewer:

The 4.5° FWHM observed for the 50 nm-thick PVD AlN seed layer exceeds optimal values reported for thicker AlN films, primarily reflecting inherent nucleation limitations in ultrathin layers rather than process deficiencies. Ultrathin films exhibit constrained nucleation sites and incomplete grain coalescence, compounded by insufficient stress relaxation mechanisms, which collectively cause orientation dispersion and broadened rocking curves. Progressive grain coalescence and partial dislocation annihilation with increasing thickness enhance *c*-axis alignment, yielding narrower FWHM values. This well-established thickness dependence of AlN (002) rocking curve FWHM is extensively documented in references [1-4] and visually confirmed in **Fig. R3b and 3d**, where disproportionately large FWHM values are evident for minimal PVD AlN thicknesses.

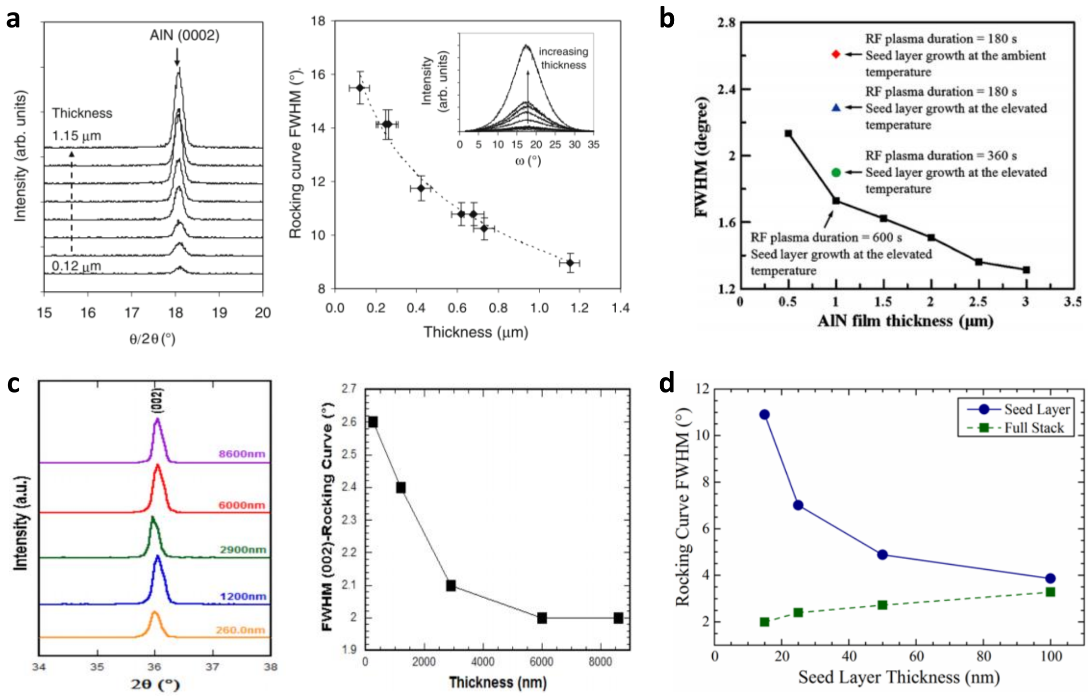

Fig. R3 Thickness dependence of the AlN (002) rocking curve FWHM reported in the literature, showing a decrease with increasing film thickness[1-4].

In our earlier work, a 770 nm-thick AlN film deposited under identical conditions exhibited a FWHM of 1.38° (**Fig. R4**), aligning with literature values. This conclusively demonstrates our deposition process is capable of producing high-quality AlN films, while the broader 4.5° FWHM observed for the 50 nm-thick PVD AlN layer is attributed to inherent limitations of ultrathin film growth (e.g., incomplete grain coalescence at 50 nm thickness). These results are consistent with **references [2-4]** documenting thickness-dependent FWHM broadening in nitride films.

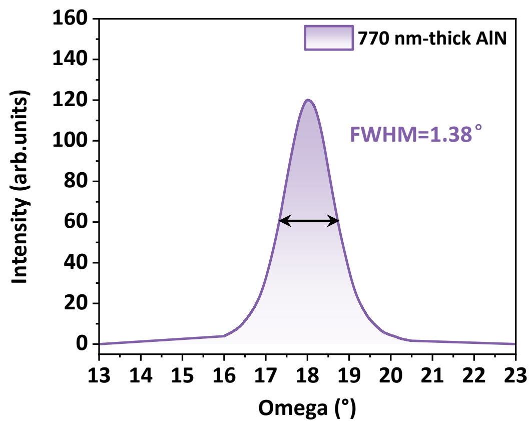

Fig. R4 X-ray rocking curve of the 770 nm-thick AlN film deposited on Si, with a FWHM of 1.38°.

XRD data for PVD and MOCVD AlN in **Fig. 2d** and **S4** respectively confirm (002) preferred orientation in both films, though thickness constraints substantially degrade PVD AlN crystallinity as evidenced by both XRD and rocking curve analyses. HRTEM/FFT assessment **(Fig. R5 a-c**) reveals lattice fringes along the *c*-axis in 50 nm PVD AlN, yet local bending and contrast variations manifest dislocations, strain, and lattice distortions. The FFT-derived reciprocal spacing of 7.98 nm^{-1} (**Fig. R5c**) corresponds to 0.25 nm real-space d-spacing, matching wurtzite AlN (002) planes, confirming preserved *c*-axis orientation despite broad FWHM, albeit with wider orientation distribution and heightened defect density.

This further demonstrates that, although the PVD AlN seed layer provides a certain degree of orientation guidance, its improvement effect is limited. **This limitation motivated the adoption of a high-quality MOCVD AlN seed layer in our subsequent work, which offers superior orientation uniformity and interface quality.** To present a more comprehensive comparison of the seed layers and their influence on ScAlN, HRTEM contrasts between PVD and MOCVD AlN seed layers have been added in the revised manuscript, as detailed below.

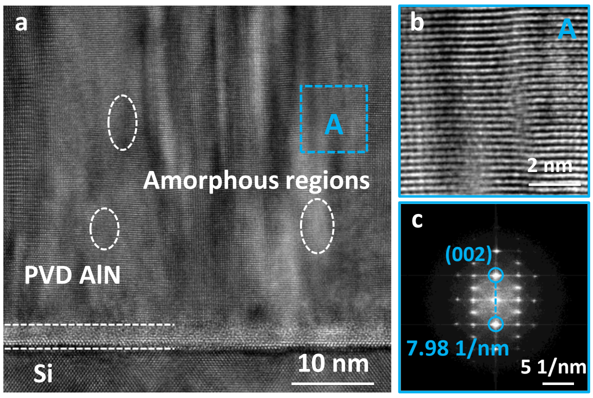

Fig. R5 HRTEM and FFT analysis of the PVD AlN seed layer. a Cross-sectional HRTEM image of the PVD AlN layer deposited on Si, showing lattice fringes predominantly aligned along the *c*-axis but with local bending and contrast variations. **b** Enlarged view of region A in panel a, highlighting local orientation dispersion of the lattice fringes. **c** FFT pattern from region A, exhibiting (002) reflections.

Revised Supplementary Information:

Line 182:

Comparison of PVD and MOCVD AlN seed layers

Two 50 nm-thick AlN seed layers are prepared on Si substrates by PVD and MOCVD to provide distinct crystallographic templates for subsequent $Sc_{0.2}Al_{0.8}N$ growth. The crystallinity is evaluated via X-ray rocking curves and high-resolution transmission electron microscopy (HRTEM)/Fast Fourier Transform (FFT) analyses. The PVD AlN exhibits a broad FWHM of 4.50° (**Fig. S4a**), HRTEM lattice fringes with local bending/contrast variations (**Fig. S4b**), and diffuse (002) FFT reflections, indicating polycrystallinity with dislocations and strain. Conversely, MOCVD AlN shows a narrow FWHM of 0.63° (**Fig. S4d**), highly ordered *c*-axis lattice fringes, and sharp symmetric (002) FFT spots (**Fig. S4e**), confirming superior single-crystalline quality.

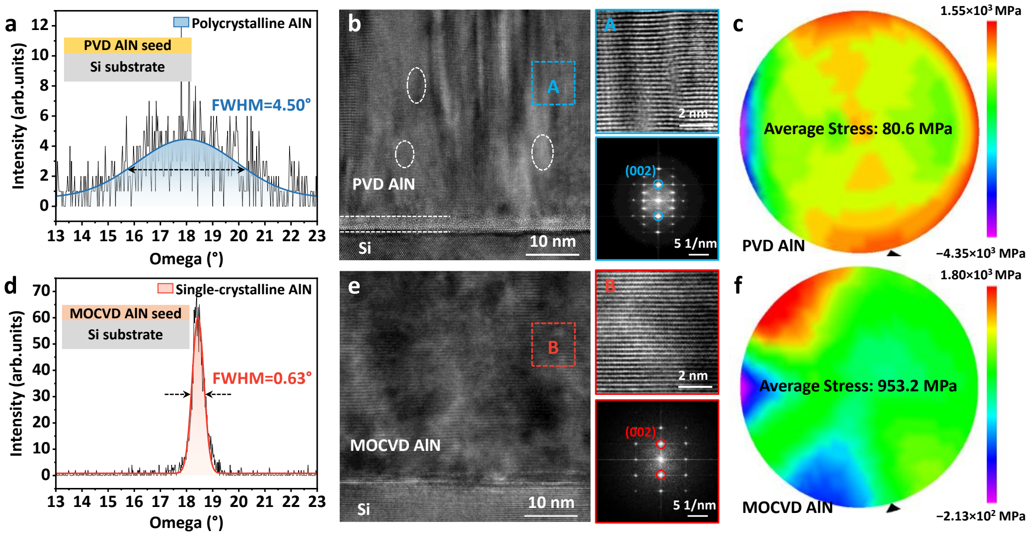

Fig. S4 Characterization of PVD and MOCVD deposited AlN seed layers. a Rocking curve for the (002) reflection of 50 nm-thick PVD AlN, showing a FWHM of 4.50°. **b** Cross-sectional HRTEM image of PVD AlN, including a magnified region (A) and corresponding fast FFT pattern. The lattice fringes are primarily *c*-axis oriented but exhibit local bending and contrast variations, while the FFT pattern displays slightly diffuse diffraction spots, consistent with a polycrystalline structure. **c** Residual stress map of the PVD AlN seed layer, with an average stress of ~81 MPa. **d** Rocking curve for the (002) reflection of 50 nm-thick MOCVD AlN, with a FWHM of 0.63°, characteristic of single-crystalline quality and excellent *c*-axis orientation. **e** Cross-sectional HRTEM image of MOCVD AlN, including a magnified region (B) and corresponding FFT pattern. The lattice fringes are highly ordered and continuous along the *c*-axis, and the FFT pattern shows a single set of sharp (002) diffraction spots (no polycrystalline rings), confirming a single-crystalline structure. **f** Residual stress map of the MOCVD AlN seed layer, with an average stress of ~953 MPa.

References

1. Sánchez, G., Abdallah, B., Tristant, P., Monnoyer, P., Jouan, P.-Y. & Boulmer-Leborgne, C. Microstructure and mechanical properties of AlN films obtained by plasma enhanced chemical

vapor deposition. *J. Mater. Sci.* 44, 6125–6134 (2009).
2. Howell, K. M., Bashir, W., De Pastina, A., Matloub, R., Muralt, P. & Villanueva, L. G. Effect of AlN seed layer on crystallographic characterization of piezoelectric AlN. *J. Vac. Sci. Technol. A* 37, 021504 (2019).
3. Aït Aïssa, K., Semmar, N., De Sousa Meneses, D., Le Brizoual, L., Gaillard, M., Petit, A., Jouan, P.-Y., Boulmer-Leborgne, C. & Djouadi, M. Thermal conductivity measurement of AlN films by fast photothermal method. *J. Phys.: Conf. Ser.* 395, 012089 (2012).
4. Lin, C.-M., Lien, W.-C., Felmetsger, V., Hopcroft, M., Senesky, D. & Pisano, A. AlN thin films grown on epitaxial 3C-SiC (100) for piezoelectric resonant devices. *Appl. Phys. Lett.* 97, 141907 (2010).

6) Lines 202-205: The claim about the grain structure is not really supported by the SEM images due to the blurry image. A FIB cut might be a better choice here. Also, both figures should be taken at the same sample angle.

Response to Reviewer:

Following this advice, we re-prepared the samples using focused ion beam (FIB) milling and conducted cross-sectional TEM analyses on all three types of films, as shown in **revised Figs. 2 g-i and Figs. S5 a-c.** When ScAlN is directly deposited on Si (**Fig. 2g**), the film develops a columnar morphology and the grains are irregular and randomly oriented. The grain boundaries appear curved and discontinuous, while local contrast fluctuations and stripe interruptions indicate a high density of dislocations and stacking faults, accompanied by a rough and incoherent interface. With the introduction of a PVD AlN seed layer (**Fig. 2h**), the seed itself exhibits a fine columnar structure that partially improves nucleation. The overgrown ScAlN shows more continuous and vertical columns than in the case of direct growth on Si, and the overall *c*-axis alignment is moderately enhanced, though grain-boundary waviness remains visible. In contrast, the MOCVD AlN seed layer forms a dense, epitaxial structure with a flat and well-defined interface, which provides an effective template for ScAlN growth (**Fig. 2i**). The ScAlN film exhibits a pronounced reduction in columnar stripe contrast, indicative of highly consistent *c*-axis orientation. Dislocations and defects are markedly reduced, and the interface appears flat and sharp, confirming a significant improvement in crystalline quality. In addition, selected-area electron diffraction (SAED) patterns and diffraction spot broadening measurements were conducted to further evaluate the crystallinity and degree of lattice alignment. These new data have been included in the revised manuscript and provide direct and quantitative evidence supporting the discussion of grain structure and interfacial coherence.

Revised Main Text:

Line 218:

Cross-sectional transmission electron microscopy (TEM) images (**Figs. 2 g-i**) reveal the microstructural evolution of $Sc_{0.2}Al_{0.8}N$ films deposited on different templates (additional characterization in **Fig. S5**). The film on Si (**Fig. 2g**) shows a columnar structure with pronounced contrast fluctuations, indicating poor crystallinity and high defect density, its selected area electron diffraction (SAED) pattern exhibits diffuse (002) spots with a broadening of 0.488 nm^{-1}, confirming polycrystallinity. With a polycrystalline AlN seed layer (**Fig. 2h**), the vertical grain orientation partially improves, though dislocations and misoriented regions persist. The ScAlN film corresponding SAED pattern shows moderately sharper (002) spots (broadening reduced to 0.445 nm^{-1}), indicating improved *c*-axis alignment. In contrast, the film on the MOCVD single-crystalline AlN seed layer (**Fig. 2i**) displays a highly aligned structure with low defect density, its SAED pattern features sharp (002) spots with minimal broadening (0.293 nm^{-1}), demonstrating epitaxial alignment and excellent *c*-axis orientation. Collectively, these findings collectively confirm that the MOCVD single-crystalline AlN seed layer significantly enhances film crystallinity, effectively promoting well-oriented ScAlN growth with reduced defect density, and is indispensable for depositing high-quality piezoelectric films.

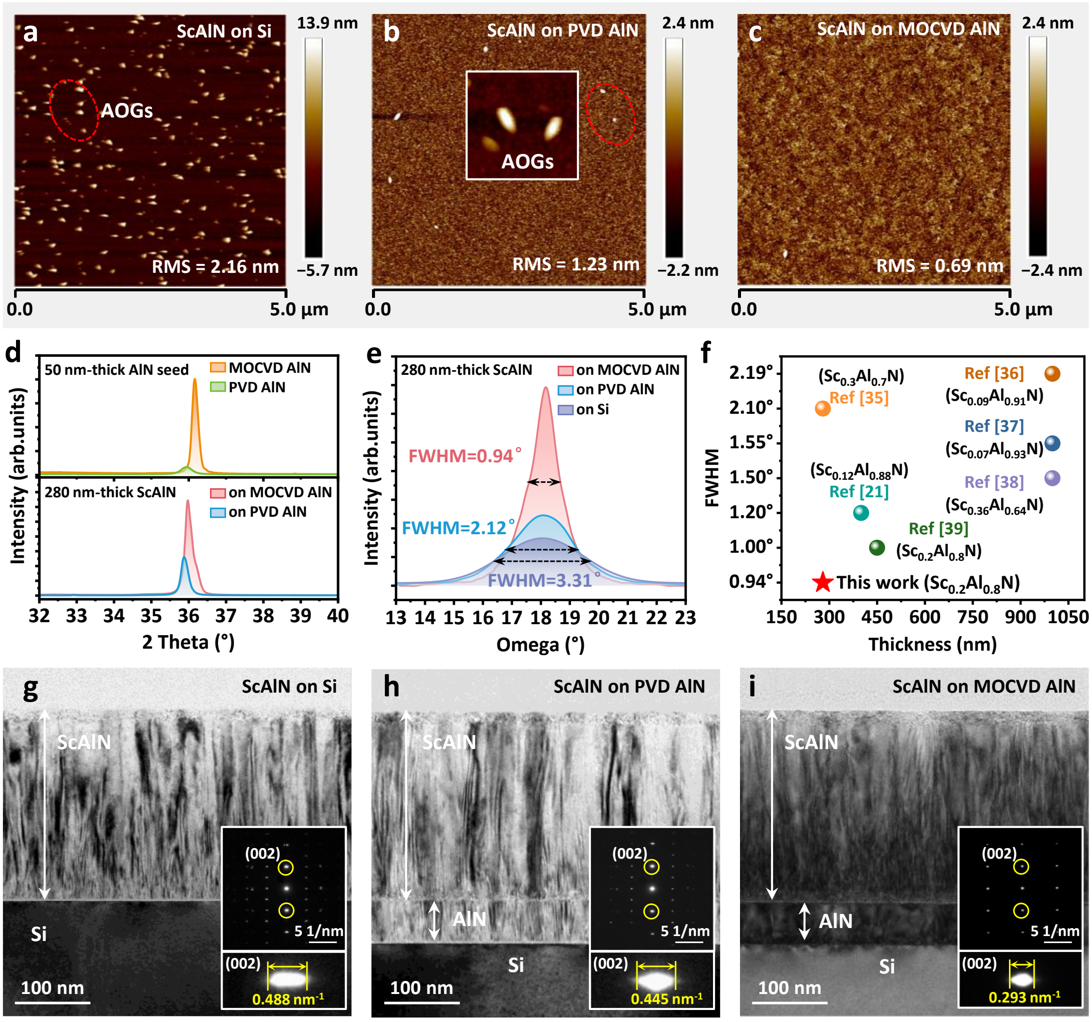

Fig. 2 Characterization of $Sc_{0.2}Al_{0.8}N$ film deposited on different substrates: Si, PVD and MOCVD AlN seed layer. g-i Cross-sectional TEM and corresponding SAED patterns.

Revised Supplementary Information:

Line 212:

Cross-sectional HRTEM images (**Figs. S5a-c**) reveal distinct interfacial structures for $Sc_{0.2}Al_{0.8}N$ films deposited on different substrates. When grown directly on Si (**Fig. S5a**), an amorphous transition layer forms at the interface, and the film exhibits discontinuous, distorted lattice fringes, indicating poor crystallinity. On the PVD AlN seed layer (**Fig. S5b**), the interfacial region appears disordered and polycrystalline, with multiple lattice orientations and poor boundary continuity. In contrast, $Sc_{0.2}Al_{0.8}N$ deposited on the MOCVD AlN seed layer (**Fig. S5c**) shows well-ordered, continuous lattice fringes across the interface, where the single-crystalline AlN template promotes coherent *c*-axis oriented growth and enhanced structural integrity.

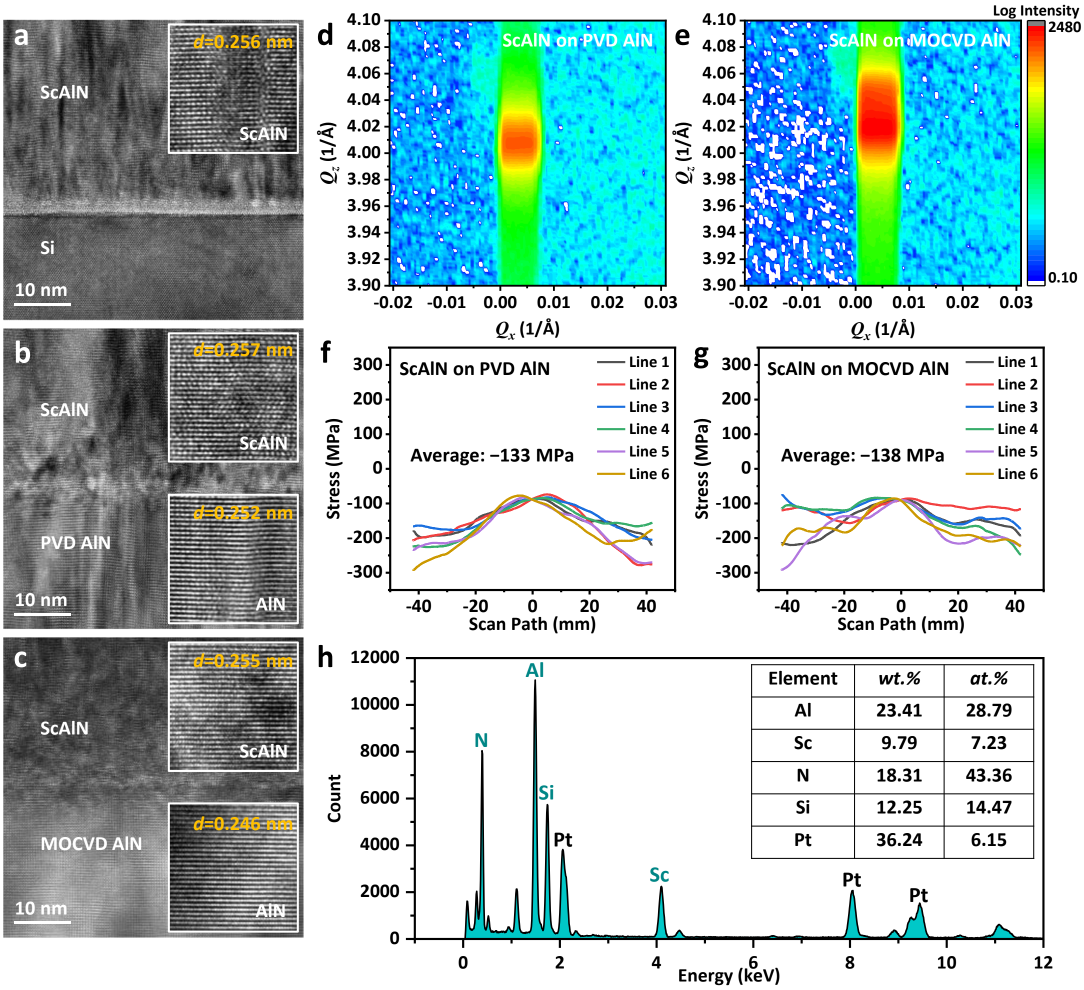

Fig. S5 Characterization of $Sc_{0.2}Al_{0.8}N$ film deposited on different substrates: Si, PVD and MOCVD AlN seed layer. a-c Cross-sectional HRTEM images highlighting the interfacial structures of $Sc_{0.2}Al_{0.8}N$ films deposited on different substrates. **a** $Sc_{0.2}Al_{0.8}N$ directly deposited on Si, showing an amorphous transition layer at the interface and locally disordered lattice regions. **b** $Sc_{0.2}Al_{0.8}N$ deposited on the PVD AlN seed layer, showing a disordered polycrystalline interface with multiple lattice orientations and poor structural continuity. Both AlN and ScAlN layers show partially distorted lattice fringes. **c** $Sc_{0.2}Al_{0.8}N$ deposited on the MOCVD AlN seed layer, exhibiting continuous and well-ordered (002) lattice fringes across the interface, indicating good structural continuity.

7) Line 211: What is meant by "no significant abrupt changes in stress..."?

Response to Reviewer:

We thank the reviewer for pointing this out. Our original wording was imprecise.

What we intended to convey is that the residual stress values of the $Sc_{0.2}Al_{0.8}N$ films grown on single-crystalline and polycrystalline AlN seeds are comparable, because the ScAlN thickness and deposition parameters were identical in both cases. In the revised manuscript, we have clarified the ambiguous sentence and relocated the stress analysis data to **Figs. S5f and S5g** (see **Comment (6)**) with additional supporting datasets. Furthermore, we have supplemented the residual stress distribution maps for both PVD and MOCVD AlN seed layers in **Figs. S4c and S4f** (see **Comment (5)**).

Revised Supplementary Information:

Line 192: The relevant description of Figs. S4c and S4f

…Residual stress mapping reveals an average stress of 81 MPa for PVD AlN (**Fig. S4c**) versus 953 MPa for MOCVD AlN (**Fig. S4f**). The higher stress in MOCVD AlN originates from thermal and epitaxial mismatch, which intensifies with thickness and can cause cracking.…

Line 225: The relevant description of Figs. 5f and 5g

…The residual stress distributions of the $Sc_{0.2}Al_{0.8}N$ films on different AlN seed layers (PVD and MOCVD) are shown in **Figs. S5f** and **S5g**, exhibiting compressive stress profiles with good uniformity across the wafer for both samples. The average stress values are −133 MPa for the film grown on the PVD AlN seed layer and −138 MPa for that on the MOCVD AlN seed layer. While the seed layers themselves possess distinct stress characteristics, the ScAlN film maintains a consistently low and uniform stress level, a key prerequisite for preserving structural integrity when the seed layer is removed in subsequent fabrication steps.…

8) Fig. 3b: While the polarity is nicely visible for the ScAlN, in the AlN, the case is not so clear. Arguably, the opposite polarisation would also fit the image as shown. The rest of the data supports the claim of polarity inversion, however, the TEM image by itself does not. Is there any other data to support this? What is the reason for this inversion (see above, missing references)?

Response to Reviewer:

As correctly pointed out, **Fig. 3b** in the original manuscript was acquired in the HAADF-STEM mode, where the image contrast mainly originates from atomic number (Z-contrast). Consequently, the signal from light elements such as nitrogen is relatively weak, making the polarity direction less distinct.

To provide a clearer identification of the polarity, we have supplemented the revised manuscript with iDPC-STEM images (see **revised Fig. 3c and Fig. 3e**). This imaging technique provides high-sensitivity phase contrast for both light and heavy elements, allowing the stacking sequence of Al and N atomic columns to be directly resolved. As shown in the images, the AlN seed layer exhibits an N-Al-N stacking sequence corresponding to Al-polarity (+*c* direction), whereas the overlying $Sc_{0.2}Al_{0.8}N$ film displays an Al-N-Al stacking sequence corresponding to N-polarity (−*c* direction), clearly revealing a polarity inversion at the interface.

In addition, to provide a more intuitive visualization of the lattice structure of each layer, we have re-acquired the HRTEM images for both the AlN seed layer and the $Sc_{0.2}Al_{0.8}N$ film. **Fig. 3** and the corresponding descriptions have been updated accordingly, and the revised content is provided below for your convenience.

Revised Main Text:

Line 245:

To understand the critical impact of crystal structure and polarity alignment on resonator performance in the AlN/ScAlN bilayer system, we employ HRTEM and integrated differential phase contrast scanning transmission electron microscopy (iDPC-STEM) to investigate the atomic configuration and polarity at the interface between the MOCVD AlN seed layer and the $Sc_{0.2}Al_{0.8}N$ film. Cross-sectional HRTEM imaging (**Fig. 3a**) reveals a sharp interface featuring a thin transition layer between the AlN seed and the overlying ScAlN film. High-magnification analysis of regions A and B (**Figs. 3b** and **3d**) show well-ordered (002) lattice fringes in both layers, with measured interplanar spacings of 0.246 nm for AlN and 0.255 nm for ScAlN, the latter's expansion confirming lattice distortion induced by Sc incorporation. Corresponding Fast Fourier transform (FFT) patterns exhibit clear, symmetric diffraction spots, verifying good crystallinity in both layers, the sharper reflections from the AlN seed layer indicate its superior single-crystalline quality. At atomic resolution, iDPC-STEM imaging distinctly resolves the stacking sequences of Al and N atomic columns, clearly demonstrating opposite polarities across the interface. The ScAlN layer exhibits N-polarity (−*c* direction) while the AlN seed layer maintains Al-polarity (+*c* direction) (**Figs. 3c** and **3e**). Significantly, despite this observed polarity reversal within the AlN/$Sc_{0.2}Al_{0.8}N$ bilayer, high-resolution TEM analysis reveals no evident lattice defects or structural discontinuities, indicating excellent epitaxial alignment and interfacial compatibility.

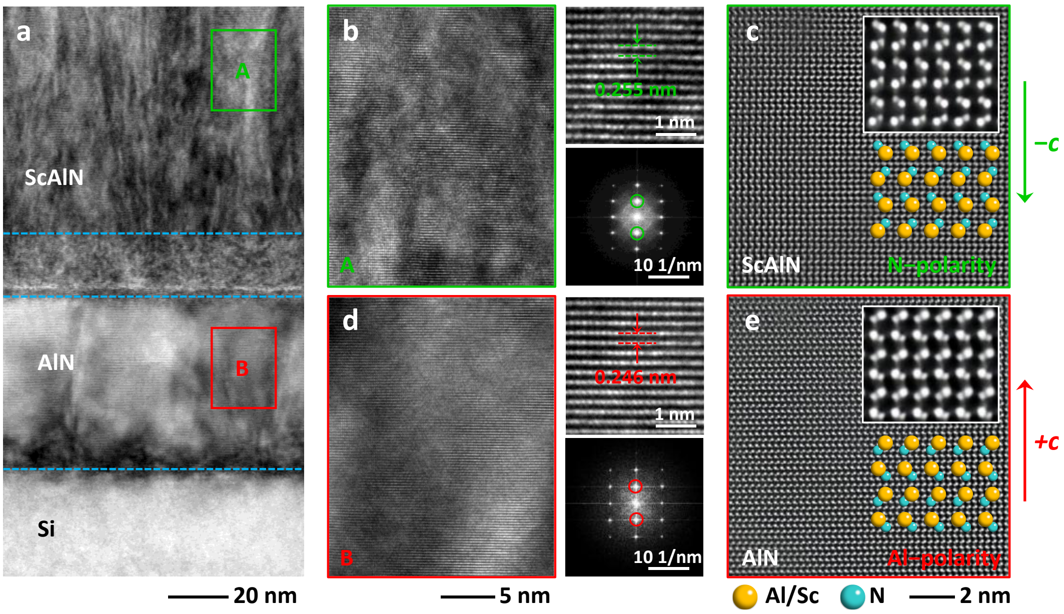

Fig. 3 Cross-sectional TEM characterization of the $Sc_{0.2}Al_{0.8}N$ and single-crystalline AlN seed layer interface. a Cross-sectional HRTEM image of the $Sc_{0.2}Al_{0.8}N$/AlN/Si heterostructure, showing a thin interfacial transition layer between AlN and ScAlN. **b** HRTEM images from region A (green) with corresponding lattice images and FFT patterns. **c** iDPC-STEM imaging of atomic structures in **b** and corresponding atomic models of ScAlN, viewed along the [11-20] zone axis (partially enlarged insets). **d** HRTEM images from region B (red) with corresponding lattice images and FFT patterns. **e** iDPC-STEM imaging of atomic structures in **d** and corresponding atomic models of AlN, viewed along the [11-20] zone axis (partially enlarged insets).

9) Optimization strategy: Removal of the AlN layer is used to optimize the device, however this step requires a layer transfer step, which is typically something to avoid. Why not target different optimization routes such as minimizing AlN seed layer thickness as much as possible and optimizing the AlN/ScAlN interface to avoid polarity inversion? What is the benefit of this approach for applications (since 5G and 6G are specifically mentioned as application scenarios)?

Response to Reviewer:

We agree that reducing the seed layer thickness or avoiding polarity inversion can to some extent mitigate the influence of the AlN seed layer on the overall piezoelectric performance of the AlN/ScAlN composite film. However, under high-frequency operating conditions relevant to 5G and 6G applications, the piezoelectric layer thickness has already been reduced to a few hundred nanometers to achieve GHz-scale resonance (in this work, AlN is 50 nm-thick and that of ScAlN is 280 nm-thick). A 50 nm AlN layer is already regarded as a relatively thin seed layer for epitaxial growth. Under such constraints, **further reduction in thickness would lead to a noticeable degradation in crystallinity and overall film quality.** Although such a thin AlN layer still exhibits better texture than PVD-deposited AlN, its quality is insufficient to fully transfer the advantages of the MOCVD-grown single-crystalline template during the subsequent ScAlN deposition.

On the other hand, polarity control of AlN and ScAlN films remains an important yet challenging topic[1-13]. Previous studies have shown that AlN films grown epitaxially on Si (111) substrates tend to exhibit Al-polar orientation[1,2]. This is primarily determined by interfacial bonding chemistry: the Si/AlN interface is typically composed of Si-N bonds, resulting in AlN nucleation from interfacial nitrogen atoms and subsequent growth along the [0001] direction, leading to an Al-polar configuration. **Although polarity inversion has been reported through methods such as inserting interlayers[4-6], tuning deposition parameters[8,9], or introducing oxygen or Mg dopants[10-12], these approaches generally degrade crystalline quality and piezoelectric performance (e.g., reductions in d_{33} and k_{eff}^2)[12,13].** Therefore, achieving effective polarity control remains a significant challenge.

In addition, as noted in Response to **Comment 2)**, ScAlN films directly deposited on Mo electrodes exhibit markedly poorer crystallinity compared to those grown on the AlN seed layer, indicating that high-quality epitaxial templates are indispensable for achieving superior film performance. Therefore, if further improvement in filter characteristics such as insertion loss and out-of-band suppression is desired, the layer transfer process becomes a necessary and effective route. This optimization is primarily related to structural quality rather than polarity itself.

Considering these factors, we adopted a direct removal of the AlN seed layer strategy, which preserves the excellent templating function of AlN while ultimately yielding a single-polar ScAlN film. **This approach is broadly applicable to different polarity configurations, whether the AlN and ScAlN layers are parallel or antiparallel in polarization, removing the AlN layer allows the ScAlN film to recover its intrinsic piezoelectric properties and polarization state.** Furthermore, the etching process for the AlN seed layer has been optimized in our experiments, achieving stable and reproducible termination control. This process is technically mature, exhibits low complexity, and does not impose additional challenges for overall process compatibility.

As the operating frequency in wireless communication systems continues to increase from approximately 2 GHz in early 5G bands to above 6 GHz in emerging 6G front-end modules, signal attenuation becomes more pronounced, and stricter requirements are imposed on filter insertion loss and out-of-band rejection. **These trends pose two major challenges for next-generation acoustic filters: (1) improving the crystalline quality of piezoelectric films to minimize intrinsic acoustic loss, and (2) optimizing device structures to sustain high performance at elevated frequencies.** This work specifically focuses on the former challenge by enhancing the film quality through the introduction of a MOCVD-grown single-crystalline AlN seed layer, which serves as an effective epitaxial template to reduce structural defects and thereby lower acoustic loss in the ScAlN film.

References

1. Radtke, G., Couillard, M., Botton, G. A., Zhu, D. & Humphreys, C. J. Scanning transmission electron microscopy investigation of the Si (111)/AlN interface grown by metalorganic vapor phase epitaxy. *Appl. Phys. Lett.* 97, 251901 (2010).
2. Radtke, G., Couillard, M., Botton, G. A., Zhu, D. & Humphreys, C. J. Structure and chemistry of the Si (111)/AlN interface. *Appl. Phys. Lett.* 100, 011910 (2012).
3. Liu, Z., Liu, B., Ren, F., Yin, Y. et al. Atomic-Scale Mechanism of Spontaneous Polarity Inversion in AlN on Nonpolar Sapphire Substrate Grown by MOCVD. *Small.* 18, 2200057 (2022).
4. Wu, Y., Hanlon, A., Kaeding, J. F., Sharma, R., Fini, P. T., Nakamura, S., Speck, J. S. Effect of nitridation on polarity, microstructure, and morphology of AlN films Available. *Appl. Phys. Lett.* 84, 912–914 (2004).
5. Park, J. S., Minegishi, T., Lee, S. H., Im, I. H., Park, S. H., Hanada, T., Goto, T., Cho, M. W., Yao, T., Hong, S. K., Chang, J. H. Effects of interfacial layer structures on crystal structural properties of ZnO films. *J. Vac. Sci. Technol. A*. 26, 90–96 (2008).
6. Hite, J. K., Twigg, M. E., Mastro, M. A., Eddy, C. R. Jr. & Kub, F. J. Initiating polarity inversion in GaN growth using an AlN interlayer. *Phys. Status. Solidi. A*. 208, 1504–1506 (2011).
7. Jasinski, J., Liliental-Weber, Z., Paduano, Q. S. & Weyburne, D. W. Inversion domains in AlN grown on (0001) sapphire. *Appl. Phys. Lett.* 83, 2811–2813 (2003).
8. Niu, Y., Deng, T., Zhang, X. et al. Lattice Polarity Manipulation of AlN Films on SiC Substrates for N-Polar GaN HEMTs. *Cryst. Growth Des.* 24, 7477–7485 (2024).
9. Milyutin, E., Harada, S., Martin, D., Carlin, J. F., Grandjean, N., Savu, V., Vaszquez-Mena, O., Brugger, J. & Muralt, P. Sputtering of (001) AlN thin films: Control of polarity by a seed layer. *J. Vac. Sci. Technol. B.* 28, L61–L63 (2010).

10. Romano, L. T., Northrup, J. E., Ptak, A. J. & Myers, T. H. Faceted inversion domain boundary in GaN films doped with Mg. *Appl. Phys. Lett.* 77, 2479–2481 (2000).
11. Jiang, K., Ben, J., Sun, X., et al. The AlN lattice-polarity inversion in a high-temperature-annealed c-oriented AlN/sapphire originated from the diffusion of Al and O atoms from sapphire. *Nanoscale Adv.* 6, 418–427 (2024).
12. Anggraini, S. A., Uehara, M., Hirata, K., Yamada, H. & Akiyama, M. Polarity inversion of aluminum nitride thin films by using Si and MgSi dopants. *Sci. Rep.* 10, 4369 (2020).
13. Mizuno, T., Umeda, K., Aida, Y., Honda, A., Akiyama, M., Nagase, T. & Kobayashi, M. Germanium aluminum nitride thin films for piezo-MEMS devices. Proc. 19th Int. Conf. Solid-State Sensors, Actuators and Microsystems (TRANSDUCERS 2017), 1891–1894 (IEEE, 2017).

10) FBAR 1-3: FBAR-1 is MOCVD AlN + ScAlN, FBAR-2 is ScAlN with the PVD AlN seed removed and FBAR-3 is ScAlN with the MOCVD AlN seed removed. A sample with PVD AlN seed + ScAlN is missing, especially if the impact of poly vs. single crystalline seeds is to be studied.

Response to Reviewer:

At the early stage of this study, we indeed fabricated FBARs with ScAlN deposited on PVD AlN seed layers and on MOCVD AlN seed layers (the latter corresponding to FBAR-1 in the main text) to compare the effect of seed crystallinity, as shown in **Fig. R6.** As expected, FBARs fabricated from ScAlN films grown on MOCVD AlN seed layers of superior crystallographic quality exhibited much higher Q factors (Q_{max}=970) than those based on PVD AlN seeds (Q_{max}=189), highlighting the role of a well-oriented AlN template in enhancing film quality and device performance. However, both devices showed a relatively low effective electromechanical coupling coefficient (k_{eff}^2) of around 6%, far below the theoretical value (around 13%). This finding suggested that, in addition to seed crystallinity, the presence of an AlN seed interlayer itself could suppress.

Motivated by this observation, FBARs were subsequently re-fabricated on PVD AlN seed layers with a removal step (FBAR-2 in the main text). The PVD configuration was selected as a cost- and time-efficient platform to probe the role of seed removal on k_{eff}^2. The experimental results confirmed that after removing the PVD seed layer, the k_{eff}^2 of the device was significantly improved, verifying the previous theoretical prediction.

After confirming this mechanism, we applied the same strategy to devices based on MOCVD-grown AlN seed layers, re-fabricating them with the seed layer removed

(FBAR-3 in the main text). Subsequent optimization of the electrode thickness enabled operation at even higher frequencies. Benefiting from the high-quality MOCVD AlN template, these devices achieved the balance of high Q and improved k_{eff}^2. **Table S6** (in the revised **Supplementary Information**) summarizes the stack thickness parameters of the four groups of FBARs.

The devices investigated in this study form a factorial matrix of four possible configurations, as shown in **Fig. S12** (in the revised **Supplementary Information**). Three representative FBARs (FBAR 1-3) are presented in the main text as the key comparison groups. The comparison between FBAR-1 and FBAR-3 isolates the effect of retaining versus removing the AlN seed layer on k_{eff}^2, whereas the comparison between FBAR-2 and FBAR-3 examines how the crystalline quality of the ScAlN film, determined by the underlying seed, governs the device Q factor. The remaining configuration, in which the PVD AlN seed layer was retained beneath the ScAlN film, exhibited markedly inferior performance. Consequently, no further filter-level design or characterization was pursued for this case. Our systematic filter demonstrations therefore focused on FBAR 1-3. In accordance with the reviewer's suggestion, the FBAR for the configuration in which the PVD AlN seed layer was retained beneath the ScAlN film have been added to the **Supplementary Information**, while the main text highlights the three representative FBARs.

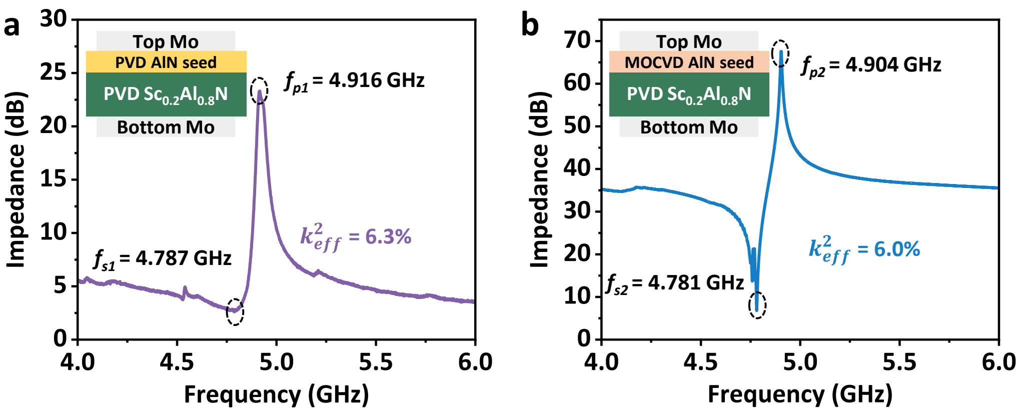

Fig. R6 Impedance spectra of FBARs with different AlN seed layers retained in the device stack. a FBAR based on a PVD AlN seed layer, exhibiting k_{eff}^2=6.3% and a maximum quality factor Q_{max}=189. **b** FBAR based on a PVD AlN seed layer, exhibiting k_{eff}^2=6.0% and a maximum quality factor Q_{max}=970.

Revised Supplementary Information:

Line 383:

Table S6 summarizes the layer-stack thicknesses and processing conditions for the four FBAR devices, all of which maintain identical AlN seed and ScAlN film thicknesses as well as top and bottom Mo electrodes, except for FBAR-3 where the electrodes were strategically thinned to achieve a higher resonance frequency as part of the design-process optimization.

Table S6 Thickness parameters of the FBAR layer stack.

Device	Top Mo	ScAlN	Bottom Mo	AlN seed	Seed processing
FBAR-0	80 nm	280 nm	80 nm	50 nm	PVD AlN (Retained)
FBAR-1	80 nm	280 nm	80 nm	50 nm	MOCVD AlN (Retained)
FBAR-2	80 nm	280 nm	80 nm	50 nm	PVD AlN (Removed)
FBAR-3	65 nm	280 nm	65 nm	50 nm	MOCVD AlN (Removed)

FBAR-0, an early-stage test structure fabricated with a retained PVD AlN seed layer, exhibits a low effective electromechanical coupling coefficient of 6.3% and a limited quality factor (Q_{max} =189) in its impedance response (**Fig. S12a**), confirming that the poor crystallinity of the PVD-deposited seed significantly degrades performance. The overall trends in **Fig. S12c** and **S12d** show that devices with MOCVD AlN seeds achieve higher Q than those with PVD seeds, while removing the seed layer further enhances the effective electromechanical coupling coefficient. Statistical comparison in **Fig. S12d**, based on over 100 samples per group, reveals that FBAR-1 operates at a higher resonance frequency than FBAR-0, and FBAR-3 at a higher frequency than FBAR-2, highlighting the substantial improvement in resonance quality attained with single-crystalline seed layers.

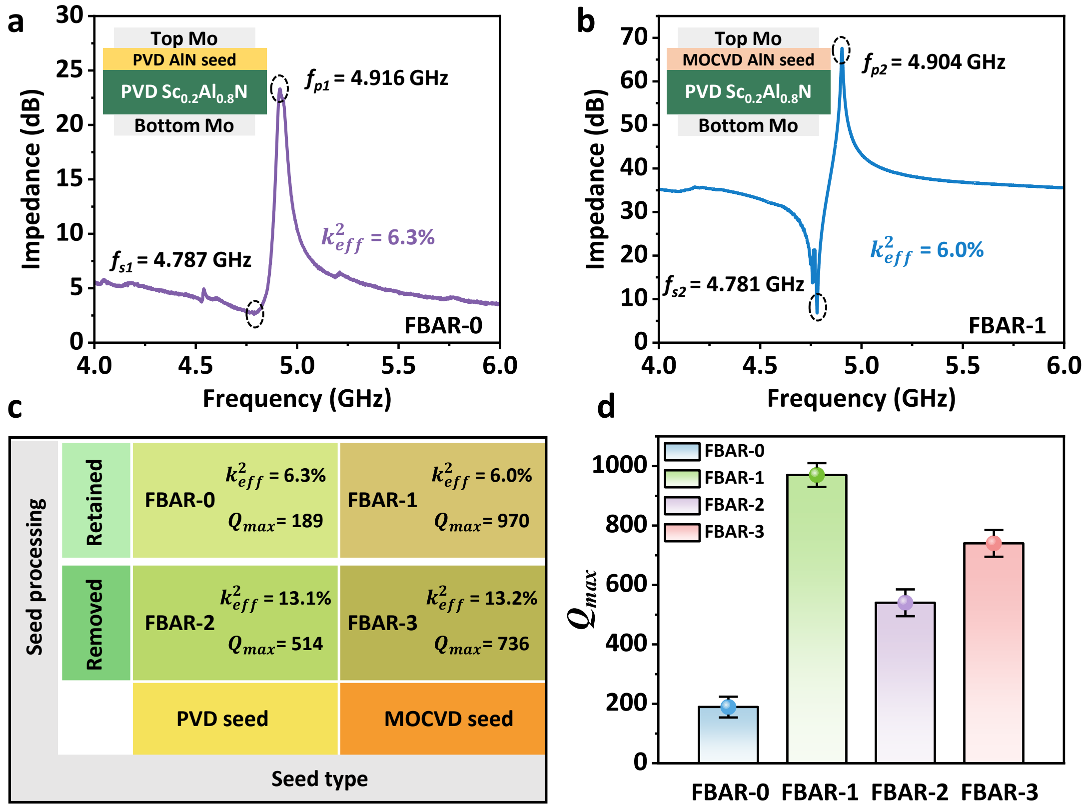

Fig. S12 Electrical characterization of FBARs with different AlN seed conditions. **a** Impedance curve of the FBAR with a retained PVD AlN seed layer, exhibiting k_{eff}^2 =6.3% and a Q_{max}=189. **b** Impedance curve of the FBAR with a retained MOCVD AlN seed layer, exhibiting k_{eff}^2 =6.0% and a maximum quality factor Q_{max}=970. **c** Summary of k_{eff}^2 and Q_{max} in FBARs fabricated with different AlN seed types (PVD or MOCVD) and processing conditions (retained or removed). Devices using MOCVD AlN seeds exhibit consistently higher Q_{max} values than those based on PVD seeds, while removing the AlN seed layer significantly enhances k_{eff}^2 in both cases. **d** Statistical analysis of Q factors for the four FBAR groups.

11) Poly vs. single crystalline: This is claimed, but not supported by the data. Why is the MOCVD AlN layer single crystalline, a FWHM of 0.94° does not imply this without other supporting data.

Response to Reviewer:

In many epitaxial growth studies, the term "single-crystalline thin film" is commonly used to describe epitaxial layers that possess a single crystallographic orientation and maintain lattice registry with the underlying substrate, in contrast to textured polycrystalline films typically obtained by sputtering[1-5]. Our use of "single-crystalline AlN" follows this well-established convention in the epitaxy literature.

We would also like to clarify that the FWHM value of 0.94° mentioned in the manuscript corresponds to the 280 nm-thick $Sc_{0.2}Al_{0.8}N$ layer grown on the MOCVD AlN seed, whereas the MOCVD AlN seed layer itself exhibits a narrower FWHM of 0.63°. To address this point, we have included additional HRTEM and FFT analyses in the revised Supplementary Information.

As shown in **Fig. R7a** the PVD AlN film exhibits discontinuous lattice fringes and locally misaligned domains, yet the lattice planes remain predominantly oriented along the c-axis. The corresponding FFT pattern shows slightly diffuse (002) diffraction spots, indicating a polycrystalline structure with limited crystallinity. In contrast, the MOCVD AlN layer displays uniform and coherently aligned lattice fringes throughout the entire film thickness, as shown in **Fig. R7b**, and its FFT pattern presents a single set of sharp (002) diffraction spots without polycrystalline rings, confirming a well-defined epitaxial single orientation.

In summary, we consider the AlN film grown by MOCVD to be a single-crystalline epitaxial film, in accordance with the conventional definition widely adopted in the epitaxy community, whereas the AlN film deposited by PVD is characterized as a textured polycrystalline film. The corresponding data have been supplemented in the revised version (newly revised **Fig. 2** and **Fig. S4**, as detailed in **Comment 5 and Comment 6**).

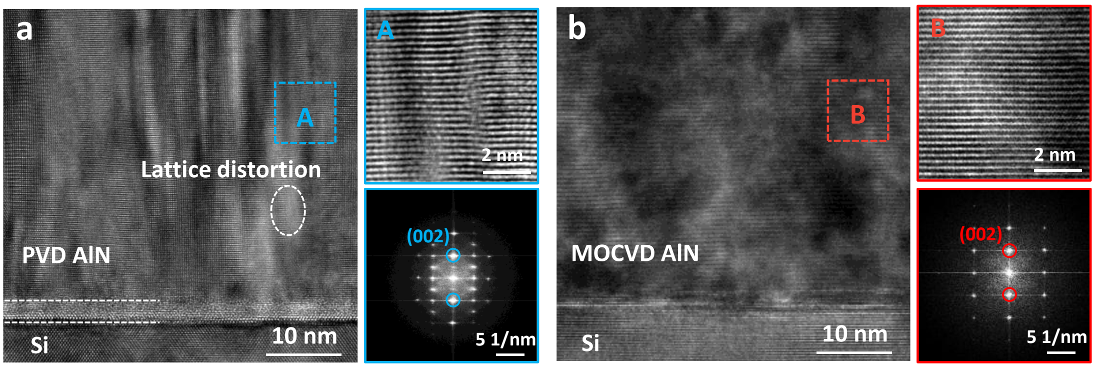

Fig. R7 Cross-sectional HRTEM comparison of PVD deposited and MOCVD grown AlN seed layers. a Cross-sectional HRTEM image of the PVD AlN, together with a magnified region A and corresponding FFT pattern. The lattice fringes are mainly oriented along the c-axis but show local bending and contrast variations, and the FFT pattern exhibits slightly diffuse diffraction spots, indicating a polycrystalline structure. **b** Cross-sectional HRTEM image of the MOCVD AlN, together with a magnified region B and corresponding FFT pattern. The lattice fringes are highly ordered and continuous along the c-axis, and the FFT pattern displays a single set of sharp (002) diffraction spots without polycrystalline rings, indicating a single-crystalline structure.

References

1. Ouyang, P., Yi, X. & Li, G. Single-Crystalline Bulk Acoustic Wave Resonators Fabricated With AlN Film Grown by a Combination of PLD and MOCVD Methods. *IEEE Electron Device Lett.* 45, 538–541 (2024).
2. Yi, X., Zhao, L., Ouyang, P. et al. High-Quality Film Bulk Acoustic Resonators Fabricated on AlN Films Grown by a New Two-Step Method. *IEEE Electron Device Lett.* 43, 942–945 (2022).
3. Matloubian, M. & Gershenzon, M. MOCVD epitaxial growth of single crystal GaN, AlN and $Al_xGa_{1-x}N$. J. Electron. Mater. 14, 633–644 (1985).
4. Yang, H., Wang, W., Liu, Z. & Li, G. Epitaxial growth of 2 inch diameter homogeneous AlN single-crystalline films by pulsed laser deposition. *J. Phys. D: Appl. Phys.* 46, 105101 (2013).
5. Yang, H., Wang, W., Liu, Z. & Li, G. Homogeneous epitaxial growth of AlN single-crystalline films on 2 inch-diameter Si (111) substrates by pulsed laser deposition. *CrystEngComm*. 15, 7171 (2013).

12) Lines 335-337: Acoustic confinement by the AlN layer: Please elaborate, as the acoustic impedance mismatch between AlN and ScAlN is not large. Why would there be any relevant acoustic confinement. In fact, would this not be bad, as it might deteriorate the frequency response?

Response to Reviewer:

We acknowledge that the original description of "acoustic confinement" was imprecise and have rectified this throughout the manuscript. Operating frequency, thin-film quality, and device architecture represent fundamental determinants of resonator Q factor, with the present work concentrating on Q enhancement via superior film crystallinity. The MOCVD-grown single-crystalline AlN serves as an epitaxial template that minimizes lattice defects and grain boundary dissipation in the ScAlN overlayer, thereby enhancing resonator Q through crystalline coherence rather than wave confinement. However, we fully concur that retaining AlN introduces detrimental effects: 1) its lower electromechanical coupling coefficient K_t^2 (~6.5%) versus ScAlN reduces overall transduction efficiency, and 2) polarity inversion at the AlN/ScAlN interface further degrades effective K_t^2. This fundamental trade-off motivated our dual strategy: leveraging MOCVD AlN for initial heteroepitaxial growth quality while strategically removing it post-deposition to maximize piezoelectric response. The empirical superiority of this approach is demonstrated in FBAR performance metrics (**Fig. 4** in the revised manuscript), where seed layer removal yielded 740 MHz bandwidth while maintaining a Q_{max} of 736 at over 6GHz through defect-minimized ScAlN.

Revised Main Text:

Line 336:

…FBAR-1 achieves the highest Q_{max} of 970, attributed to the high crystalline quality and reduced defect density of the $Sc_{0.2}Al_{0.8}N$ film grown on single-crystalline AlN. Comparatively, FBAR-2 exhibits a significantly lower Q_{max} of 514 due to poor crystallinity in $Sc_{0.2}Al_{0.8}N$ deposited on polycrystalline AlN, where random grain orientations disrupt *c*-axis alignment, causing stress inhomogeneity and anisotropic deformation. These microstructural irregularities act as scattering centers, increasing propagation losses[17,19,44]. FBAR-3 employs the same single-crystalline AlN seed as FBAR-1 but undergoes post-deposition AlN removal, yielding a Q_{max} of 736. **Consequently, the Q_{max} of FBAR-3 is slightly lower than that of FBAR-1, primarily attributed to the >6 GHz operating frequency that induces severe acoustic energy dissipation[45,46].** Nevertheless, FBAR-3 achieves about 43% higher Q_{max} than FBAR-2 and delivers the highest FOM of 97, demonstrating superior overall performance.

13) Fig 5: Why are there 2 S ports? The device schematic shows a single input port. Are both S ports connected?

Response to Reviewer:

We thank the reviewer for raising this point and for the opportunity to clarify the signal pad configuration in **Fig. 5**. In high-frequency RF probing, the two standard coplanar pad layouts are Ground-Signal-Ground (GSG) and Ground-Signal-Signal-Ground (GSSG). The GSG layout constitutes a single-ended port where the signal pad is flanked by two ground pads, providing strong field confinement for single-ended excitation, as illustrated in **Fig. R8a**. Conversely, the GSSG configuration represents a differential port featuring two signal pads positioned between outer ground pads, shown in **Fig. R8b**. This arrangement enables direct differential-mode excitation, preserves signal symmetry, suppresses common-mode interference, and maintains precise control of the 100 Ω differential impedance (50 Ω per line) required for high-frequency measurements.

In **Fig. 4** of the manuscript, the individual **FBAR** were designed as **single-port** devices and implemented with a GSG pad layout, which is the standard configuration for single-ended excitation and measurement. By contrast, the filter shown in **Fig. 5** is a two-port differential device. Each port therefore adopts an identical GSSG pad layout, allowing direct connection to calibrated GSSG probes. Regarding the role of the "S" pads, the left-hand pair (S^+/S^-) corresponds to the input differential port (Port 1), while the right-hand pair forms the output differential port (Port 2). These two sets of signal pads belong to different ports and are not connected internally. The outer ground pads on each side are tied together locally, ensuring proper impedance matching to the probe grounds and providing electromagnetic shielding to suppress common-mode noise.

During measurement, the vector network analyzer excites the input pair (S^+/S^- at Port 1) in differential mode through the GSSG probe, and the output is collected from the corresponding pair at Port 2. The measured S_{21} therefore represents the differential transmission coefficient from the input differential port to the output differential port, consistent with the two-port differential S-parameter definition.

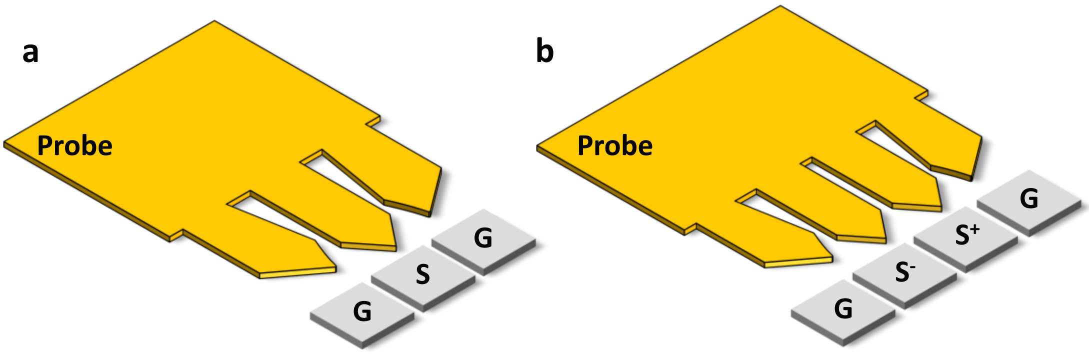

Fig. R8 GSG and GSSG probe configurations. a GSG probe contacting a three-pad structure (G-S-G) for single-ended excitation. **b** GSSG probe contacting a four-pad structure (G-S^--S^+-G) for differential excitation.

14) Line 520: How is selectivity achieved for etching AlN on top of ScAlN? Is an etch monitoring method used to stop the process as soon as the ScAlN layer is reached?

Response to Reviewer:

As correctly pointed out, in our work the removal of the AlN seed layer was monitored in real time by optical emission spectroscopy (OES). And the process is implemented using inductively coupled plasma (ICP) dry etching, where distinct etching recipes were optimized for AlN and ScAlN to achieve high selectivity (**Table S5** in the newly revised **Supplementary Information**). The AlN seed layer was etched with a Cl_2-based chemistry, while the ScAlN layer employed a BCl_3-based process. To ensure precise termination, in situ OES was introduced for endpoint detection **(Fig. S10a** in the newly revised **Supplementary Information**). OES monitors the characteristic light emitted by excited plasma species and volatile reaction by-products during etching, allowing real-time tracking of process evolution. When the AlN layer is completely removed and the underlying ScAlN is exposed, the reaction chemistry changes abruptly, producing a sharp drop in emission intensity that marks the etch endpoint (**Fig. S10a**). This approach ensures complete AlN removal while preserving the structural and functional integrity of the ScAlN film. The corresponding description and data have been supplemented in the revised manuscript.

Revised Supplementary Information:

Line 335:

AlN seed layer etching

After Au-Au bonding and Si substrate removal, the AlN seed layer in the second and third FBAR sets is selectively removed via ICP dry etching to assess its impact on device performance. Given the near-identical chemical reactivity of AlN and ScAlN, uncontrolled etching risks over-etching and damaging the ScAlN layer. Distinct etching recipes are optimized for each material to enhance selectivity, as detailed in **Table S4**. The AlN seed layer is etched using a Cl_2-based chemistry, while the ScAlN layer employs a BCl_3-based process. In Cl_2 plasma, AlN exhibits a significantly higher etch rate than ScAlN due to the greater reactivity of the Al–N bond with Cl radicals and the higher volatility of $AlCl_3$ compared to $ScCl_3$. This inherent etch rate difference ensures natural selectivity, protecting the underlying ScAlN when the endpoint is reached.

Table S5 ICP etching parameters for AlN and ScAlN films.

Target layer	Etching gas	Gas flow rate	Chamber pressure	RF power
AlN	Cl_2	50 sccm	8 mTorr	500 W
ScAlN	BCl_3	100 sccm	5 mTorr	500 W

The etching process is monitored in situ by optical emission spectroscopy (OES) (**Fig.**

S10a), where the emission signal associated with AlN reaction products remains stable during etching. Upon complete removal of the AlN seed layer and exposure of the underlying ScAlN, a sudden change in reaction chemistry causes a pronounced intensity drop, identified as the etch endpoint. This non-invasive, real-time detection enables precise termination, preventing over-etching and preserving device performance. Validation using an AlN/ScAlN test sample confirms endpoint accuracy, optical microscopy images before etching (**Fig. S10b**) show uniform contrast with clear pattern boundaries, while post-etching (**Fig. S10c**) reveals a distinct color shift due to ScAlN exposure, confirming complete AlN removal and a smooth, damage-free surface morphology.

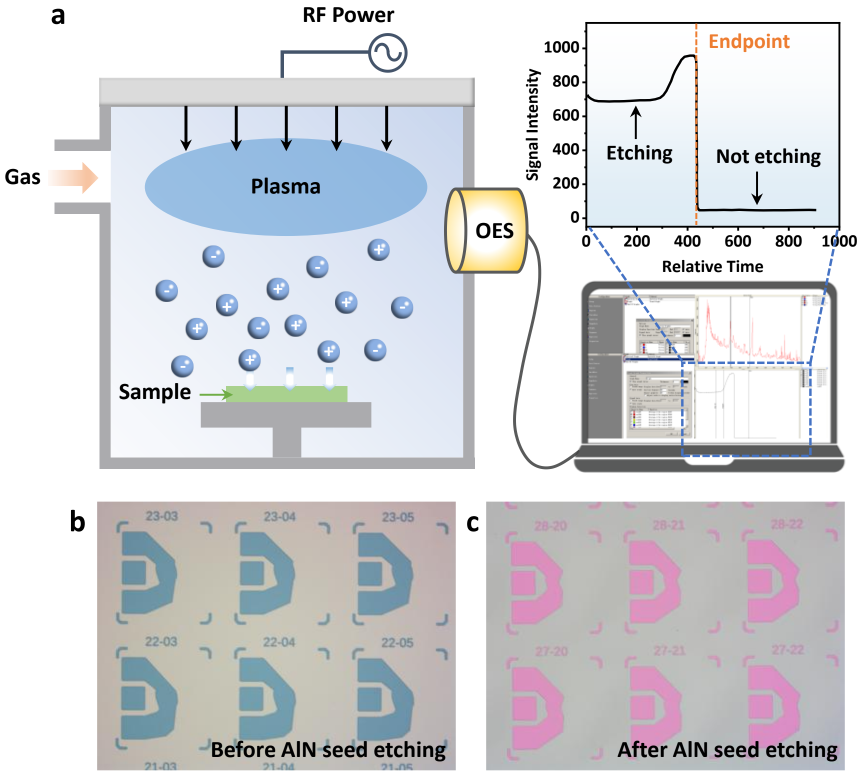

Fig. S10 The optical emission spectroscopy (OES)-based endpoint detection for AlN etching. a Schematic illustration of OES monitoring system used during the plasma etching of AlN. The RF-powered plasma generates reactive ions that bombard the sample surface, while the OES module detects the optical emission intensity of reaction products in real time. The inset shows a typical OES signal curve, where the sharp intensity drop indicates the endpoint corresponding to complete removal of the AlN seed layer. **b, c** Optical microscopy images of the MOCVD AlN seed layer before and after etching, respectively, confirming accurate endpoint control and a clean surface morphology.

15) Fig. S2: The rocking curve of AlN barely shows any signal, are you sure, the layer is crystalline at all? Show the Bragg Brentano spectrum.

Response to Reviewer:

We thank the reviewer for this comment and fully understand the concern regarding **Fig. S2** (the newly **Fig. S4** in revised Supplementary Information). Because the PVD AlN seed layer is only 50 nm-thick, X-ray rocking curve exhibits weak intensity and a broad FWHM, which can give the impression of an amorphous layer. However, this is dued to incomplete lateral coalescence and limited orientation coherence at such ultrathin thicknesses, rather than the absence of crystallinity.

We have added the X-ray diffraction (XRD) scans of both the PVD AlN and the MOCVD AlN seed layers in **Fig. 2** (in the revised manuscript). The PVD AlN shows a clear AlN (002) diffraction peak at 35.9°, confirming that the layer is crystalline. It should be noted that due to the large difference in peak intensities, as shown in **Fig. 2g,** the 50 nm-thick MOCVD-grown AlN seed layer exhibits a sharp, intense (002) diffraction peak, whereas the PVD-deposited AlN shows a broader, weaker (002) feature, indicating inferior c-axis orientation. Further verified by XRD rocking curves and HRTEM (Fig. S4), the PVD AlN seed layer displays a broad peak with a full width at half maximum (FWHM) of 4.50°, characteristic of poor c-axis alignment and polycrystalline nature, while the MOCVD AlN seed layer presents a sharp, narrow peak with a FWHM of 0.63°, demonstrating excellent c-axis orientation and single-crystalline quality. **Fig. R9a** and **Fig. R9b** are plotted with different vertical scales, the MOCVD AlN exhibits an (002) peak intensity more than one order of magnitude higher than that of the PVD AlN, highlighting their significant difference in crystalline quality. These results demonstrate that while the PVD AlN can provide a certain degree of orientation guidance, its improvement effect is limited. This is precisely why we subsequently employed high-quality MOCVD AlN as the seed layer to achieve superior crystalline quality and device performance.

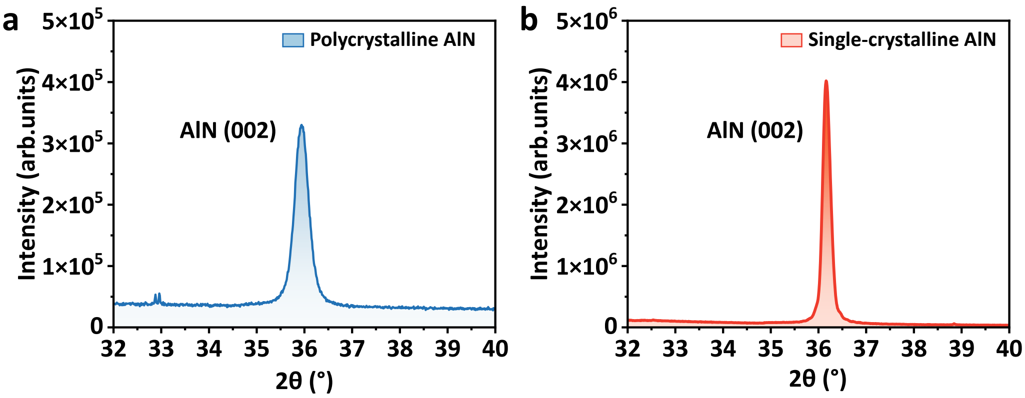

Fig. R9 XRD scans of AlN seed layers from 30° to 60°. a 50 nm-thick PVD AlN seed layer showing the AlN (002) diffraction peak at 35.9° and an additional weak peak at 44.4°, corresponding to fcc Al (200). **b** 50 nm-thick MOCVD AlN seed layer exhibiting a sharp and intense (002) reflection, more than one order of magnitude stronger than the PVD AlN.

Revised Main Text:

Line 188:

X-ray diffraction (XRD) measurements are conducted to evaluate the crystalline quality of both the AlN seed layers and the deposited $Sc_{0.2}Al_{0.8}N$ films. As shown in **Fig. 2d**, the 50 nm-thick MOCVD AlN seed layer exhibits a sharp, intense (002) diffraction peak, whereas the PVD AlN shows a broader, weaker (002) feature, indicating inferior *c*-axis orientation. Further verified by XRD rocking curves (**Figs. S4a and S4d**), the PVD AlN seed layer displays a broad peak with a full width at half maximum (FWHM) of 4.50°, characteristic of poor *c*-axis alignment and polycrystalline nature, while the MOCVD AlN seed layer presents a sharp, narrow peak with a FWHM of 0.63°, demonstrating excellent *c*-axis orientation and single-crystalline quality. High-resolution transmission electron microscopy (HRTEM) images of the AlN seed layers reveal that PVD AlN contains obvious defect-rich and partially amorphous regions, whereas MOCVD AlN maintains a highly ordered lattice (**Figs. S4b and S4e**). For the 280 nm-thick $Sc_{0.2}Al_{0.8}N$ films deposited on these templates, the XRD peak of the film on MOCVD AlN remains narrower and higher in intensity compared to those on PVD AlN or Si substrates. The *c*-axis orientation of the $Sc_{0.2}Al_{0.8}N$ films is further assessed via XRD rocking curves (**Fig. 2e**), the film on the MOCVD single-crystalline AlN seed layer exhibits the smallest FWHM of 0.94° with a sharper peak and higher intensity, while those on PVD polycrystalline AlN and bare Si substrates show larger FWHM of 2.12° and 3.31°, respectively, reflecting the superior crystal quality and improved *c*-

axis orientation of the $Sc_{0.2}Al_{0.8}N$ film deposited on the MOCVD AlN seed layer.

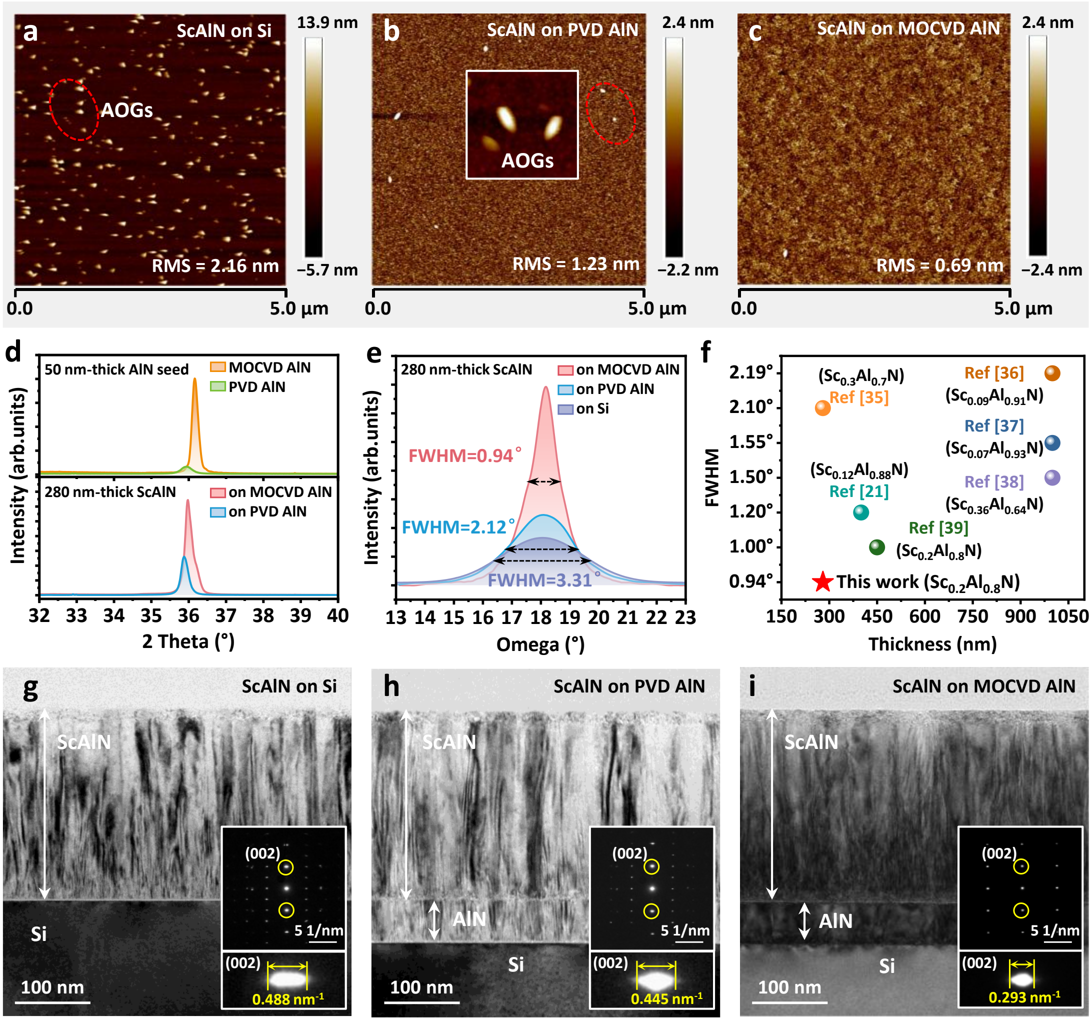

Fig. 2 Characterization of $Sc_{0.2}Al_{0.8}N$ film deposited on different substrates: Si, PVD and MOCVD AlN seed layer. a-c AFM images of different films. **d** XRD scans of AlN seed layers and $Sc_{0.2}Al_{0.8}N$ films deposited on different templates. The upper curve shows the (002) diffraction peaks of 50 nm-thick AlN seed layers prepared by MOCVD and PVD. The lower panel presents the (002) peaks of 280 nm-thick $Sc_{0.2}Al_{0.8}N$ films deposited on the corresponding AlN templates. **e** Rocking curve of the 280 nm-thick $Sc_{0.2}Al_{0.8}N$ film. **f** Comparison of rocking curve FWHM of $Sc_xAl_{1-x}N$ films with varying thicknesses between this study and previous works. **g-i** Cross-sectional TEM and corresponding SAED patterns.

Reviewer #2 (Remarks to the Author):

Expertise: acoustic resonators

The manuscript entitled "Enhancing ScAlN-Based FBAR Performance via MOCVD-AlN Seed Layer Crystallinity Optimization and Polarity Inversion Elimination for Sub-7GHz Applications" introduced a dual-optimization strategy aimed at improving the performance of ScAlN-based Film Bulk Acoustic Resonators (FBARs) by addressing both crystal quality and polarity alignment. First, the single? crystalline AlN seed layer was introduced MOCVD to significantly improve the microstructure of $Sc_{0.2}Al_{0.8}N$ film and the AlN seed layer was removed subsequently in post-processing to eliminate the polarity inversion at the AlN/ScAlN interface. While the core concept of eliminating polarization reversal through the removal of the AlN seed layer is innovative, several critical issues within the manuscript necessitate thorough revision prior to consideration for publication. The current submission suffers from a lack of methodological clarity, insufficient experimental validation for pivotal claims, and a need for more comprehensive data presentation.

Response to Reviewer:

We sincerely appreciate the reviewer's insightful critique regarding methodological clarity, experimental validation, and data comprehensiveness. To address these concerns: 1) We have enhanced our theoretical framework with Mori-Tanaka modeling, quantitatively predicting performance degradation due to polarity mismatch, as presented in the original manuscript (**Fig. 1e**). 2) Existing cross-sectional TEM evidence (**Fig. 3**) directly visualizes the polarity inversion at the AlN/ScAlN bilayer structure, confirming the theoretical predictions. 3) Our methodology establishes a rigorous multiscale validation framework, encompassing theoretical modeling predicting polarization-induced degradation, atomic-resolution structural characterization via cross-sectional STEM confirming the Al-polar AlN to N-polar ScAlN interface reversal, and culminating in device-level experimental validation where FBAR-3 achieves a k_{eff}^2 of 13.2% and an FOM of 97. This end-to-end integration bridges fundamental materials design with device optimization.

We emphasize that our dual-optimization strategy effectively resolves the fundamental conflict between crystallinity enhancement and polarity mismatch in piezoelectric heterostructures, combining novel theoretical insights, atomic-scale structural validation, and device-level demonstrations. We hope this revised response meets the high standards of the reviewers and the journal.

Specific Points Requiring Major Revision:

1. Removal of AlN Seed Layer: The central claim of the manuscript revolves around removing the single-crystal AlN seed layer to enhance the piezoelectric properties of the ScAlN layer due to the cancellation of piezoelectricity when both layers with opposite polarization are present. However, the manuscript fails to describe the methodology or process used for the removal of this single crystal AlN seed layer. This is a critical omission that undermines the reproducibility and understanding of the presented work. This process also appears to be missing from the fabrication process flow in Figure S5 and the corresponding optical microscopy images in Figure S6.

Response to Reviewer:

As correctly noted, the removal of the AlN seed layer is a critical step for ensuring device performance. This process is implemented using inductively coupled plasma (ICP) dry etching, where distinct etching recipes were optimized for AlN and ScAlN to achieve high selectivity (**Table S5** in the newly revised **Supplementary Information**). The AlN seed layer was etched with a Cl_2-based chemistry, while the ScAlN layer employed a BCl_3-based process. To ensure precise termination, in situ optical emission spectroscopy (OES) was introduced for endpoint detection **(Fig. S10a** in the newly revised **Supplementary Information**). OES monitors the characteristic light emitted by excited plasma species and volatile reaction by-products during etching, allowing real-time tracking of process evolution. When the AlN layer is completely removed and the underlying ScAlN is exposed, the reaction chemistry changes abruptly, producing a sharp drop in emission intensity that marks the etch endpoint (**Fig. S10a**). This approach ensures complete AlN removal while preserving the structural and functional integrity of the ScAlN film. The corresponding description and data have been supplemented in the revised manuscript.

Revised Supplementary Information:

Line 335:

AlN seed layer etching

After Au-Au bonding and Si substrate removal, the AlN seed layer in the second and third FBAR sets is selectively removed via ICP dry etching to assess its impact on device performance. Given the near-identical chemical reactivity of AlN and ScAlN, uncontrolled etching risks over-etching and damaging the ScAlN layer. Distinct etching recipes are optimized for each material to enhance selectivity, as detailed in **Table S4**. The AlN seed layer is etched using a Cl_2-based chemistry, while the ScAlN layer employs a BCl_3-based process. In Cl_2 plasma, AlN exhibits a significantly higher etch rate than ScAlN due to the greater reactivity of the Al–N bond with Cl radicals and the higher volatility of $AlCl_3$ compared to $ScCl_3$. This inherent etch rate difference ensures natural selectivity, protecting the underlying ScAlN when the endpoint is reached.

Table S5 ICP etching parameters for AlN and ScAlN films.

Target layer	Etching gas	Gas flow rate	Chamber pressure	RF power
AlN	Cl_2	50 sccm	8 mTorr	500 W
ScAlN	BCl_3	100 sccm	5 mTorr	500 W

The etching process is monitored in situ by optical emission spectroscopy (OES) (**Fig. S10a**), where the emission signal associated with AlN reaction products remains stable during etching. Upon complete removal of the AlN seed layer and exposure of the underlying ScAlN, a sudden change in reaction chemistry causes a pronounced intensity drop, identified as the etch endpoint. This non-invasive, real-time detection enables precise termination, preventing over-etching and preserving device performance. Validation using an AlN/ScAlN test sample confirms endpoint accuracy, optical microscopy images before etching (**Fig. S10b**) show uniform contrast with clear pattern boundaries, while post-etching (**Fig. S10c**) reveals a distinct color shift due to ScAlN exposure, confirming complete AlN removal and a smooth, damage-free surface morphology.

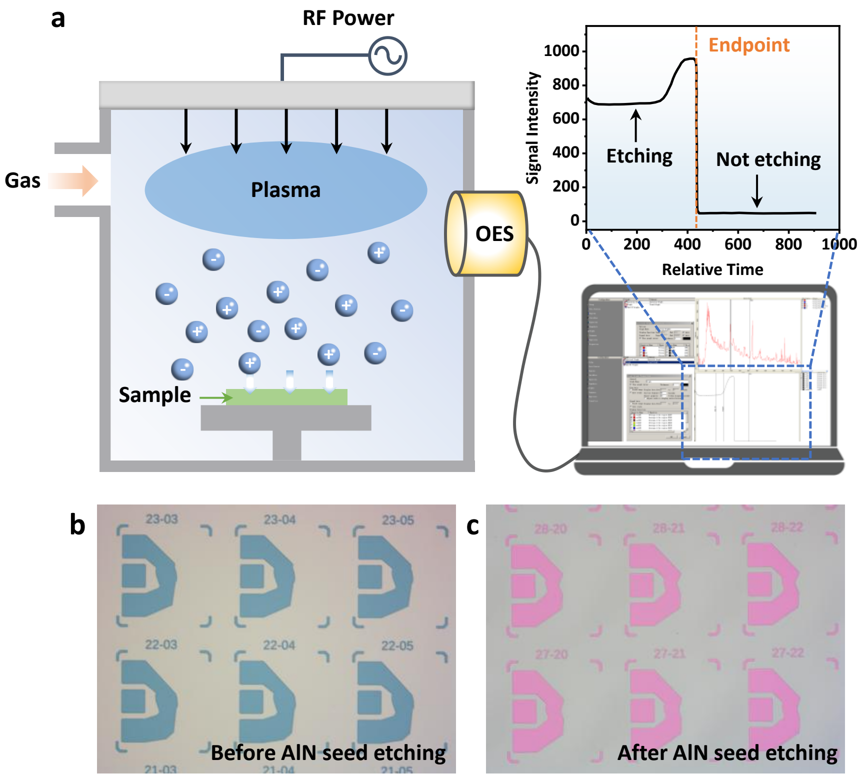

Fig. S10 The optical emission spectroscopy (OES)-based endpoint detection for AlN etching. a Schematic illustration of OES monitoring system used during the plasma etching of AlN. The RF-powered plasma generates reactive ions that bombard the sample surface, while the OES module detects the optical emission intensity of reaction products in real time. The inset shows a typical OES signal curve, where the sharp intensity drop indicates the endpoint corresponding to complete removal of the AlN seed layer. **b, c** Optical microscopy images of the MOCVD AlN seed layer before and after etching, respectively, confirming accurate endpoint control and a clean surface morphology.

2. Experimental Validation of Piezoelectric Properties Model: The manuscript presents a simplified model calculating the piezoelectric characteristics as a function of layer thickness for the AlN/ScAlN bilayer structure. However, there is a significant lack of experimental data to support and validate this model. The manuscript claims that integrating ScAlN on an AlN seed layer with opposite polarity causes a pronounced degradation in d_{33}, K_t^2 ,and k_{eff}^2 and that even with aligned polarization, performance declines with an increasing AlN fraction. This core assertion requires robust experimental validation, not just calculation results.

Response to Reviewer:

The AlN/ScAlN bilayer piezoelectric model established in this work predicts composite film parameter variations and elucidates how polarity alignment and thickness ratios affect device piezoelectric performance, thereby providing theoretical design guidance. While fully acknowledging reviewers' suggestions for systematic thickness-ratio validation, implementing such experiments would necessitate multiple independent epitaxial growths and full wafer processes, each requiring dedicated deposition, lithography, and etching steps spanning months per batch, making comprehensive sweeps prohibitively time-consuming and costly. Therefore, targeted experimental validation was conducted by fabricating FBARs with ScAlN deposited on PVD and MOCVD AlN seed layers (the latter corresponding to FBAR-1 in the manuscript) to evaluate the influence of seed crystallinity and verify the model's predictive accuracy for electromechanical coefficients (**Fig. S12** in the newly revised **Supplementary Information**). Experimental results align with theoretical predictions (**Fig. 1**), though certain measured k_{eff}^2 values are moderately lower than modeled predictions due to complex multilayer interactions in practical devices[1-3]. Crucially, results confirm that retaining the AlN seed layer reduces both composite-film piezoelectricity and device performance, while its removal yields pronounced improvement. Model-derived material parameters (e_{33}, e_{31}, e_{15}) are benchmarked against existing studies (**Table S2**)[3-7], validating predictive capability for bilayer coupling. In the revised manuscript, we have clarified the model's scope and moderated statements about direct experimental fitting to prevent misinterpretation.

Revised Supplementary Information:

Line 391:

FBAR-0, an early-stage test structure fabricated with a retained PVD AlN seed layer, exhibits a low effective electromechanical coupling coefficient of 6.3% and a limited quality factor (Q_{max} =189) in its impedance response (**Fig. S12a**), confirming that the poor crystallinity of the PVD-deposited seed significantly degrades performance. The overall trends in **Fig. S12c** and **S12d** show that devices with MOCVD AlN seeds achieve higher Q than those with PVD seeds, while removing the seed layer further enhances the effective electromechanical coupling coefficient. Statistical comparison in **Fig. S12d**, based on over 100 samples per group, reveals that FBAR-1 operates at a higher resonance frequency than FBAR-0, and FBAR-3 at a higher frequency than

FBAR-2, highlighting the substantial improvement in resonance quality attained with single-crystalline seed layers.

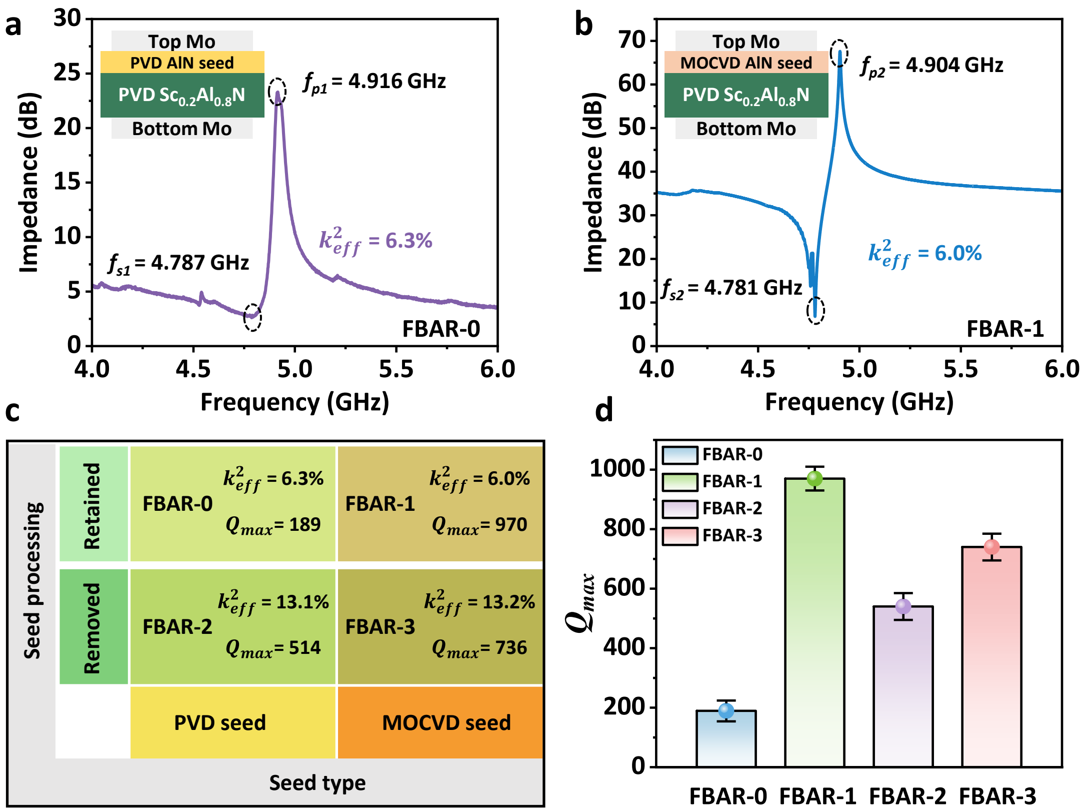

Fig. S12 Electrical characterization of FBARs with different AlN seed conditions. **a** Impedance curve of the FBAR with a retained PVD AlN seed layer, exhibiting k_{eff}^2 =6.3% and a Q_{max}=189. **b** Impedance curve of the FBAR with a retained MOCVD AlN seed layer, exhibiting k_{eff}^2 =6.0% and a maximum quality factor Q_{max}=970. **c** Summary of k_{eff}^2 and Q_{max} in FBARs fabricated with different AlN seed types (PVD or MOCVD) and processing conditions (retained or removed). Devices using MOCVD AlN seeds exhibit consistently higher Q_{max} values than those based on PVD seeds, while removing the AlN seed layer significantly enhances k_{eff}^2 in both cases. **d** Statistical analysis of Q factors for the four FBAR groups.

Table S2 Comparison of calculated and experimental material parameters with literature values for AlN and $Sc_{0.2}Al_{0.8}N$.

Material parameters		Calculation		Experiment	
		This work	Ref.	This work	Ref.
AlN	e_{33} (C/m^2)	1.492	1.471 [a]	1.52	1.55 [c]
	e_{31} (C/m^2)	−0.578	−0.593 [a]	/	−0.58 [c]
	e_{15} (C/m^2)	−0.304	−0.313 [a]	/	−0.48 [c]
	ε_r	9.3	10.31[b]	9.5	9.5 [d]
$Sc_{0.2}Al_{0.8}N$	e_{33} (C/m^2)	1.944	1.942 [a]	2.09	2.08 [e]
	e_{31} (C/m^2)	−0.649	−0.653 [a]	/	/
	e_{15} (C/m^2)	−0.299	−0.273 [a]	/	/
	ε_r	13.33	16.23[b]	13.56	13.42 [e]

[a] See Ref.[4], [b] See Ref.[5], [c] See Ref.[6], [d] See Ref.[7], [e] See Ref.[3]

Reference

1. Gao, C., *et al.* Influence of etching trench on k^2_{eff} of film bulk acoustic resonator. *Micromachines* **13**, 102 (2022).
2. Yang, H., Sun, J., Wang, H., Li, H. & Yang, B. A review of oriented wurtzite-structure aluminum nitride films. *Journal of Alloys and Compounds* **989**, 174330 (2024).
3. Zou, Y., *et al.* Aluminum scandium nitride thin-film bulk acoustic wave resonators for wide-band applications. *Microsystems & Nanoengineering* **8**, 52 (2022).
4. Caro, M. A. *et al.* Erratum: Piezoelectric coefficients and spontaneous polarization of ScAlN (Journal of Physics: Condensed Matter (2015) 27 (245901)). *J. Phys. Condens. Matter* **27**, (2015).
5. Ambacher, O. *et al.* Wurtzite ScAlN, InAlN, and GaAlN crystals, a comparison of structural, elastic, dielectric, and piezoelectric properties. *J. Appl. Phys.* **130**, (2021).
6. Tsubouch, K. & Mikoshiba, N. Zero-Temperature-Coefficient SAW Devices on AlN Epitaxial Films. *IEEE Trans. Sonics Ultrason.* **32**, 634–644 (1985).
7. Zou, J. & Pisano, A. P. Temperature compensation of the AlN Lamb wave resonators utilizing the S1 mode. in *2015 IEEE International Ultrasonics Symposium, IUS 2015* 1–4 (IEEE, 2015). doi:10.1109/ULTSYM.2015.0456.

3. Filter Data and Comparability: The manuscript introduces three stacked filter structures but does not provide specific structural parameters for each layer of FBARs. Furthermore,there is no comparison with simulation data of filters.The manuscript needs to provide detailed layer parameters for the three compared filters in Figure 5 and explain the large frequency discrepancies observed.

Additionally, a comparison between simulated and measured results for the fabricated filters in Figure 5 is missing.

Response to Reviewer:

The design and fabrication of the proposed filters were established through multiple iterative optimizations, forming a progressive evolution from Filter-1 to Filter-3. To enhance clarity, the detailed structural parameters of the three filters, including the thickness of ScAlN/AlN/Mo, and seed-layer processing state (corresponding to the FBARs), have been added in **Supplementary Table S6**.

(1) Origin of frequency differences

The center-frequency variations among the three filters primarily arise from differences in their acoustic stack structures:

Filter-1 retains the AlN seed layer, resulting in a larger total acoustic thickness and thus the lowest operating frequency. In Filter-2 and Filter-3, the AlN seed layer is removed after ScAlN deposition, reducing the total thickness and increasing the frequency. Filter-3 further employs a thinner top electrode, which shortens the acoustic path and yields the highest frequency.

(2) Design and process optimization

This work targets Wi-Fi 6E (5925-7125 MHz) high-frequency and wide-band applications. Preliminary simulations based on 30% ScAlN films demonstrated that only such a high Sc concentration could provide the required electromechanical coupling (K_t^2) to cover the entire 1200 MHz bandwidth, as shown in **Fig. R10**. However, considering the current growth challenges of high-Sc-content films, we first validated the process feasibility and structural optimization using 20% ScAlN, which already exhibits a stable crystalline quality and reproducible fabrication.

During fabrication, a 100 nm SiO_2 buffer layer was introduced to alleviate the large intrinsic stress of the a-Si sacrificial layer. This additional SiO_2, which had not been considered in the initial simulation, increased the total acoustic thickness and thus led to a lower resonant frequency than the designed target. The observed deviation therefore arises from practical process constraints rather than modeling inaccuracy. Meanwhile, the measured FBAR exhibited an effective electromechanical coupling coefficient of only ~6%, corresponding to a filter bandwidth of 320 MHz, which is significantly lower than the theoretical value and suggests that the presence of the AlN seed layer may limit k_{eff}^2 .

Therefore, a rapid verification was conducted using a filter based on a PVD-AlN seed layer (Filter-2). Unlike Filter-1, the AlN seed layer in this device was removed during subsequent processing, resulting in an increased resonance frequency. The corresponding FBAR exhibited an effective k_{eff}^2 of 13.1%, which is close to the theoretical value. However, because the series resonance (f_{s2}) of the series FBAR was slightly lower than the parallel resonance (f_{p1}) of the parallel FBAR, the overall filter bandwidth was smaller than the theoretical prediction.

Based on these results, we recalibrated the simulation model using the measured parameters of FBAR-1 and FBAR-2 and optimized the electrode thickness to achieve accurate frequency matching. The final Filter-3 shows excellent agreement between the measured and simulated transmission responses (**Figs. 5d-f**). Minor discrepancies in insertion loss and stopband level are mainly attributed to unmodeled multiphysics coupling effects that increase acoustic and electrical losses, as well as inevitable process variations. Nevertheless, the close match in center frequency, bandwidth, and passband profile confirms the reliability of both the extracted parameters and the circuit model. In the revised manuscript, the corresponding simulation results of the filters have been added and directly compared with the experimental data in **Figs. 5d-f** to improve completeness and comparability.

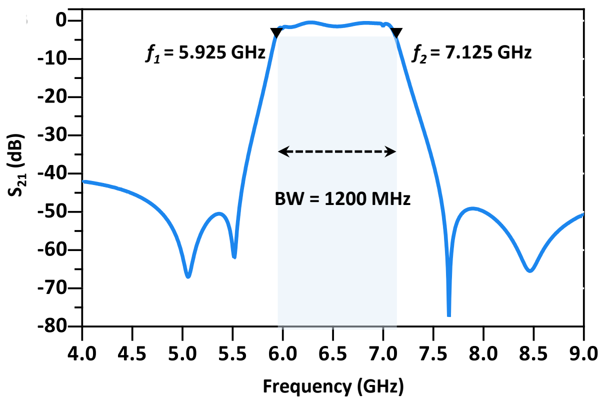

Fig. R10 Simulated transmission response of the $Sc_{0.3}Al_{0.7}N$-based filter designed for the Wi-Fi 6E band.

Revised Main Text:

Line 386:

…The limited bandwidths of Filter-1 and Filter-2 arise from frequency mismatch between the series and parallel resonators. Based on the FBAR-extracted material parameters and the measured stack thicknesses, the simulated responses of Filter-1 and

Filter-2 are recalibrated to reproduce the experimental results. Using these calibrated parameters, as shown in **Fig. 5f,** Filter-3 is redesigned and achieves an insertion loss of −2.6 dB, a 740 MHz bandwidth, and >40 dB rejection (**Fig. 5f**), in good agreement with the optimized simulation. The improvements are attributed to the high-quality $Sc_{0.2}Al_{0.8}N$ film and optimized fabrication, which enhance both passband performance and out-of-band suppression.…

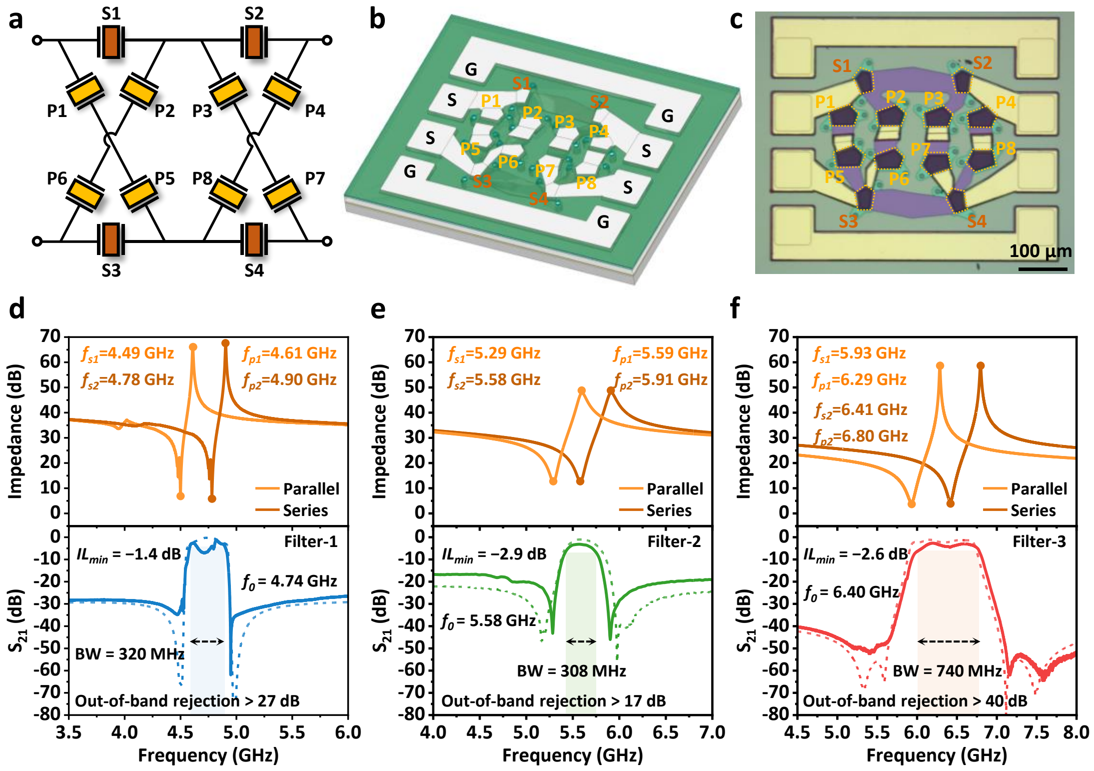

Fig. 5 Experimental results of the fabricated filters. d-f The simulated (dash lines) and measured (solid lines) transmission responses of the filters, along with the impedance curves of the corresponding resonators, for (**d**) Filter-1 (single-crystalline AlN seed layer, retained), (**e**) Filter-2 (polycrystalline AlN seed layer, removed), and (**f**) Filter-3 (single-crystalline AlN seed layer, removed).

<u>Revised Supplementary Information:</u>

Line 383:

Device characterization

Table S6 summarizes the layer-stack thicknesses and processing conditions for the four FBAR devices, all of which maintain identical AlN seed and ScAlN film thicknesses as well as top and bottom Mo electrodes, except for FBAR-3 where the electrodes were strategically thinned to achieve a higher resonance frequency as part of the design-process optimization.

Table S6 Thickness parameters of the FBAR layer stack.

Device	Top Mo	ScAlN	Bottom Mo	AlN seed	Seed processing
FBAR-0	80 nm	280 nm	80 nm	50 nm	PVD AlN (Retained)
FBAR-1	80 nm	280 nm	80 nm	50 nm	MOCVD AlN (Retained)
FBAR-2	80 nm	280 nm	80 nm	50 nm	PVD AlN (Removed)
FBAR-3	65 nm	280 nm	65 nm	50 nm	MOCVD AlN (Removed)

4. Calculation of Piezoelectric Coefficients: The manuscript needs to clearly describe the process for calculating the piezoelectric stress coefficient shown in Figure 1c. Additionally, as Equation 10 indicates that the calculation of the effective electromechanical coupling coefficient (k_{eff}^2) requires resonant and anti-resonant frequencies, the method for obtaining these values must be detailed.

Response to Reviewer:

The composition-dependent piezoelectric coefficients of ScAlN shown in Fig. 1c are derived from first-principles calculations using the Vienna Ab initio Simulation Package (VASP) within the density functional theory (DFT) framework and its linear-response extension, density functional perturbation theory (DFPT), which directly evaluates piezoelectric coefficients at representative $Sc_xAl_{1-x}N$ compositions ($0 \leq x \leq 0.4$)[1-5,] as detailed in the Methods and Supplementary Information. Additionally, resonant (f_s) and anti-resonant (f_p) frequencies were obtained from the simulated impedance-frequency response of the FBAR structure using COMSOL Multiphysics, with full methodological descriptions incorporated into the revised manuscript[6].

Revised Main Text:

Line: 467

Methods: First-principles calculation of piezoelectric stress coefficients

The first-principles calculations are carried out using the Vienna Ab initio Simulation

Package (VASP) within the framework of density functional theory (DFT) and its linear-response extension, the density functional perturbation theory (DFPT)[56–58]. This approach enables direct evaluation of the piezoelectric stress coefficients at several representative compositions of wurtzite $Sc_xAl_{1-x}N$. Calculations are conducted using a 2×2×2 wurtzite supercell containing 32 atoms, with Sc concentrations of 6.25%, 12.5%, 18.75%, 25%, 31.25%, and 37.5%, as shown in **Fig. S1.** For each composition, several inequivalent substitutional configurations are examined, and the lowest-energy structure is adopted for property evaluation. The projector augmented-wave (PAW) method is employed together with the generalized gradient approximation of Perdew-Burke-Ernzerhof (GGA-PBE) for exchange-correlation. A plane-wave cutoff energy is 520 eV, and Brillouin-zone integrations are carried out on a Γ-centered 9×9×3 Monkhorst-Pack *k*-point mesh[59].

Line: 481

Electromechanical modeling of AlN/ScAlN bilayers

…A detailed illustration of the Euler angle settings is provided in **Figs. S1 e-f**. The k_{eff}^2 of the FBAR is extracted from its simulated impedance-frequency response curve according to the equation [62]:

$$k_{eff}^2 = \frac{\pi^2}{4} \cdot \frac{f_s \cdot \left(f_p - f_s\right)}{f_p^{\ 2}} \tag{1}$$

<u>**Revised Supplementary Information:**</u>

Line 20:

First-principles calculation of piezoelectric stress coefficients

Figure S1 shows the wurtzite $Sc_xAl_{1-x}N$ supercell models used for first-principles calculations, where 2×2×2 wurtzite supercells are constructed to model Sc substitution at Al sites with Sc concentrations of 6.25 at.%, 12.5 at.%, 18.75 at.%, 25 at.%, 31.25 at.%, and 37.5 at.%, respectively. The computational settings align with the **Method section** of the main text. The compositional dependence of material properties on Sc concentration, illustrated in **Fig. 1c**, is derived by fitting discrete data points with a quadratic polynomial, as shown in **Table 1**. The calculated material parameters for AlN and $Sc_{0.2}Al_{0.8}N$ show excellent consistency with established literature values (**Table S2**). These parameters are subsequently adopted for FBAR and filter modeling. Experimentally extracted parameters, obtained by fitting measured impedance spectra using the Mason model after device fabrication, exhibit close agreement with simulation inputs and literature data, demonstrating the methodology's accuracy and self-consistency.

Table S1 Calculated piezoelectric stress coefficients of wurtzite $Sc_xAl_{1-x}N$ at different Sc contents.

	AlN	6.25 at.%	12.5 at.%	18.75 at.%	25 at.%	31.25 at.%	37.5 at.%
e_{33} (C/m^2)	1.492	1.543	1.698	1.901	2.152	2.486	2.866
e_{31} (C/m^2)	−0.578	−0.592	−0.621	−0.644	−0.670	−0.724	−0.775
e_{15} (C/m^2)	−0.304	−0.303	−0.301	−0.299	−0.299	−0.298	−0.297

The compositional dependence of e_{ij} on Sc concentration is obtained by fitting the discrete data points with a quadratic polynomial:

$$e_{15}(x) = -0.2984x - 0.3043(1-x) + 0.0245x(1-x) \tag{2}$$

$$e_{31}(x) = -1.6800x - 0.5781(1-x) + 0.9281x(1-x) \tag{3}$$

$$e_{33}(x) = 10.0304x + 1.4815(1-x) - 7.7945x(1-x) \tag{4}$$

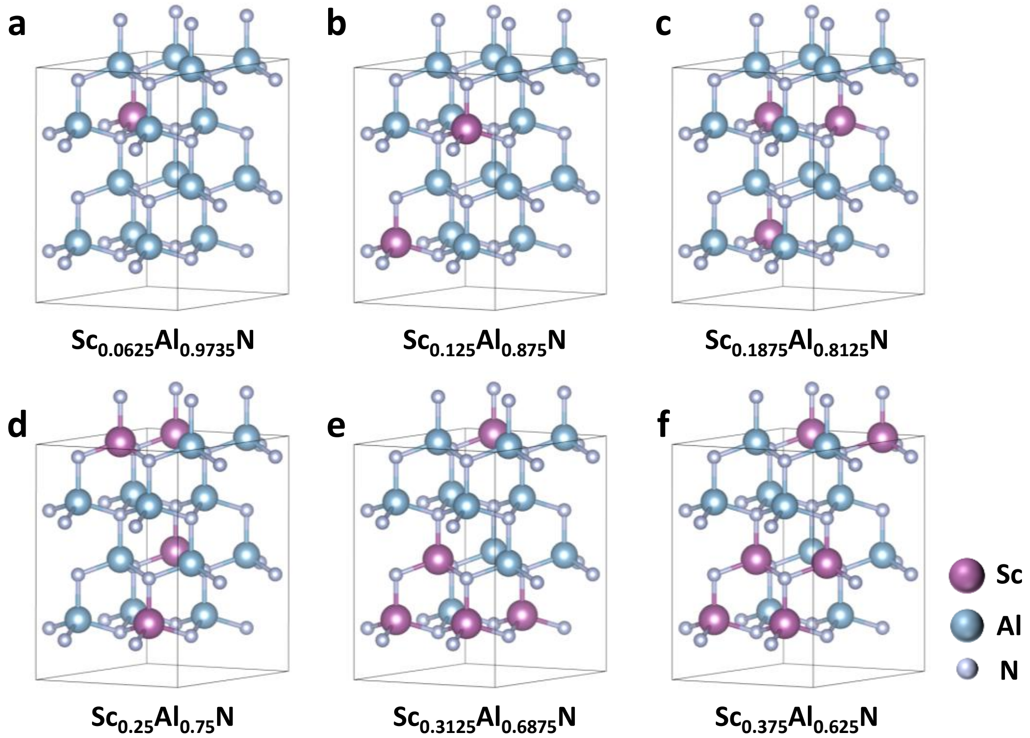

Fig. S1 Wurtzite $Sc_xAl_{1-x}N$ supercell models used for first-principles calculations. a-f 2×2×2 wurtzite supercells are constructed to model Sc substitution at Al sites with Sc concentrations of 6.25 at.%, 12.5 at.%, 18.75 at.%, 25 at.%, 31.25 at.%, and 37.5 at.%, respectively.

Table S2 Comparison of calculated and experimental material parameters with literature values for AlN and $Sc_{0.2}Al_{0.8}N$.

Material parameters		Calculation		Experiment	
		This work	Ref.	This work	Ref.
AlN	e_{33} (C/m^2)	1.492	1.471 [a]	1.52	1.55 [c]
	e_{31} (C/m^2)	−0.578	−0.593 [a]	/	−0.58 [c]
	e_{15} (C/m^2)	−0.304	−0.313 [a]	/	−0.48 [c]
	ε_r	9.3	10.31 [b]	9.5	9.5 [d]
$Sc_{0.2}Al_{0.8}N$	e_{33} (C/m^2)	1.944	1.942 [a]	2.09	2.08 [e]
	e_{31} (C/m^2)	−0.649	−0.653 [a]	/	/
	e_{15} (C/m^2)	−0.299	−0.273 [a]	/	/
	ε_r	13.33	16.23 [b]	13.56	13.42 [e]

[a] See Ref.[1], [b] See Ref.[2], [c] See Ref.[3], [d] See Ref.[4], [e] See Ref.[5]

References

1. Caro, M. A. *et al.* Erratum: Piezoelectric coefficients and spontaneous polarization of ScAlN (Journal of Physics: Condensed Matter (2015) 27 (245901)). *J. Phys. Condens. Matter* **27**, (2015).
2. Ambacher, O. *et al.* Wurtzite ScAlN, InAlN, and GaAlN crystals, a comparison of structural, elastic, dielectric, and piezoelectric properties. *J. Appl. Phys.* **130**, (2021).
3. Tsubouch, K. & Mikoshiba, N. Zero-Temperature-Coefficient SAW Devices on AlN Epitaxial Films. *IEEE Trans. Sonics Ultrason.* **32**, 634–644 (1985).
4. Zou, J. & Pisano, A. P. Temperature compensation of the AlN Lamb wave resonators utilizing the S1 mode. in *2015 IEEE International Ultrasonics Symposium, IUS 2015* 1–4 (IEEE, 2015). doi:10.1109/ULTSYM.2015.0456.
5. Zou, Y. *et al.* Aluminum scandium nitride thin-film bulk acoustic resonators for 5G wideband applications. *Microsystems Nanoeng.* **8**, (2022).
6. Bi, F. Z. & Barber, B. P. Bulk acoustic wave RF technology. *IEEE Microw. Mag.* **9**, 65–80 (2008).

5. Euler Angles and Polarization: In line 488, the manuscript states, "Polarization orientation is controlled by assigning Euler angles to each layer." A clear explanation of how Euler angles affect polarization orientation is required. Furthermore, the role and meaning of the (0,180°,0) Euler angles depicted on the right side of Figure S1c need to be clarified, as the 180° rotation is not evident from the figure.

Response to Reviewer:

We agree that the original explanation of the relationship between Euler angles and polarization was too brief, and we have added a more detailed clarification in the revised manuscript. In wurtzite piezoelectric materials such as AlN and ScAlN, the polarization direction is defined by the crystallographic *c*-axis. When the *c*-axis points along +*Z*, the film exhibits one polarity (commonly referred to as Al-polarity); when it points along −*Z*, the opposite polarity (N-polarity) is obtained. In COMSOL, the piezoelectric tensors are defined in the crystal coordinate system, and the Euler angles specify the rotation of this system relative to the global coordinates, as shown in **Fig. R11**. Thus, by assigning Euler angles, the direction of the *c*-axis in the global coordinate system can be directly adjusted, thereby enabling control of the polarization orientation.

Specifically, under Z-X-Z convention in COMSOL, the Euler angle set (α, β, γ) = (0°, 180°, 0°) corresponds to a 180° rotation about the X axis. This operation flips the *c*-axis from +Z to −Z, thereby reversing the signs of the relevant piezoelectric coefficients (e_{33}, e_{31}, e_{15}) and inverting the polarization. Since α and γ are set to 0°, no additional in-plane rotation is introduced, and the sole effect of (0°,180°,0°) is the *c*-

axis inversion. We have revised **Fig. S2** to explicitly illustrate the *c*-axis flip corresponding to (0°,180°,0°).

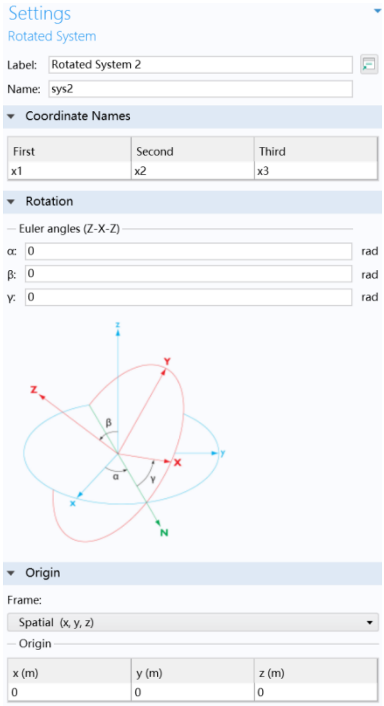

Fig. R11 Definition of the rotated coordinate system in COMSOL.

Revised Supplementary Information:

Polarization orientation setting based on Euler angles in finite element simulation model by COMSOL

To evaluate the influence of polarization orientation on the electromechanical coupling performance of the FBAR device, a three-dimensional finite element model is established, as shown in **Fig. S2c**. The simulated multilayer structure consists of the Mo electrode, an AlN seed layer, and a $Sc_{0.2}Al_{0.8}N$ piezoelectric layer. In COMSOL, the piezoelectric tensors are defined in the crystal coordinate system, and Euler angles specify the rotation of this system relative to the global coordinates. By assigning Euler angles, the orientation of the *c*-axis in the global frame can be directly controlled, thereby determining the polarization direction, as shown in **Figs. S2e-f**. Under the Z-X-Z convention, the Euler angle set (α, β, γ) = (0°, 0°, 0°) corresponds to the default Al-polar orientation with the *c*-axis along +Z, while (0°, 180°, 0°) corresponds to a 180° rotation about the X axis, which flips the *c*-axis from +Z to −Z and yields the opposite N-polar orientation.

Two polarization configurations are therefore considered in the simulations. In the parallel configuration, both the AlN and ScAlN layers are set to the Al-polar orientation (0°, 0°, 0°). In contrast, in the antiparallel configuration, the AlN layer remains Al-polar (0°, 0°, 0°), while the ScAlN layer is rotated to (0°, 180°, 0°), resulting in its *c*-axis inversion to −Z (N-polar). These two configurations enable direct comparison between parallel and antiparallel polarization states. The simulations are performed to evaluate the variation of the effective electromechanical coupling coefficient (k_{eff}^2) of FBARs under different polarization configurations and volume ratios of AlN to ScAlN.

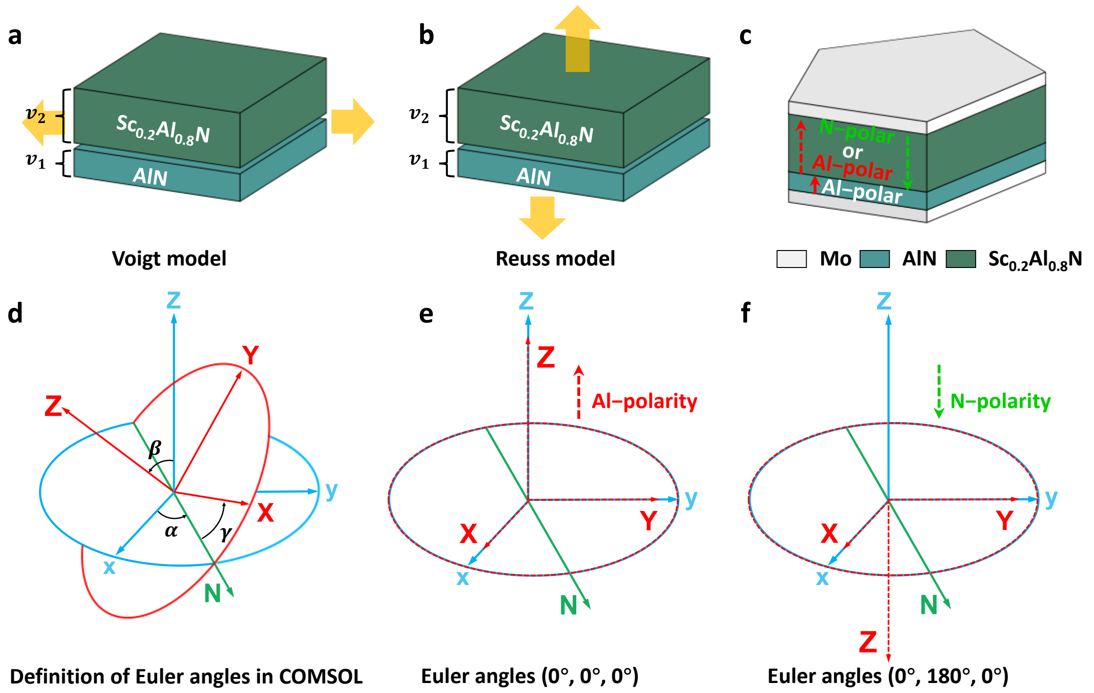

Fig. S2 Theoretical model of the FBAR. **c** Schematic of the FBAR with the bilayer structure of AlN and ScAlN. **d** Definition of Euler angles in COMSOL (Z-X-Z convention). **e** Orientation with Euler angles (0°,0°,0°), where the *c*-axis aligns with +Z, corresponding to the Al-polarity. **f** Orientation with Euler angles (0°,180°,0°), where the *c*-axis aligns with −Z, corresponding to the N-polarity.

6. Acoustic Confinement by AlN Seed Layer: Figure 4e's caption mentions, "The presence of the intact AlN seed layer provides additional acoustic confinement, thereby suppressing energy dissipation." It is recommended to include simulation results in the manuscript to substantiate the claim that the single-crystal AlN layer confines energy dissipation.

Response to Reviewer:

We acknowledge the reviewer's critical observation regarding the term "acoustic confinement" in **Fig. 4e** and confirm that this description was imprecise. It has been rectified throughout the revised manuscript to accurately reflect that the MOCVD-grown single crystalline AlN seed layer enhances resonator Q by minimizing lattice defects and grain boundary dissipation in the epitaxially grown ScAlN overlayer through superior crystalline coherence, not via physical acoustic wave confinement. While retaining the AlN seed layer improves ScAlN crystallinity, it introduces detrimental trade-offs: (1) AlN's lower intrinsic K_t^2 (~6.5%) reduces overall electromechanical efficiency, and (2) polarity inversion at the AlN/ScAlN bilayers further degrades k_{eff}^2. To resolve this, our dual strategy leverages the MOCVD-AlN template for defect-minimized ScAlN epitaxy during deposition while post-growth removal eliminates polarity mismatch. The empirical superiority of this approach is demonstrated by FBAR-3's optimized performance: 740 MHz bandwidth, k_{eff}^2 of 13.2%, and Q_{max} of 736 at over 6 GHz, validating that strategic seed layer removal maximizes piezoelectric response without compromising crystalline quality.

Revised Main Text:

Line 336:

…FBAR-1 achieves the highest Q_{max} of 970, attributed to the high crystalline quality and reduced defect density of the $Sc_{0.2}Al_{0.8}N$ film grown on single-crystalline AlN. Comparatively, FBAR-2 exhibits a significantly lower Q_{max} of 514 due to poor crystallinity in $Sc_{0.2}Al_{0.8}N$ deposited on polycrystalline AlN, where random grain orientations disrupt *c*-axis alignment, causing stress inhomogeneity and anisotropic deformation. These microstructural irregularities act as scattering centers, increasing propagation losses[17,19,44]. FBAR-3 employs the same single-crystalline AlN seed as FBAR-1 but undergoes post-deposition AlN removal, yielding a Q_{max} of 736. **Consequently, the Q_{max} of FBAR-3 is slightly lower than that of FBAR-1, primarily attributed to the >6 GHz operating frequency that induces severe acoustic energy dissipation[45,46].** Nevertheless, FBAR-3 achieves about 43% higher Q_{max} than FBAR-2 and delivers the highest FOM of 97, demonstrating superior overall performance.

7. Discrepancy in Electromechanical Coupling Coefficients and Filter Bandwidth:

In Figure 4d, FBAR 2 and FBAR 3, which correspond to resonators with the polycrystalline AlN and single-crystalline AlN seed layer removed respectively, exhibit almost identical effective electromechanical coupling coefficients. However, the filters based on these resonators (Figures 5e and 5f, corresponding to the removal of polycrystalline AlN and single crystalline AlN, respectively) show a very large difference in bandwidth. The reasons for this significant discrepancy need to be thoroughly explained.

Response to Reviewer:

Although FBAR-2 and FBAR-3 show nearly identical k_{eff}^2 values, the bandwidths of their corresponding filters differ substantially due to differences in frequency matching between the series and parallel resonators and the overall stack configuration.

These filters adopt a lattice-type topology, in which the passband is determined by the frequency alignment between the series-resonant frequency (f_{s2}) of the series FBARs and the parallel-resonant frequency (f_{p1}) of the parallel FBARs. In an ideal condition, when the parallel FBAR's $f_{s2} = f_{p1}$, the passband exhibits minimal ripple and maximum flatness, shown in **Fig. R12**. When $f_{s2} < f_{p1}$, the passband becomes compressed, resulting in a reduced bandwidth; conversely, when $f_{s2} > f_{p1}$, the bandwidth widens but at the cost of increased ripple.

As discussed in **Comment 3**, Filter-2 was designed to verify the influence of removing the AlN seed layer on the electromechanical coupling. The removal of the AlN layer slightly altered the total stack thickness and shifted the resonant frequencies, leading to an imperfect frequency match $f_{s2} < f_{p1}$ and thus a narrower passband.

In this work, the filters mainly serve to demonstrate how FBAR-level material and structural differences translate into system-level performance. The comparison between Filter-2 and Filter-3 emphasizes the influence of the AlN seed-layer crystallinity on insertion loss: Filter-2 (polycrystalline seed) exhibits –3.1 dB insertion loss, whereas Filter-3 (single-crystalline seed) benefits from improved film quality and Q factor, lowering the loss to –2.6 dB.

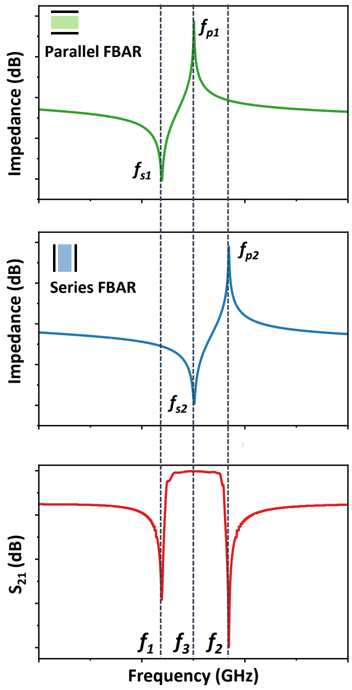

Fig. R12 Simulated transmission response of the filter and its correlation with individual FBAR units.

8. Polarity Inversion in ScAlN: Regarding Figure 1 (Crystal structure, polarization characteristics, and piezoelectric properties of AlN and ScAlN films), the manuscript should clarify the conditions under which the polarity of ScAlN inverts. The implication that any minor Sc doping would cause polarity flipping requires further physical justification.

Response to Reviewer:

We thank the reviewer for raising this important point about polarity inversion in ScAlN. After reassessing our wording and comparing with recent reports, we clarified the manuscript to avoid implying that small amounts of Sc automatically flip polarity. Experimental evidence indicates that polarity in AlN/ScAlN systems is a multi-factor phenomenon: while Sc incorporation modifies lattice parameters, bonding configurations, and surface kinetics and therefore can influence polarity stability[1-5], it is not by itself a sufficient or universally dominant trigger for polarity inversion. Instead, polarity outcomes are strongly governed by interfacial and growth conditions. For example, seed-layer/template polarity, substrate surface chemistry and energy, ion bombardment or substrate bias during sputtering, residual stress and impurity/oxygen diffusion at interfaces, which can directly induce inversion or stabilize a given polarity state. Notably, polarity inversion of ScAlN has been demonstrated under substrate ion-beam irradiation and other processing-dependent conditions, and Si-doping has also been reported to invert AlN polarity under specific doping levels and growth recipes. Therefore, we have revised the manuscript to emphasize that Sc content is an important intrinsic factor but not the sole or necessarily decisive parameter. Polarity inversion in practice results from a complex interplay of intrinsic composition and extrinsic growth/interfacial conditions. A systematic exploration of the precise Sc concentration thresholds and the specific growth parameter windows that produce polarity switching is beyond the scope of this work but is an important direction for future theoretical and experimental studies.

References

1. Suzuki, M., Yanagitani, T. & Odagawa, H. Polarity-inverted ScAlN film growth by ion beam irradiation and application to overtone acoustic wave (000–1)/(0001) film resonators. *Applied Physics Letters* **104**, 172905 (2014).
2. Anggraini, S. A., Takeuchi, M., Inoue, S. *et al.* Polarity inversion of aluminum nitride thin films by using Si doping. *Scientific Reports* **10**, 12836 (2020).
3. Jiang, K., Hu, J., Luo, Y. *et al.* AlN lattice-polarity inversion in high-temperature-annealed c-oriented AlN/sapphire originated from diffusion of Al and O atoms from sapphire. *Nanoscale Advances* **5**, 4800–4808 (2023).
4. Mondal, S., Zukauskaite, A., Lin, Y. C. *et al.* Polarity-controlled ScAlN multilayer transduction structures. *Applied Physics Letters* **125**, 172903 (2024).
5. Shojiki, K., Nishihara, T., Yanagitani, T. *et al.* Polarity control of sputter-deposited AlN with high-quality crystal. *Japanese Journal of Applied Physics* **62**, SJ1001 (2023).

9. Comparison of AlN Seed Layers: For Figure S2, which compares X-ray rocking curves of AlN seed layers deposited by PVD and MOCVD, it would be beneficial to also compare the crystallinity of MOCVD-grown AlN with thin Mo electrode as the guide layer versus MOCVD-grown AlN directly on Si.

Response to Reviewer:

We have supplemented the new manuscript with data on Mo's impact on thin-film properties, including direct ScAlN growth on Mo, and growth on Mo deposited on either PVD or MOCVD AlN seed layers before ScAlN deposition. While in the Mo/AlN/ScAlN stack configuration with a retained AlN seed layer, the interfacial AlN inevitably reduces the effective electromechanical coupling (k_{eff}^2) compared to a pure ScAlN structure, this architecture is essential for leveraging MOCVD-grown epitaxial single-crystalline AlN seed layers on Si (111), which enable high-quality c-axis oriented ScAlN growth and consequently high-Q FBARs. Critically, AlN's hexagonal symmetry achieves excellent lattice matching with Si (111) triangular surface lattice, whereas Mo's bcc structure exhibits rectangular symmetry in its (110) plane; this structural incompatibility prevents commensurate epitaxial alignment for wurtzite AlN/ScAlN, and direct ScAlN nucleation on polycrystalline Mo, which would occur if Mo were positioned between AlN and ScAlN, resulting in significantly degraded crystallinity.

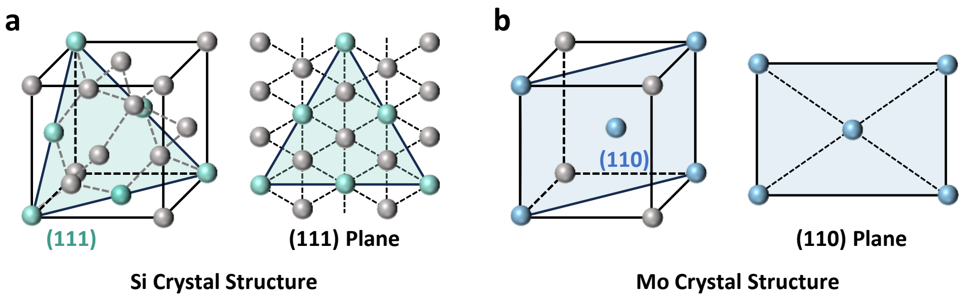

Fig. R13 Crystal structures of Si (111) and Mo (110) planes. a Si has a diamond-cubic structure, and the (111) plane exhibits an equilateral triangular lattice. **b** Mo has a body-centered cubic (bcc) structure, and the (110) plane exhibits a rectangular lattice.

(1) Thin-film quality comparison

During the initial stage of thin-film development we systematically examined the influence of Mo and AlN seed layers on the crystalline quality of ScAlN. As shown in **Fig. R14**, four samples were fabricated for comparison. In Sample 1 (**Fig. R14a**), a 60 nm-thick Mo electrode was sputtered on Si, followed by 280 nm-thick ScAlN. In Sample 2 (**Fig. R14**b), a 50 nm-thick PVD AlN seed layer and a 60 nm-thick Mo electrode were sputtered sequentially on Si, followed by 280 nm-thick ScAlN. In Sample 3 (**Fig. R14c**), a 50 nm-thick MOCVD AlN seed layer was epitaxially grown on Si, on top of which a 60 nm-thick Mo electrode and 280 nm-thick ScAlN were deposited. In Sample 4 (**Fig. R14d**), a 50 nm-thick MOCVD AlN seed layer was epitaxially grown on Si, followed directly by 280 nm ScAlN without Mo. The X-ray rocking-curve FWHM values were 2.6°, 2.3°, 1.4°, and 0.94°, respectively. These results clearly show that direct epitaxy of ScAlN on MOCVD AlN yields the best crystalline quality (FWHM 0.94°), which is the approach adopted in this work.

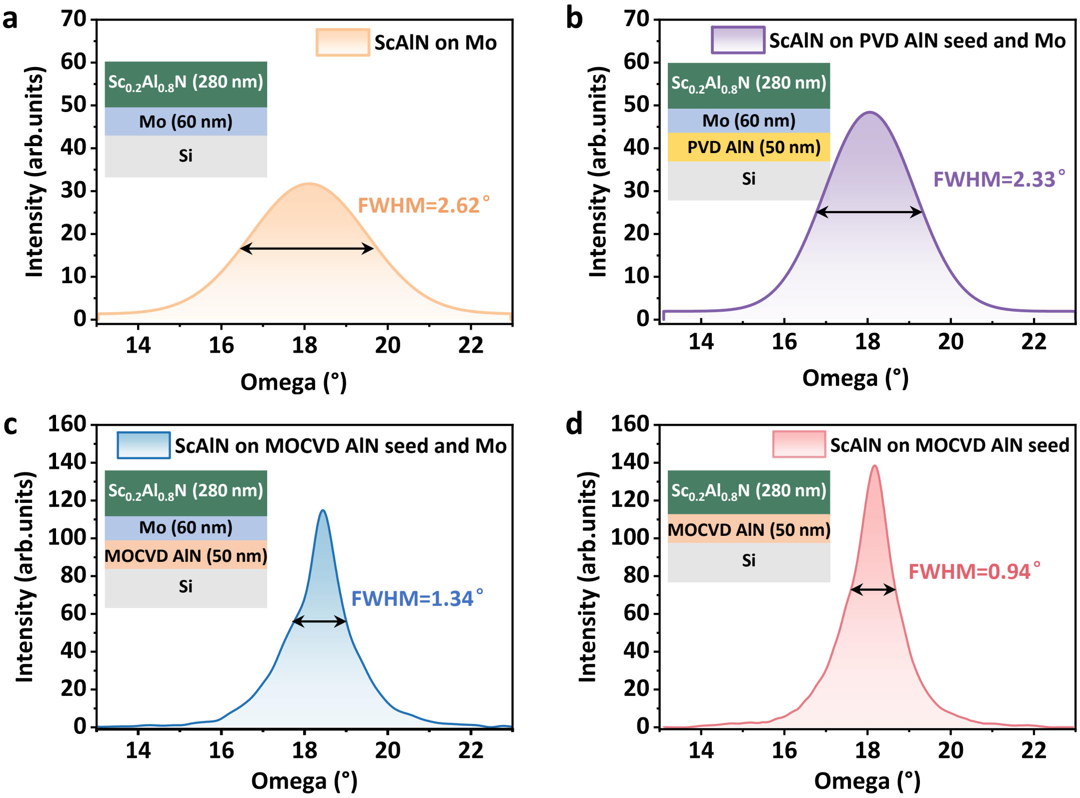

Fig. R14 (Fig. S6 in the newly revised Supplementary Information) X-ray rocking curve of the 280 nm-thick $Sc_{0.2}Al_{0.8}N$ film. a 280 nm-thick $Sc_{0.2}Al_{0.8}N$ deposited on a 60 nm-thick Mo layer on Si, FWHM = 2.62°. **b** 280 nm-thick $Sc_{0.2}Al_{0.8}N$ deposited on 60 nm-thick Mo with a 50 nm-thick PVD AlN seed layer on Si, FWHM = 2.33°. **c** 280 nm-thick $Sc_{0.2}Al_{0.8}N$ deposited on 60 nm-thick Mo with a 50 nm-thick MOCVD AlN seed layer on Si, FWHM = 1.34°. **d** 280 nm-thick $Sc_{0.2}Al_{0.8}N$ deposited directly on a 50 nm-thick MOCVD AlN seed layer on Si without Mo, FWHM = 0.94°.

(2) Device performance comparison

Our prior work explored FBARs based on the AlN/Mo/ScAlN stack, yet their quality factors remained constrained. For instance, Ref. [1] reported a 4.3 GHz FBAR with this configuration achieving Q_s=150, Q_p=318, and a figure of merit (FOM) of 62. In contrast, by leveraging epitaxial AlN/ScAlN films and a thin-film transfer process, our optimized FBAR-3 devices operating at 6.4 GHz attained significantly enhanced values of Q_s=192, Q_p=719, and a FOM of 97. These results confirm that single-crystalline AlN films provide superior epitaxial templating, thereby improving ScAlN crystalline quality and ultimately enhancing resonator Q factors.

To avoid a decrease in K_t^2 while obtaining a higher Q value, we developed and validated an etching process to selectively remove the AlN seed layer after transfer when required. Using inductively coupled plasma (ICP) etching with in-situ optical emission spectroscopy (OES) endpoint detection, we reliably identify the transition from AlN to ScAlN through the change in reaction-product emission intensity. This non-destructive method ensures precise termination at the interface without damaging the underlying ScAlN, and has been demonstrated to be both repeatable and reliable.

In conclusion, the single-crystalline AlN seed layer enables high-quality ScAlN growth with enhanced Q factors, while selective removal of this seed layer achieves favorable polarity alignment and restores high k_{eff}^2 and Q values. This dual-optimization approach provides an effective and reliable pathway for optimizing high-frequency FBAR performance.

Revised Supplementary Information:

Line 255:

Effect of Mo electrode and AlN seed layers on ScAlN crystallinity

As shown in **Fig. S6**, XRD rocking curves of the (002) reflection exhibit variations in the FWHM values among the samples. The ScAlN film grown directly on Mo exhibits a broad FWHM of 2.62°, indicating relatively poor crystallinity due to the polycrystalline nature and lattice mismatch at the Mo/ScAlN interface. When a PVD AlN seed layer is introduced between Mo and ScAlN, the FWHM decreases to 2.33°, suggesting partial improvement in orientation. A more substantial enhancement is observed for ScAlN deposited on a MOCVD AlN seed layer. The FWHM is reduced to 1.34° when a Mo electrode is present, and further decreases to 0.94° when ScAlN is directly grown on MOCVD AlN without Mo. These results demonstrate that the presence and crystallinity of the AlN seed layer play a decisive role in promoting highly *c*-axis oriented ScAlN growth. In particular, the single-crystalline MOCVD AlN template provides an optimal lattice environment and effectively suppresses grain-tilt dispersion, leading to the best overall film quality. Therefore, the subsequent section investigates the crystalline quality of AlN seed layers prepared by PVD and MOCVD.

References

1. Zou, Y., *et al*. Aluminum scandium nitride thin-film bulk acoustic resonators for 5G wideband applications. *Microsyst. Nanoeng.* 8, 124 (2022).

10. Filter Performance Benchmarking: The reported lattice-type filter demonstrates a center frequency of 6.4 GHz, a minimum insertion loss of -2.6 dB,

a 3 dB bandwidth of 740 MHz, and out-of-band rejection exceeding 40 dB. When compared to the metrics of existing ScAlN filter, the insertion loss and bandwidth of the presented device do not appear to offer a significant advantage. This should be discussed.

Response to Reviewer:

We sincerely appreciate the reviewer's insightful comment regarding the comparative performance of our lattice-type filter. We acknowledge that the insertion loss (−2.6 dB) achieved in this work is competitive within the landscape of high-frequency (>6 GHz) ScAlN filters rather than representing a singular breakthrough in that specific metric, as benchmarked in Table 2. However, we wish to clarify that the primary focus of this research was to systematically investigate and demonstrate the impact of enhanced thin-film quality on resonator and filter performance. Crucially, the filter presented here achieves a distinctive combination of high operational frequency (6.4 GHz), low insertion loss, and a notably wide -3 dB bandwidth of 740 MHz, alongside robust out-of-band rejection exceeding 40 dB. This bandwidth represents a significant improvement relative to comparable high-frequency ScAlN filters documented in prior literature.

It is important to emphasize that optimizing acoustic filter performance involves complex interdependencies, including operating frequency, thin-film quality, device architecture, circuit matching, and electromagnetic compatibility. Achieving substantial reductions in insertion loss at frequencies exceeding 6 GHz is fundamentally challenging. Our approach centered on enhancing resonator Q through the strategic deployment of an MOCVD-grown single-crystalline AlN template. This enabled the epitaxial growth of a ScAlN overlayer with superior crystallinity, minimizing lattice defects and grain boundary dissipation as a crystalline coherence strategy distinct from wave confinement methods. The resultant performance metrics comprehensively validate the efficacy of this film-centric approach for Q enhancement. We agree that further optimization is attainable. Future work will focus on iterative process refinement, substrate engineering, and advanced packaging architectures to drive additional performance gains in insertion loss and overall filter response.

Specific Points Requiring Minor Revision:

1. Atomic Structure Labeling: The atomic structure of ScAlN labeled in Fig. 1b appears to be that of ScN. This needs to be corrected.

Response to Reviewer:

In the original manuscript, the schematic of the ScAlN structure (**Fig. 1b**) adopted a Sc-centered representation, which might have caused confusion with the ScN structure. In the revised version, the atomic configuration has been redrawn using N-centered tetrahedra to clearly represent the wurtzite-type coordination in both AlN and ScAlN layers.

Revised Main Text:

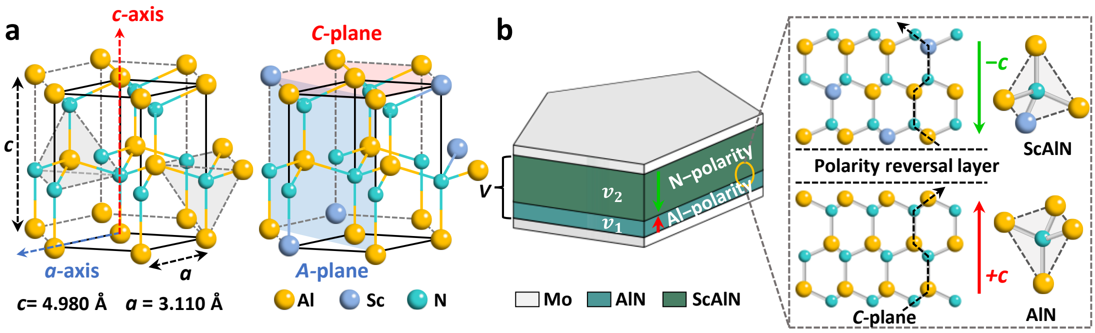

Fig. 1 (Newly revised in the manuscript) Crystal structure, polarization characteristics, and piezoelectric properties of AlN and ScAlN films. a Atomic structures of AlN and ScAlN, showing the *c*-axis polarization and hexagonal symmetry. **b** Schematic of the FBAR with the bilayer structure of AlN and ScAlN, highlighting polarity orientations and the polarity reversal layer.

Reviewer #3 (Remarks to the Author):

Expertise: acoustic resonators, surface acoustic waves

In this manuscript, the authors significantly improved the crystalline quality of low-temperature PVD-grown ScAlN films by introducing an AlN single-crystal seed layer grown by MOCVD. Combined with theoretical model analysis, film characterization, and FBAR device verification, they elucidate the effects of the quality and polarity of the AlN seed layer on the microstructure and electromechanical coupling characteristics of the ScAlN films. This work provides a feasible and scalable technical path for realizing high-performance wideband filters in the frequency band below 7 GHz. This manuscript needs to be revised before it can be accepted for publication.

Response to Reviewer:

We sincerely thank the reviewer for their positive recognition of our work and their insightful comments. In response to the suggestion for revision, we will further clarify the correlation between the theoretical models and experimental results, especially regarding how the crystallinity and polarity of the MOCVD-grown AlN seed layer synergistically influence the electromechanical performance of ScAlN-based FBARs. Additionally, we have elaborated on the scalability and practical implications of the proposed dual-optimization strategy for sub-7 GHz wideband filter applications, and ensure that all methodological details and comparative analyses are explicitly highlighted to enhance the reproducibility and impact of the study. We hope this revised response meets the high standards of the reviewers and the journal.

The questions are as follows:

1. For the variation of piezoelectric constants in ScAlN films with Sc concentration shown in Figure 1c, please explain the calculation method used.

Response to Reviewer:

The composition-dependent piezoelectric coefficients of ScAlN shown in **Fig. 1c** are derived from first-principles calculations using the Vienna Ab initio Simulation Package (VASP) within the density functional theory (DFT) framework and its linear-response extension, density functional perturbation theory (DFPT), which directly evaluates piezoelectric coefficients at several representative compositions of wurtzite $Sc_xAl_{1-x}N$ ($0 \leq x \leq 0.4$), as detailed in the revised main text and Supplementary Information[1-5]. Additionally, theoretical calculations are benchmarked against experimental measurements and prior studies in **Table S2** to explicitly confirm computational accuracy.

Revised Main Text:

Line: 467

Methods: First-principles calculation of piezoelectric stress coefficients

The first-principles calculations are carried out using the Vienna Ab initio Simulation Package (VASP) within the framework of density functional theory (DFT) and its linear-response extension, the density functional perturbation theory (DFPT)[56–58]. This approach enables direct evaluation of the piezoelectric stress coefficients at several representative compositions of wurtzite $Sc_xAl_{1-x}N$. Calculations are conducted using a 2×2×2 wurtzite supercell containing 32 atoms, with Sc concentrations of 6.25%, 12.5%, 18.75%, 25%, 31.25%, and 37.5%, as shown in **Fig. S1.** For each composition, several inequivalent substitutional configurations are examined, and the lowest-energy structure is adopted for property evaluation. The projector augmented-wave (PAW) method is employed together with the generalized gradient approximation of Perdew-Burke-Ernzerhof (GGA-PBE) for exchange-correlation. A plane-wave cutoff energy is 520 eV, and Brillouin-zone integrations are carried out on a Γ-centered 9×9×3 Monkhorst-Pack k-point mesh[59].

Revised Supplementary Information:

Line 20:

First-principles calculation of piezoelectric stress coefficients

Figure S1 shows the wurtzite $Sc_xAl_{1-x}N$ supercell models used for first-principles calculations, where 2×2×2 wurtzite supercells are constructed to model Sc substitution at Al sites with Sc concentrations of 6.25 at.%, 12.5 at.%, 18.75 at.%, 25 at.%, 31.25 at.%, and 37.5 at.%, respectively. The computational settings align with the **Method section** of the main text. The compositional dependence of material properties on Sc concentration, illustrated in **Fig. 1c**, is derived by fitting discrete data points with a quadratic polynomial, as shown in **Table 1**. The calculated material parameters for AlN and $Sc_{0.2}Al_{0.8}N$ show excellent consistency with established literature values (**Table S2**). These parameters are subsequently adopted for FBAR and filter modeling. Experimentally extracted parameters, obtained by fitting measured impedance spectra using the Mason model after device fabrication, exhibit close agreement with simulation inputs and literature data, demonstrating the methodology's accuracy and self-consistency.

Table S1 Calculated piezoelectric stress coefficients of wurtzite $Sc_xAl_{1-x}N$ at different Sc contents.

	AlN	6.25 at.%	12.5 at.%	18.75 at.%	25 at.%	31.25 at.%	37.5 at.%
e_{33} (C/m^2)	1.492	1.543	1.698	1.901	2.152	2.486	2.866
e_{31} (C/m^2)	−0.578	−0.592	−0.621	−0.644	−0.670	−0.724	−0.775
e_{15} (C/m^2)	−0.304	−0.303	−0.301	−0.299	−0.299	−0.298	−0.297

The compositional dependence of e_{ij} on Sc concentration is obtained by fitting the discrete data points with a quadratic polynomial:

$$e_{15}(x) = -0.2984x - 0.3043(1-x) + 0.0245x(1-x) \quad (5)$$

$$e_{31}(x) = -1.6800x - 0.5781(1-x) + 0.9281x(1-x) \quad (6)$$

$$e_{33}(x) = 10.0304x + 1.4815(1-x) - 7.7945x(1-x) \quad (7)$$

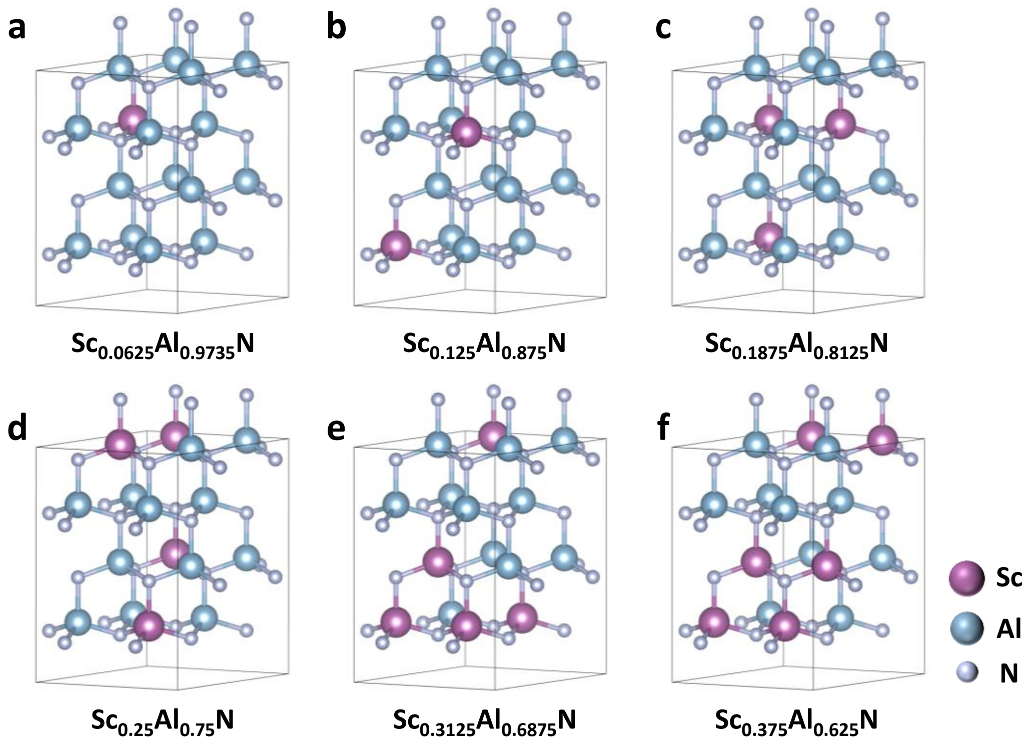

Fig. S1 Wurtzite $Sc_xAl_{1-x}N$ supercell models used for first-principles calculations.

a-f 2×2×2 wurtzite supercells are constructed to model Sc substitution at Al sites with Sc concentrations of 6.25 at.%, 12.5 at.%, 18.75 at.%, 25 at.%, 31.25 at.%, and 37.5 at.%, respectively.

Table S2 Comparison of calculated and experimental material parameters with literature values for AlN and $Sc_{0.2}Al_{0.8}N$.

Material parameters		Calculation		Experiment	
		This work	Ref.	This work	Ref.
AlN	e_{33} (C/m^2)	1.492	1.471 [a]	1.52	1.55 [c]
	e_{31} (C/m^2)	−0.578	−0.593 [a]	/	−0.58 [c]
	e_{15} (C/m^2)	−0.304	−0.313 [a]	/	−0.48 [c]
	ε_r	9.3	10.31[b]	9.5	9.5 [d]
$Sc_{0.2}Al_{0.8}N$	e_{33} (C/m^2)	1.944	1.942 [a]	2.09	2.08 [e]
	e_{31} (C/m^2)	−0.649	−0.653 [a]	/	/
	e_{15} (C/m^2)	−0.299	−0.273 [a]	/	/
	ε_r	13.33	16.23[b]	13.56	13.42 [e]

[a] See Ref.[1], [b] See Ref.[2], [c] See Ref.[3], [d] See Ref.[4], [e] See Ref.[5]

References

1. Caro, M. A. *et al.* Erratum: Piezoelectric coefficients and spontaneous polarization of ScAlN (Journal of Physics: Condensed Matter (2015) 27 (245901)). *J. Phys. Condens. Matter* **27**, (2015).
2. Ambacher, O. *et al.* Wurtzite ScAlN, InAlN, and GaAlN crystals, a comparison of structural, elastic, dielectric, and piezoelectric properties. *J. Appl. Phys.* **130**, (2021).
3. Tsubouch, K. & Mikoshiba, N. Zero-Temperature-Coefficient SAW Devices on AlN Epitaxial Films. *IEEE Trans. Sonics Ultrason.* **32**, 634–644 (1985).
4. Zou, J. & Pisano, A. P. Temperature compensation of the AlN Lamb wave resonators utilizing the S1 mode. in *2015 IEEE International Ultrasonics Symposium, IUS 2015* 1–4 (IEEE, 2015). doi:10.1109/ULTSYM.2015.0456.
5. Zou, Y. *et al.* Aluminum scandium nitride thin-film bulk acoustic resonators for 5G wideband applications. *Microsystems Nanoeng.* **8**, (2022).
6. Bi, F. Z. & Barber, B. P. Bulk acoustic wave RF technology. *IEEE Microw. Mag.* **9**, 65–80 (2008).

2. Note that in Figure 1e, for antiparallel polarization, the electromechanical coupling coefficient K_t^2 of the composite film approaches zero near v_1/v_2=0.6, while the simulated effective electromechanical coupling coefficient k_{eff}^2 of the

FBAR remains non-zero. Conversely, at v1/v2=1.0, K_t^2 increases to 6%, yet the simulated k_{eff}^2 of the FBAR is nearly zero. Please explain the relationship between k_{eff}^2 and K_t^2, and the reasons for the above contradiction.

Response to Reviewer:

We acknowledge the imprecise description regarding the abscissa in the initial manuscript and confirm that all horizontal coordinates in **Fig. 1** have been uniformly standardized to represent the AlN to total volume ratio $v_1/(v_1+v_2)$. The intrinsic electromechanical coupling coefficient K_t^2 represents the theoretical energy conversion capability of a piezoelectric material, defined as:

$$K_t^2 = \frac{e_{33}^2}{c_{33}^E \cdot \varepsilon_{33}^S + e_{33}^2}$$

where e_{33} is the piezoelectric stress coefficient, c_{33} is the elastic stiffness at a constant electric field, and ε_r is the dielectric permittivity at constant strain. It reflects the intrinsic properties of the material itself and is independent of electrode configuration, interfaces, parasitic effects, or boundary conditions. In this study, K_t^2 is derived purely from theoretical material parameters, and the effective properties for the AlN/ScAlN bilayer are obtained through homogenization. Critically, when AlN and ScAlN exhibit opposite polarities (e.g., Al-polar vs. N-polar), their e_{33} coefficients adopt opposite signs. At volume ratio $v_1/(v_1+v_2)$≈0.6, the effective e_{33} approaches zero, driving K_t^2 to a minimum. As shown in Figs. 1d and 1e, parallel polarity alignment reduces the composite film's K_t^2 from ~14% to 6% with increasing AlN fraction (with k_{eff}^2 for FBARs following a similar trend), whereas antiparallel alignment collapses both K_t^2 and k_{eff}^2 to near-zero values at $v_1/(v_1+v_2)$ ≈0.6, though K_t^2 slightly rebounds as AlN dominates beyond this point due to its intrinsic properties. These results confirm that antiparallel integration catastrophically degrades d_{33}^*, K_t^2, and k_{eff}^2, while even parallel alignment progressively diminishes performance with higher AlN content, underscoring the pivotal role of polarity control in piezoelectric bilayer design.

Revised Main Text:

Line 143:

Figure. 1d illustrates the variation of the effective longitudinal piezoelectric strain coefficient (d_{33}^*) with the AlN to total volume ratio $v_1/(v_1+v_2)$ for parallel (aligned polarity) and antiparallel (opposite polarity) configurations. In the parallel case, d_{33}^* decreases gradually with increasing AlN volume fraction due to the lower intrinsic response, yet remains positive, preserving the piezoelectric direction. Conversely, antiparallel polarity induces the mutual cancellation of piezoelectric effects, causing d_{33}^* to decline sharply and even reverse sign when $v_1/(v_1+v_2)$ exceeds around 0.7. **Figs. 1d and 1e** further show the K_t^2 of composite films and k_{eff}^2 of theoretical FBAR devices shown in **Fig. S2**. Parallel alignment reduces K_t^2 from approximately 14% to 6% (with k_{eff}^2 following similarly), indicating preserved electromechanical response. Antiparallel alignment collapses both coefficients to near-zero at $v_1/(v_1+v_2)$ of about 0.6 to 0.7, though K_t^2 slightly rebounds as AlN dominates. These results confirm that antiparallel integration severely degrades d_{33}^*, K_t^2, and k_{eff}^2, while even parallel alignment reduces performance with higher AlN content, critically compromising FBAR efficiency, underscoring polarity's pivotal role in piezoelectric properties and device design.

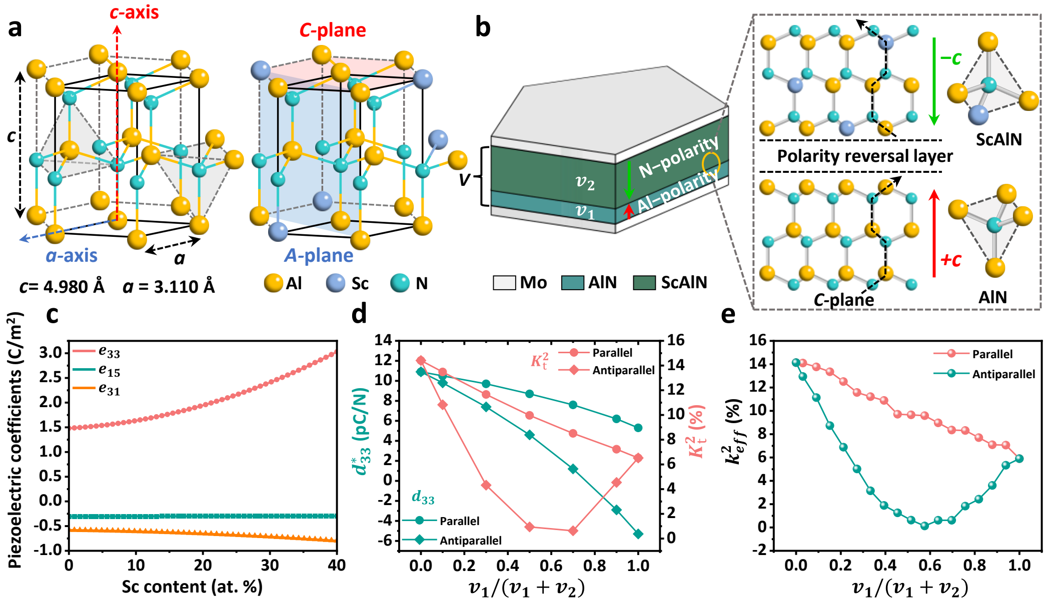

Fig. 1 Crystal structure, polarity characteristics, and piezoelectric properties of AlN and ScAlN films. b Schematic of the FBAR with the AlN/ScAlN bilayer structure, highlighting polarity orientations and the polarity reversal layer. **c** Calculated piezoelectric stress coefficients (e_{15}, e_{31}, e_{33}) as functions of Sc

concentration. **d** d_{33}^{*} and K_t^2 of AlN/ScAlN bilayers with the AlN fraction for parallel and antiparallel polarities. **e** k_{eff}^2 of the FBAR with the AlN fraction for parallel and antiparallel polarities.

3. For Figure 2i, it is recommended to include comparative data with the results reported in: "Chen, Zhipeng, et al. High-Performance Film Bulk Acoustic Resonator and Filter Based on an $Al_{0.8}Sc_{0.2}N$ Film Prepared by a Low-Temperature Staged Deposition Method. IEEE Transactions on Electron Devices 72.1, 383-389(2025) ".

Response to Reviewer:

We appreciate the reviewer's valuable suggestion and have carefully studied the work by Chen et al. (IEEE Trans. Electron Devices, 2025). This study shares a concept consistent with our work, both employ a high-quality single-crystalline AlN layer to promote the epitaxial growth of AlScN films with superior crystallinity. Specifically, Chen et al. deposited a single-crystal AlN buffer layer by pulsed laser deposition (PLD) and subsequently grew an $Al_{0.8}Sc_{0.2}N$ film by PVD. The 450-nm-thick film exhibited a (0002) X-ray rocking curve FWHM of 1.0°, compared to 1.8° for the film deposited directly on Si without a seed layer, clearly demonstrating that the use of a single-crystalline AlN seed layer significantly reduces dislocation density and enhances the orientation of ScAlN films. We have incorporated the results from this work into **Fig. 2i** to provide a more comprehensive comparison of the reported FWHM values and to better illustrate the current progress in ScAlN thin-film research.

4. On Line 293, "obtained by cutting along the slice line in Fig. 5a" should be corrected to "obtained by cutting along the slice line in Fig. 4b".

Response to Reviewer:

We thank the reviewer for pointing out this mistake. The sentence has been corrected in the revised manuscript, and all figure numbers have been carefully checked throughout the text.

Revised Main Text:

Line 308:

Fig. 4b shows the surface SEM image of the fabricated FBAR, highlighting its surface morphology, while **Fig. 4c** presents a cross-sectional SEM image taken along the slice line indicated in **Fig. 4b**, clearly revealing the multilayer structure.

5. During the fabrication of FBAR-2 and FBAR-3, when removing the AlN seed layer via ICP etching, how was over-etching into the AlScN layer prevented?

Response to Reviewer:

Response to Reviewer:

Indeed, because AlN and ScAlN exhibit very similar chemical reactivity, the removal of the AlN seed layer is a critical step for ensuring device performance. This process is implemented using inductively coupled plasma (ICP) dry etching, where distinct etching recipes were optimized for AlN and ScAlN to achieve high selectivity (**Table S5** in the newly revised **Supplementary Information**). The AlN seed layer was etched with a Cl_2-based chemistry, while the ScAlN layer employed a BCl_3-based process. To ensure precise termination, in situ optical emission spectroscopy (OES) was introduced for endpoint detection **(Fig. S10a** in the newly revised **Supplementary Information**). OES monitors the characteristic light emitted by excited plasma species and volatile reaction by-products during etching, allowing real-time tracking of process evolution. When the AlN layer is completely removed and the underlying ScAlN is exposed, the reaction chemistry changes abruptly, producing a sharp drop in emission intensity that marks the etch endpoint (**Fig. S10a**). This approach ensures complete AlN removal while preserving the structural and functional integrity of the ScAlN film. The corresponding description and data have been supplemented in the revised manuscript.

Revised Supplementary Information:

Line 335:

AlN seed layer etching

After Au-Au bonding and Si substrate removal, the AlN seed layer in the second and third FBAR sets is selectively removed via ICP dry etching to assess its impact on device performance. Given the near-identical chemical reactivity of AlN and ScAlN, uncontrolled etching risks over-etching and damaging the ScAlN layer. Distinct etching recipes are optimized for each material to enhance selectivity, as detailed in **Table S4**. The AlN seed layer is etched using a Cl_2-based chemistry, while the ScAlN layer employs a BCl_3-based process. In Cl_2 plasma, AlN exhibits a significantly higher etch rate than ScAlN due to the greater reactivity of the Al–N bond with Cl radicals and the higher volatility of $AlCl_3$ compared to $ScCl_3$. This inherent etch rate difference ensures natural selectivity, protecting the underlying ScAlN when the endpoint is reached.

Table S5 ICP etching parameters for AlN and ScAlN films.

Target layer	Etching gas	Gas flow rate	Chamber pressure	RF power
AlN	Cl_2	50 sccm	8 mTorr	500 W
ScAlN	BCl_3	100 sccm	5 mTorr	500 W

The etching process is monitored in situ by optical emission spectroscopy (OES) (**Fig. S10a**), where the emission signal associated with AlN reaction products remains stable during etching. Upon complete removal of the AlN seed layer and exposure of the underlying ScAlN, a sudden change in reaction chemistry causes a pronounced intensity drop, identified as the etch endpoint. This non-invasive, real-time detection enables precise termination, preventing over-etching and preserving device performance. Validation using an AlN/ScAlN test sample confirms endpoint accuracy, optical microscopy images before etching (**Fig. S10b**) show uniform contrast with clear pattern boundaries, while post-etching (**Fig. S10c**) reveals a distinct color shift due to ScAlN exposure, confirming complete AlN removal and a smooth, damage-free surface morphology.

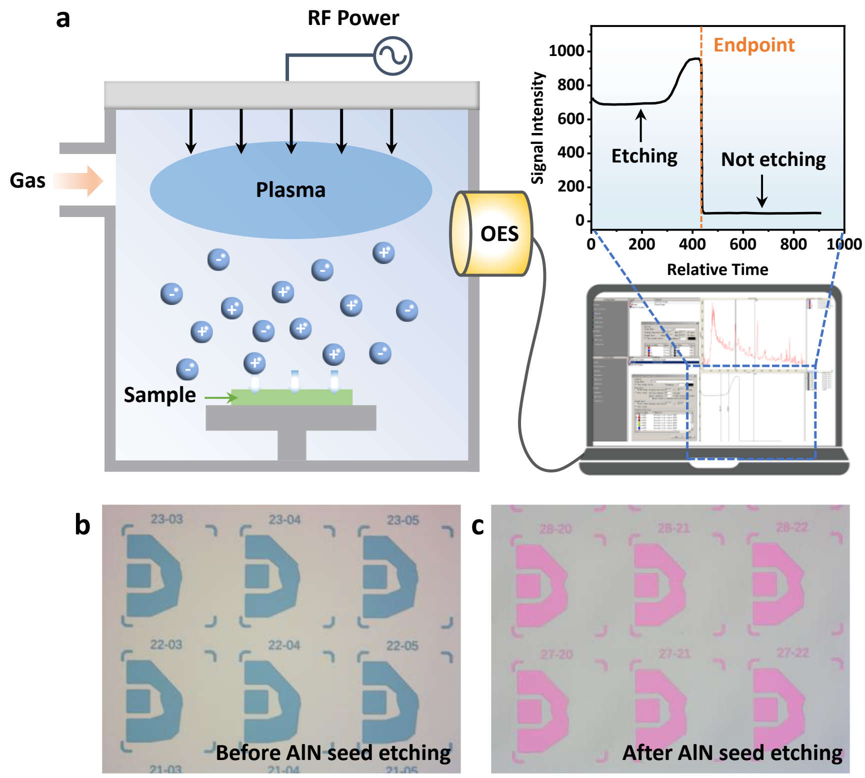

Fig. S10 The optical emission spectroscopy (OES)-based endpoint detection for AlN etching. a Schematic illustration of OES monitoring system used during the plasma etching of AlN. The RF-powered plasma generates reactive ions that bombard the sample surface, while the OES module detects the optical emission intensity of reaction products in real time. The inset shows a typical OES signal curve, where the sharp intensity drop indicates the endpoint corresponding to complete removal of the AlN seed layer. **b, c** Optical microscopy images of the MOCVD AlN seed layer before and after etching, respectively, confirming accurate endpoint control and a clean surface morphology.

6. For FBAR1 with v_1/v_2=50/280=0.18 in the final test results (in Fig. 4d), the measured k_{eff}^2 is 6%, while the FEM simulation in Figure 1e predicts $k_{eff}^2 \approx 9\%$. Please explain why the experimentally measured k_{eff}^2 is lower than the simulated value.

Response to Reviewer:

We appreciate the reviewer's comment. In this work, the finite element simulations were primarily intended to analyze the influence of the AlN/ScAlN thickness ratio on the effective electromechanical coupling coefficient (k_{eff}^2). Therefore, only the fundamental Mo-AlN/ScAlN-Mo structure was considered in the model to eliminate external factors irrelevant to this specific study. In such an ideal configuration, both the electrical and mechanical energies are confined within the piezoelectric layer, resulting in the maximum energy conversion efficiency and the theoretical k_{eff}^2.

In the fabricated devices, however, additional non-piezoelectric insulating layers such as the SiO_2 stress-relief buffer, passivation films. Although these layers play important structural and stress-management roles, they do not contribute to piezoelectric conversion and thus reduce the overall coupling efficiency.

(1) Electrical aspect: these layers form serial or parallel capacitive paths with the piezoelectric stack. Part of the applied electric field is distributed in the non-piezoelectric regions, which cannot produce piezoelectric polarization, leading to a smaller portion of the input energy effectively participating in conversion.

(2) Acoustic aspect: the acoustic impedance mismatch between the piezoelectric and surrounding layers causes partial reflection, transmission, and leakage of acoustic waves at the interfaces. This mismatch and the associated dissipation weaken the acoustic confinement in the piezoelectric film, shift the anti-resonant frequency toward lower values, and narrow the separation between the resonant and anti-resonant frequencies.

As a result, the experimentally measured k_{eff}^2 is lower than the theoretical value obtained from the idealized FEM model.

Reviewer #4 (Remarks to the Author):

Expertise: AlN films, piezo-MEMS sensors

The paper deals with the improvement of FBAR devices for sub-7 GHz applications, both by simulations and experimentally. In the focus is the impact of the quality (polycrystalline, single-crystalline) of an AlN seed layer on the properties of a ScAlN layer sputter-deposited subsequently on top. The microstructural integrity of both layers as well as the polarity change at the AlN/ScAlN interface are investigated. Their influence on FBAR device performance is measured and discussed. The paper is very timely and of high readability. However, there are some deficits in the manuscript to be addressed before final publication. These are in detail.

Response to Reviewer:

We sincerely appreciate the positive feedback from the reviewer regarding the timeliness and readability of our work. In response to the comment on deficits in the manuscript, we will carefully address these concerns by further clarifying the correlation between simulation and experimental results, particularly emphasizing how the microstructural integrity and polarity alignment at the AlN/ScAlN interface collectively influence FBAR performance. We will also provide additional details on the experimental methodology, including deposition parameters and characterization techniques, to enhance reproducibility. Furthermore, we have strengthened the discussion by including more in-depth analysis of the role of single-crystalline vs. polycrystalline seed layers in reducing defects and improving piezoelectric response, ensuring that all conclusions are well-supported by both theoretical and empirical evidence. These revisions have significantly improved the clarity and rigor of the manuscript. We hope this revised response meets the high standards of the reviewers and the journal.

a) The manuscript includes a “Discussion” section. According to the understanding of the reviewer this is a “Summary”, but does not discuss the results and findings of the authors in more detail with respect to e.g. the state of the art, as already done before.

Response to Reviewer:

We have significantly revised the Discussion section, specifically incorporating comparisons with other work to highlight the distinctions of our study and providing an in-depth analysis of the underlying reasons for these differences, which we believe makes the revised content more aligned with the journal's requirements.

Revised Main Text:

Line 416: Discussion

This investigation integrates theoretical modeling, thin-film characterization, and device-level measurements to clarify how the quality and polarity of AlN seed layers and ScAlN films affect microstructural characteristics and electromechanical performance, as well as how these elements jointly govern the ultimate operational performance of FBAR devices. Theoretical frameworks employing the Reuss and Mori-Tanaka methodologies demonstrate that the configuration of polarity is pivotal to the electromechanical response of AlN/ScAlN bilayer systems. Antiparallel polar states at the bilayer structure induce partial cancellation of internal electric fields, leading to a significant diminishment in d_{33}, K_t^2, k_{eff}^2. Our theoretical framework (Reuss and Mori-Tanaka models) quantifies how antiparallel polarity at the AlN/ScAlN bilayers catastrophically degrades electromechanical coupling (**Figs. 1d, e**), directly linking polarity mismatch to the observed K_t^2 reduction. This cancellation effect stems from opposing spontaneous polarization vectors, disrupting charge transfer efficiency across the heterointerface, a phenomenon corroborated by STEM imaging (**Fig. 3**).

Critically, the MOCVD single-crystalline AlN seed layer addresses crystallinity limitations endemic to sputtered polycrystalline seeds. Its epitaxial template suppresses AOG formation and yields ScAlN films with exceptional orientation and smoothness. This aligns with reports that low-defect acoustic scattering, explaining the higher Q in devices using single-crystalline seeds[19,54,55]. However, crystallinity alone is insufficient, polarity inversion persists at bilayer structures (**Fig. 3**), constraining k_{eff}^2. Our innovation lies in selective seed layer removal, a tactic absent in prior ScAlN FBAR studies. This physically decouples crystallinity and polarity management, the MOCVD template guides high-quality ScAlN growth but is removed before electrode deposition to eliminate the polarity-mismatched structure. The resulting k_{eff}^2 recovery to 13.2% (**Fig. 4d**) unequivocally attributes performance loss to polarity cancellation, not Sc doping or intrinsic material properties. This approach outperforms polarity-control methods relying solely on doping (e.g., SiAlN), which introduce additional defects[30].

Finally, the optimized FBARs were integrated into lattice-type filters, yielding impressive results. Relative to prior ScAlN-based filters, this work demonstrates significant advancements in bandwidth and selectivity metrics, stemming from enhanced k_{eff}^2 and Q in the constituent FBAR resonators. While this study emphasizes engineering innovations and microstructural performance analysis, future studies will incorporate deeper investigations into underlying physical mechanisms. These outcomes validate the fundamental linkage between seed layer engineering and device performance, simultaneously paving the way for high-performance RF components in advanced communication systems.

In summary, this study demonstrates a dual-optimization strategy for ScAlN-based FBARs that resolves the conflict between crystallinity and polarity alignment. While a MOCVD single-crystalline AlN seed layer is essential for achieving high-quality ScAlN films, it introduces a polarity inversion that degrades electromechanical coupling. We overcome this by removing the seed layer post-deposition, a strategy guided by theoretical and STEM analysis. This approach yields FBARs with a about 43% higher k_{eff}^2 than conventional devices. Filters incorporating these FBARs show exceptional performance with 6.4 GHz center frequency, −2.6 dB insertion loss, 740 MHz bandwidth, and >40 dB rejection, which validates our methodology. Beyond polarity engineering, this work presents a generalizable paradigm for piezoelectric heterostructures, combining epitaxial seeding, post-processing, and polarity-aligned multilayer architectures to optimize performance in sub-7 GHz applications such as filters, sensors, and energy harvesters

b) Even more, the reviewer misses a compact comparison of important FBAR device parameters, such as *Q* factor, coupling coefficient, FOM, etc. with the state of the art. The authors compare their 3 different devices among each other (see Tab. 1), what is appreciated by the reviewer, but a comparison to literature of that least their best device concept is missing, as there are a lot of similar ScAlN FBAR devices reported.

Response to Reviewer:

We have supplemented our comparative data with FBAR-0, an early-stage test structure fabricated with a retained PVD AlN seed layer, while maintaining three representative FBARs (1-3) as key comparison groups in the main text: FBAR-1 versus FBAR-3 isolates the effect of retaining versus removing the AlN seed layer, and FBAR-

2 versus FBAR-3 examines how the ScAlN film's crystalline quality (determined by the underlying seed) governs device Q factor. The configuration retaining the PVD AlN seed layer exhibited markedly inferior performance and was not pursued for filter-level characterization, with this omitted configuration now detailed in Supplementary Information per the reviewer's suggestion. Additionally, we have included a performance comparison of ScAlN-based FBARs with prior research (**Table S7**), where our ScAlN-based FBAR achieves over 6 GHz resonant frequency with Q_{max} =736 and an of 13.2%, yielding a 97 FOM. These results are competitive, particularly given the higher operating frequency and non-optimized electrode structure, leaving further improvement potential through structural optimization. The Q enhancement relative to prior ScAlN devices originates from the single-crystalline AlN seed enabling epitaxial growth of highly oriented films with minimal acoustic scattering, while subsequent seed layer removal eliminates polarity inversion at AlN/ScAlN bilayers, thereby maximizing k_{eff}^2.

Revised Main Text:

Line 348:

Detailed characterization of how different AlN seed conditions influence k_{eff}^2 and Q is shown in **Fig. S12**. Operating frequency, thin-film quality, and device architecture represent fundamental determinants of resonator Q factor, with the present work concentrating on Q enhancement via superior film crystallinity. Benchmarking against state-of-the-art results in **Table S7** confirms the competitiveness of our approach, especially notable given the elevated operating frequencies employed and the absence of electrode structure optimization specifically targeting Q improvement, which promises substantial future performance gains through structural refinements. These results collectively underscore the indispensable role of preserving high crystalline integrity in ScAlN films while strategically managing the AlN seed layer's function, delineating a viable strategy for optimizing the Q and k_{eff}^2 compromise in high-performance FBARs.

Revised Supplementary Information:

Line 391:

FBAR-0, an early-stage test structure fabricated with a retained PVD AlN seed layer, exhibits a low effective electromechanical coupling coefficient of 6.3% and a limited quality factor (Q_{max} =189) in its impedance response (**Fig. S12a**), confirming that the poor crystallinity of the PVD-deposited seed significantly degrades performance. The overall trends in **Fig. S12c** and **S12d** show that devices with MOCVD AlN seeds achieve higher Q than those with PVD seeds, while removing the seed layer further enhances the effective electromechanical coupling coefficient. Statistical comparison in **Fig. S12d**, based on over 100 samples per group, reveals that FBAR-1 operates at a higher resonance frequency than FBAR-0, and FBAR-3 at a higher frequency than FBAR-2, highlighting the substantial improvement in resonance quality attained with single-crystalline seed layers.

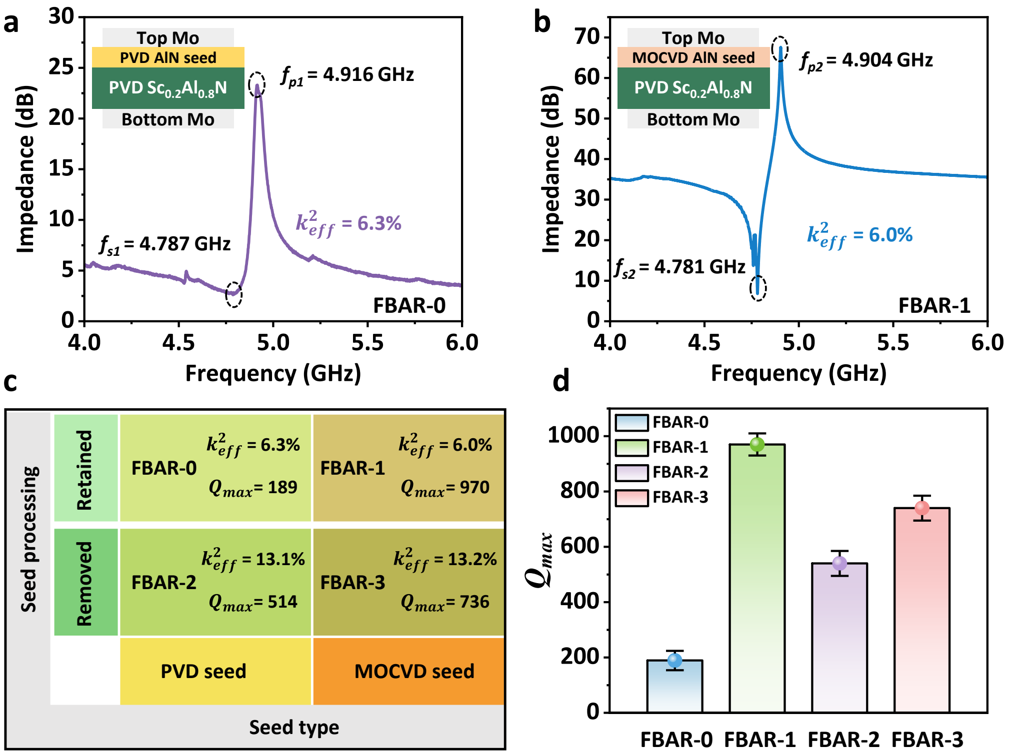

Fig. S12 Electrical characterization of FBARs with different AlN seed conditions. **a** Impedance curve of the FBAR with a retained PVD AlN seed layer, exhibiting k_{eff}^2 =6.3% and a Q_{max}=189. **b** Impedance curve of the FBAR with a retained MOCVD AlN seed layer, exhibiting k_{eff}^2 =6.0% and a maximum quality factor Q_{max}=970. **c** Summary of k_{eff}^2 and Q_{max} in FBARs fabricated with different AlN seed types (PVD or MOCVD) and processing conditions (retained or removed). Devices using MOCVD AlN seeds exhibit consistently higher Q_{max} values than those based on PVD seeds, while removing the AlN seed layer significantly enhances k_{eff}^2 in both cases. **d** Statistical analysis of Q factors for the four FBAR groups.

As summarized in **Table S7**, the $Sc_{0.2}Al_{0.8}N$-based FBAR achieves a resonant frequency of 6.8 GHz with a Q_{max} of 736 and an k_{eff}^2 of 13.2%, yielding a FOM of 97. Operating frequency, film quality, and device structure are key factors influencing the resonator's Q, and this study focuses on enhancing Q through improved film quality. The obtained results are competitive compared with references, especially considering the higher operating frequency and the fact that the electrode structure has not been fully optimized for Q enhancement, leaving further room for performance improvement via structural optimization in the future. The Q factor enhancement relative to prior ScAlN devices stems from the single-crystalline AlN seed layer, which enables epitaxial growth of highly oriented ScAlN films with minimal acoustic scattering. Subsequent selective removal of this seed layer eliminates polarity inversion at the AlN/ScAlN bilayers, thereby maximizing k_{eff}^2.

Table S7 Comparison of the performance of ScAlN-based FBARs with others research.

	Materials	Frequency (GHz)	Q_{max}	k_{eff}^2	FOM
Ref [15]	AlN	3.3	837	7.2%	60
Ref [16]	AlN	5.2	1497	6.07%	91
Ref [17]	AlN	5.93	2500	5.48%	137
Ref [5]	$Sc_{0.2}Al_{0.8}N$	4.3	424	14.5%	62
Ref [18]	$Sc_{0.2}Al_{0.8}N$	4.63	1310	10.7%	140
Ref [19]	$Sc_{0.096}Al_{0.904}N$	4.72	673	11.7%	78.7
This Work	$Sc_{0.2}Al_{0.8}N$	6.8	736	13.2%	97

c) How do the simulated piezoelectric constants match with experimental and/or theoretically predicted data reported in literature (see Fig. 1c)? The authors need to benchmark their results.

Response to Reviewer:

In this work, the piezoelectric stress coefficients of wurtzite $Sc_xAl_{1-x}N$ ($0 \le x \le 0.4$) were calculated using density functional perturbation theory (DFPT), showing good agreement with both theoretical predictions and experimental reports in previous studies[1-6]. As shown in **Fig. R15**, the simulated e_{33} increases monotonically with Sc concentration, consistent with the trends reported in previous DFT and experimental studies[1-4]. This enhancement reflects the intrinsic lattice softening and polarization amplification induced by Sc incorporation. Furthermore, **Table S2** in the revised Supplementary Information provides a quantitative comparison of the key piezoelectric stress coefficients (e_{33}, e_{31}, and e_{15}) for AlN and $Sc_{0.2}Al_{0.8}N$ with representative literature data. The results obtained in this work (e_{33}=1.492 C/m^2 for AlN; e_{33}=1.944 C/m^2 for $Sc_{0.2}Al_{0.8}N$) are in excellent agreement with previously reported DFT values (1.44-1.47 C/m^2 for AlN, 1.84-1.94 C/m^2 for $Sc_{0.2}Al_{0.8}N$) and with the experimental range for AlN (1.39-1.55 C/m^2). Both the magnitude and the composition-dependent trend validate the reliability of our DFPT-based calculations. The revised manuscript includes a description of the method for calculating the piezoelectric coefficient and a comparison of the results.

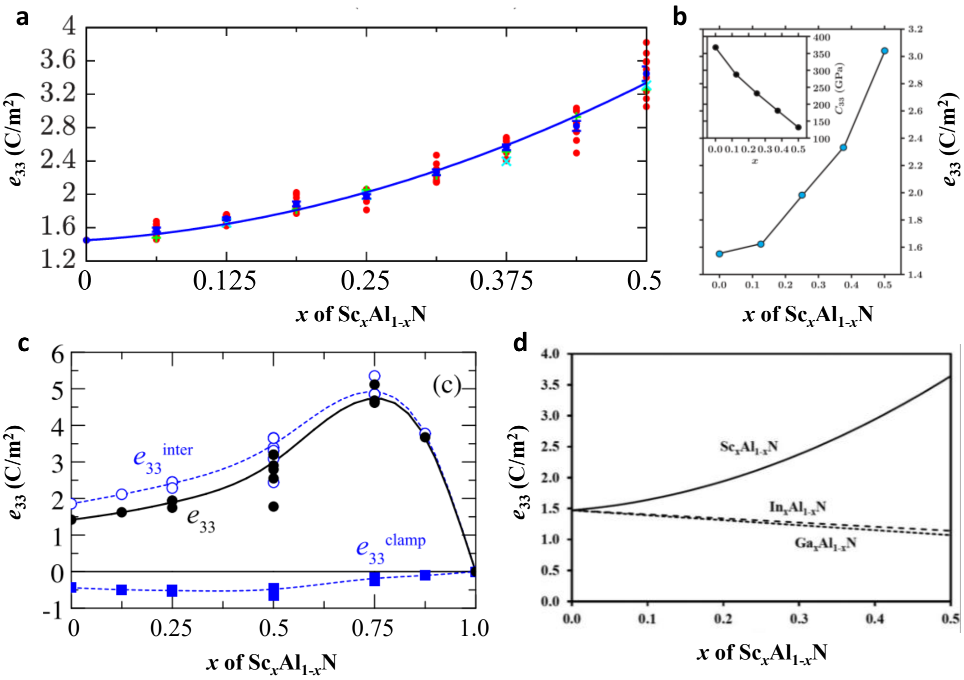

Fig. R15 The trends of the piezoelectric coefficient e_{33} in wurtzite $Sc_xAl_{1-x}N$ reported in previous studies[1-4].

Revised Supplementary Information:

Line 20:

First-principles calculation of piezoelectric stress coefficients

Figure S1 shows the wurtzite $Sc_xAl_{1-x}N$ supercell models used for first-principles calculations, where 2×2×2 wurtzite supercells are constructed to model Sc substitution at Al sites with Sc concentrations of 6.25 at.%, 12.5 at.%, 18.75 at.%, 25 at.%, 31.25 at.%, and 37.5 at.%, respectively. The computational settings align with the **Method**

section of the main text. The compositional dependence of material properties on Sc concentration, illustrated in **Fig. 1c**, is derived by fitting discrete data points with a quadratic polynomial, as shown in **Table 1**. The calculated material parameters for AlN and $Sc_{0.2}Al_{0.8}N$ show excellent consistency with established literature values (**Table S2**). These parameters are subsequently adopted for FBAR and filter modeling. Experimentally extracted parameters, obtained by fitting measured impedance spectra using the Mason model after device fabrication, exhibit close agreement with simulation inputs and literature data, demonstrating the methodology's accuracy and self-consistency.

Table S1 Calculated piezoelectric stress coefficients of wurtzite $Sc_xAl_{1-x}N$ at different Sc contents.

	AlN	6.25 at.%	12.5 at.%	18.75 at.%	25 at.%	31.25 at.%	37.5 at.%
e_{33} (C/m^2)	1.492	1.543	1.698	1.901	2.152	2.486	2.866
e_{31} (C/m^2)	−0.578	−0.592	−0.621	−0.644	−0.670	−0.724	−0.775
e_{15} (C/m^2)	−0.304	−0.303	−0.301	−0.299	−0.299	−0.298	−0.297

The compositional dependence of e_{ij} on Sc concentration is obtained by fitting the discrete data points with a quadratic polynomial:

$$e_{15}(x) = -0.2984x - 0.3043(1-x) + 0.0245x(1-x) \quad (8)$$

$$e_{31}(x) = -1.6800x - 0.5781(1-x) + 0.9281x(1-x) \quad (9)$$

$$e_{33}(x) = 10.0304x + 1.4815(1-x) - 7.7945x(1-x) \quad (10)$$

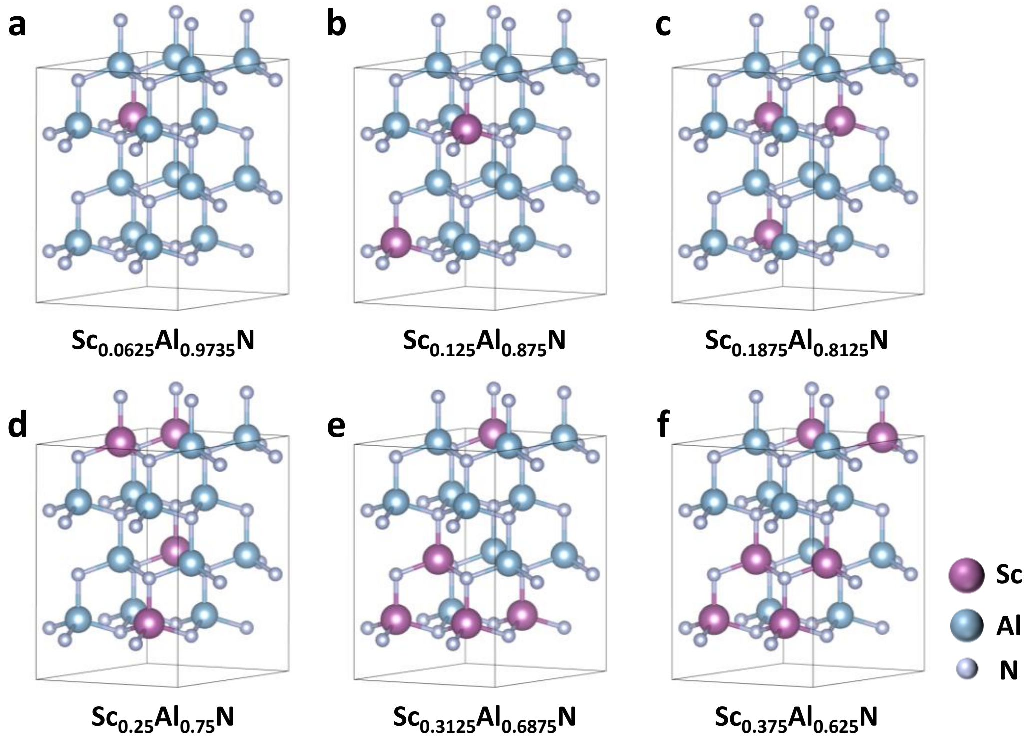

Fig. S1 Wurtzite $Sc_xAl_{1-x}N$ supercell models used for first-principles calculations. **a-f** 2×2×2 wurtzite supercells are constructed to model Sc substitution at Al sites with Sc concentrations of 6.25 at.%, 12.5 at.%, 18.75 at.%, 25 at.%, 31.25 at.%, and 37.5 at.%, respectively.

Table S2 Comparison of calculated and experimental material parameters with literature values for AlN and $Sc_{0.2}Al_{0.8}N$.

Material parameters		Calculation		Experiment	
		This work	Ref.	This work	Ref.
AlN	e_{33} (C/m^2)	1.492	1.471 [a]	1.52	1.55 [c]
	e_{31} (C/m^2)	−0.578	−0.593 [a]	/	−0.58 [c]
	e_{15} (C/m^2)	−0.304	−0.313 [a]	/	−0.48 [c]
	ε_r	9.3	10.31[b]	9.5	9.5 [d]
$Sc_{0.2}Al_{0.8}N$	e_{33} (C/m^2)	1.944	1.942 [a]	2.09	2.08 [e]
	e_{31} (C/m^2)	−0.649	−0.653 [a]	/	/
	e_{15} (C/m^2)	−0.299	−0.273 [a]	/	/
	ε_r	13.33	16.23[b]	13.56	13.42 [e]

[a] See Ref.[1], [b] See Ref.[2], [c] See Ref.[3], [d] See Ref.[4], [e] See Ref.[5]

References

1. Caro, M. A., Zhang, S., Riekkinen, T., Ylilammi, M., Moram, M. A., López-Acevedo, O. & Laurila, T. Piezoelectric coefficients and spontaneous polarization of ScAlN. *J. Phys.: Condens. Matter.* 27, 245901 (2015).
2. Tasnádi, F., Alling, B., Höglund, C., Wingqvist, G., Birch, J., Hultman, L. & Abrikosov, I. A. Origin of the anomalous piezoelectric response in wurtzite $Sc_xAl_{1-x}N$ alloys. *Phys. Rev. Lett.* 104, 137601 (2010).
3. Momida, H., Teshigahara, A. & Oguchi, T. Strong enhancement of piezoelectric constants in $Sc_xAl_{1-x}N$: first-principles calculations. *AIP Adv.* 6, 065006 (2016).
4. Ambacher, O., Christian, B., Feil, N., Urban, D. F., Elsässer, C., Prescher, M. & Kirste, L. Wurtzite ScAlN, InAlN, and GaAlN crystals: a comparison of structural, elastic, dielectric, and piezoelectric properties. *J. Appl. Phys.* 130, 045102 (2021).
5. Tsubouchi, K. & Mikoshiba, N. Zero-Temperature-Coefficient SAW Devices on AlN Epitaxial Films. *IEEE Trans. Sonics Ultrason.* 32, 634–644 (1985).
6. Bu, G., Ciplys, D., Shur, M., Schowalter, L. J., Schujman, S. & Gaska, R. Electromechanical coupling coefficient for surface acoustic waves in single-crystal bulk aluminum nitride. *Appl. Phys. Lett.* 84, 4611 (2004).

d) The reviewer misses a clear need to include the simulations in the manuscript. Where in this study did the authors quantitatively compare the simulation results with those from device or material analyses? The reviewer could not find such a direct comparison, raising the question why these simulations help to understand the experimental results in more detail.

Response to Reviewer:

In the revised manuscript, detailed comparative analyses between the simulation and experimental results for the materials, FBAR devices, and corresponding filters have been added to clearly demonstrate the quantitative consistency and relevance of the simulations.

Specifically, as discussed in **Comment (c)**, the initial material parameters were obtained from first-principles calculations and subsequently used for FBAR modeling (the corresponding results have been added in the **revised Fig. 4c**). The simulated material constants were then verified by comparing with the experimentally fitted parameters extracted from the measured impedance spectra of the fabricated FBARs, confirming the accuracy and validity of the computational results.

The filter design and fabrication were established through iterative optimization from Filter-1 to Filter-3. Filters 1 and 2 were used for process verification and calibration. Due to incomplete consideration of process-induced variations in the initial simulation, slight frequency mismatches occurred between the series and parallel resonators in Filter-1 and Filter-2. Based on the FBAR-extracted material parameters and the measured layer thicknesses, the simulated responses of Filter-1 and Filter-2 were recalibrated to reproduce the experimental data (see r**evised Figs. 5d and 5e**). Using these calibrated parameters, Filter-3 was redesigned, achieving an insertion loss of −2.6 dB, a 740 MHz bandwidth, and > 40 dB rejection (**Fig. 5f**), in excellent agreement with the optimized simulation results.

Revised Main Text:

Line 311:

Figure 4d displays the simulated (dash lines) and measured (solid lines) frequency responses of the three FBARs, where the blue curve represents FBAR-1 (single-crystalline AlN seed layer, retained), the green curve corresponds to FBAR-2 (polycrystalline AlN seed layer, removed), and the red curve is associated with FBAR-3 (single-crystalline AlN seed layer, removed). … FBAR-1 demonstrates a comparatively low k_{eff}^2 of 6.0%, while FBAR-2 and FBAR-3 exhibit substantially improved k_{eff}^2 of 13.1% and 13.2%, respectively. This enhancement stems from the elimination of polarity inversion at the AlN/ScAlN bilayers. In FBAR-1, the opposing polarities between the AlN seed layer and the $Sc_{0.2}Al_{0.8}N$ film cause partial cancellation of the electric field, thereby diminishing electromechanical coupling efficiency. Conversely, removing the AlN seed layer in FBAR-2 and FBAR-3 effectively alleviates the detrimental effects of polarity mismatch. These results agree well with theoretical and simulated expectations, verifying that eliminating the polarity-mismatched AlN seed layer successfully restores the intrinsic piezoelectric response of the $Sc_{0.2}Al_{0.8}N$ film.

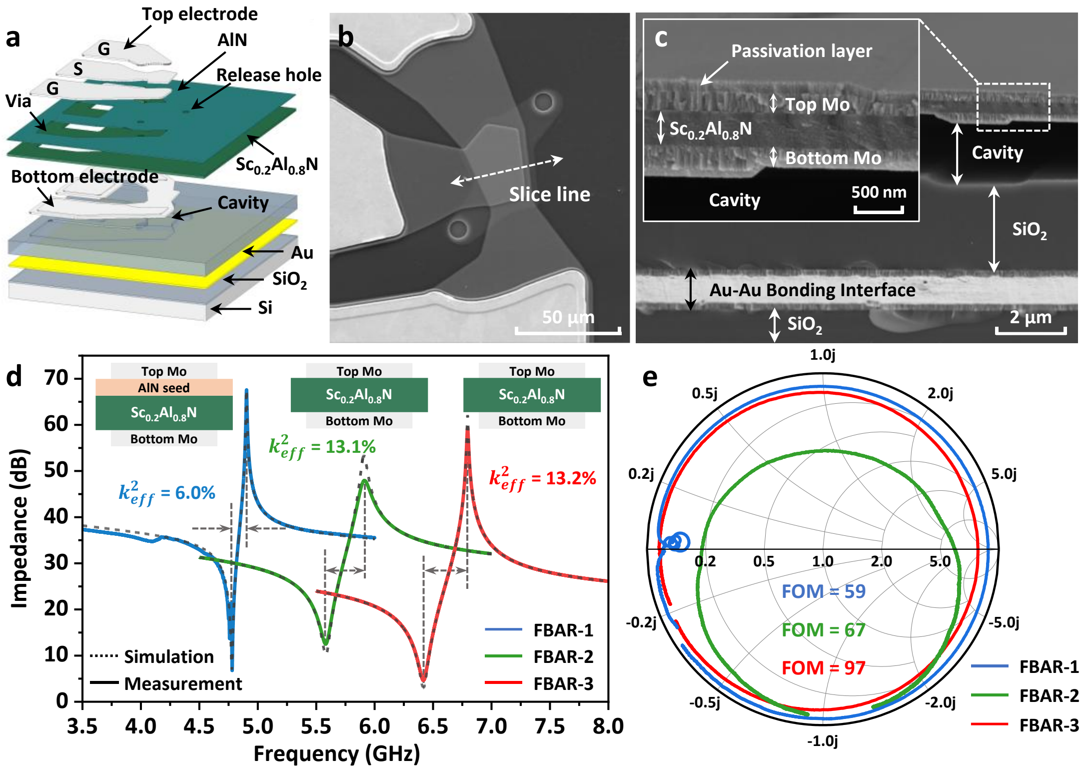

Fig. 4 Measurement and analysis of the fabricated FBARs. d The simulated (dash lines) and measured (solid lines) frequency responses of the three FBARs with different seed layer configurations.

Line 386:

…The limited bandwidths of Filter-1 and Filter-2 arise from frequency mismatch between the series and parallel resonators. Based on the FBAR-extracted material parameters and the measured stack thicknesses, the simulated responses of Filter-1 and Filter-2 are recalibrated to reproduce the experimental results. Using these calibrated parameters, as shown in **Fig. 5f,** Filter-3 is redesigned and achieves an insertion loss of −2.6 dB, a 740 MHz bandwidth, and >40 dB rejection (**Fig. 5f**), in good agreement with the optimized simulation.…

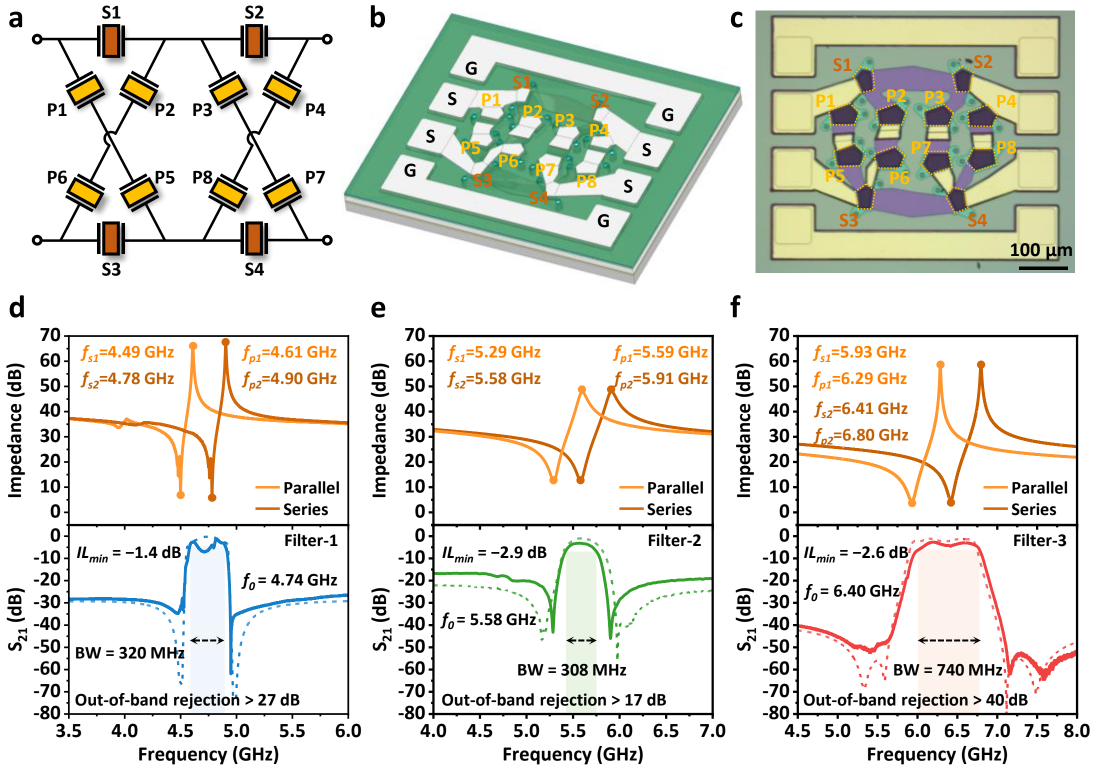

Fig. 5 Experimental results of the fabricated filters. d-f The simulated (dash lines) and measured (solid lines) transmission responses of the filters, along with the impedance curves of the corresponding resonators, for (**d**) Filter-1 (single-crystalline AlN seed layer, retained), (**e**) Filter-2 (polycrystalline AlN seed layer, removed), and (**f**) Filter-3 (single-crystalline AlN seed layer, removed).

e) The reviewer misses a statement in the manuscript whether and if yes, how the authors included the different permittivity values of AlN and ScAlN films in their simulations.

Response to Reviewer:

In response to the reviewer's comments, the revised Supplementary Information (**Table S2**, listed in **Comment (3)**) now compares calculated and experimental permittivity values of AlN and ScAlN films with prior research, where the DFT-calculated values (see Supplementary Information for methodology) and experimental data obtained through resonator reverse fitting show good agreement. The experimental permittivity ε_r was determined from the resonator's capacitance relationship[1]:

$$C_0 = \frac{\varepsilon_r \varepsilon_0 A}{d}$$

where A is electrode area and d is piezoelectric layer thickness. The close alignment between simulated and experimental resonator responses in **Fig. 4d** validates the accuracy of our fitted parameters, which are also consistent with existing literature references[1-3].

Reference

1. Zou, Y. *et al.* Aluminum scandium nitride thin-film bulk acoustic resonators for 5G wideband applications. *Microsystems Nanoeng.* **8**, (2022).
2. Ambacher, O. *et al.* Wurtzite ScAlN, InAlN, and GaAlN crystals, a comparison of structural, elastic, dielectric, and piezoelectric properties. *J. Appl. Phys.* **130**, (2021).
3. Zou, J. & Pisano, A. P. Temperature compensation of the AlN Lamb wave resonators utilizing the S1 mode. in *2015 IEEE International Ultrasonics Symposium, IUS 2015* 1–4 (IEEE, 2015). doi:10.1109/ULTSYM.2015.0456.

f) How accurate is the *Q*-factor determined from their measurements? The authors state an "43.2% increase". The reviewer doubts that this is possible with such accuracy. A rigorous error analysis including error propagation is needed for each *Q*-factor value.

Response to Reviewer:

We thank the reviewer for this important comment and have supplemented the revised manuscript accordingly. This work employed the Bode Q method, expressed as[1]:

$$Q = \omega \cdot \frac{|S_{11}|\, group\_delay\left(S_{11}\right)}{1 - |S_{11}|^2}$$

where ω is angular frequency and *group_delay* (S_{11}) is derived from the frequency derivative of the S_{11} phase. This method aligns with Q fundamental definition as the ratio of stored energy to dissipated power per cycle by evaluating the phase response slope and power transmission, providing a robust measure of energy dynamics that inherently accounts for both intrinsic losses and external loading effects. Compared to the 3 dB bandwidth method, the Bode approach offers superior immunity to measurement noise and frequency resolution limitations, particularly advantageous for high-Q resonators and facilitates automated, high-throughput characterization of thousands of devices as performed herein. Regarding the reported enhancement, the 43.2% increase was calculated from representative devices (Q = 514 vs. 736), values closely matching wafer-level averages from over 100 samples per group. While this representative selection avoids bias from outliers, we acknowledge that "43.2%" implies excessive precision. The revised manuscript conservatively states "about 43%". Additionally, we have incorporated statistical validation in **Fig. S12d** confirm devices using MOCVD AlN seeds exhibit consistently higher Q_{max} values than those based on PVD seeds.

Revised Supplementary Information:

Statistical comparison in **Fig. S12d**, based on over 100 samples per group, reveals that FBAR-1 operates at a higher resonance frequency than FBAR-0, and FBAR-3 at a higher frequency than FBAR-2, highlighting the substantial improvement in resonance quality attained with single-crystalline seed layers.

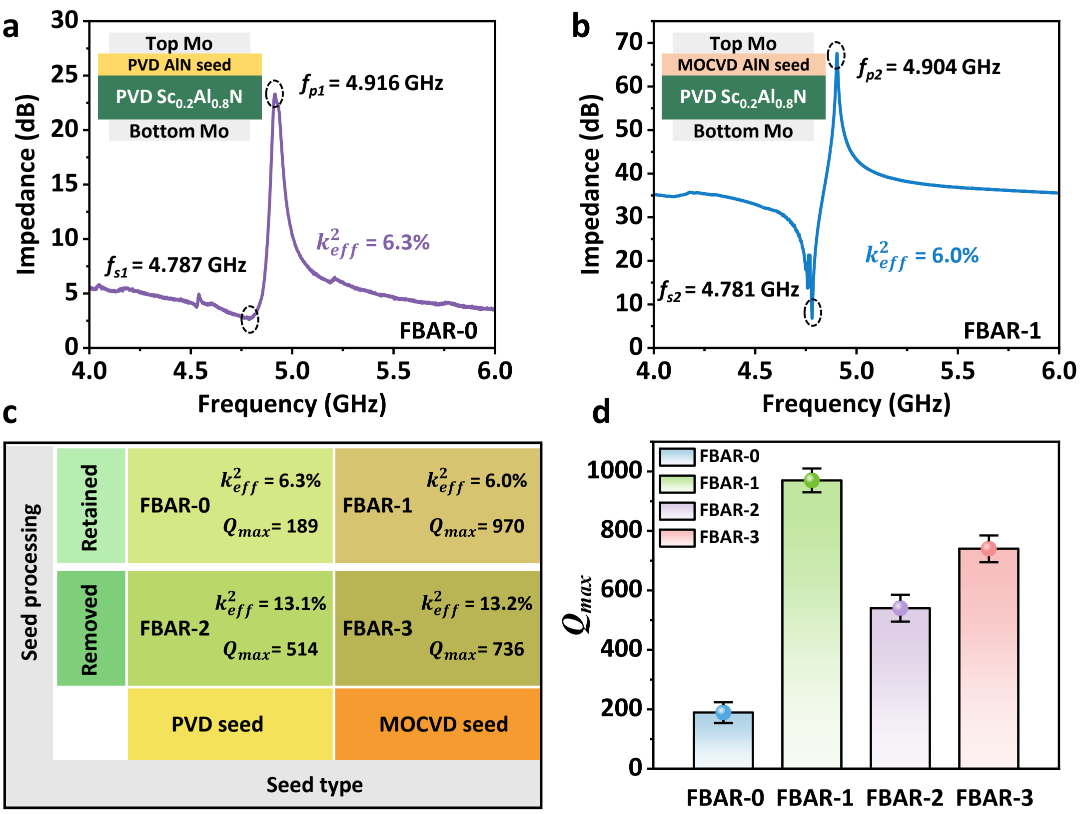

Fig. S12 Electrical characterization of FBARs with different AlN seed conditions. **a** Impedance curve of the FBAR with a retained PVD AlN seed layer, exhibiting k^2_{eff} =6.3% and a Q_{max}=189. **b** Impedance curve of the FBAR with a retained MOCVD AlN seed layer, exhibiting k^2_{eff} =6.0% and a maximum quality factor Q_{max}=970. **c** Summary of k^2_{eff} and Q_{max} in FBARs fabricated with different AlN seed types (PVD or MOCVD) and processing conditions (retained or removed). Devices using MOCVD AlN seeds exhibit consistently higher Q_{max} values than those based on PVD seeds, while removing the AlN seed layer significantly enhances k_{eff}^2 in both cases. **d** Statistical analysis of Q factors for the four FBAR groups.

References

1. Feld, D. A., Parker, R., Ruby, R., Bradley, P. & Dong, S. After 60 years: A new formula for computing quality factor is warranted. in *2008 IEEE Ultrasonics Symposium (IUS)* 431–436 (2008). doi:10.1109/ULTSYM.2008.0105.

g) How many devices did the authors measure to get to their *Q*-factors? A corresponding statement is needed.

Response to Reviewer:

We have supplemented the revised manuscript with the corresponding data. Wafers were fabricated for each FBAR configuration, and statistical comparisons based on more than 100 samples per group (**Fig. S12d**, listed in **Comment (f)**) show that FBAR-1 exhibits higher Q values than FBAR-0, and FBAR-3 higher than FBAR-2, highlighting the substantial improvements in resonance quality achieved by employing single-crystalline AlN seed layers. Due to inevitable process variations, the Q factors exhibit a statistical distribution across each wafer, with the maximum values fluctuating within ±50 of their averages (**Fig. S12d**). To ensure representative comparison, devices whose Q factors were closest to the statistical averages were selected from each wafer for the main text, ensuring that the reported impedance and transmission curves accurately reflect the overall device performance while maintaining clarity of presentation.

h) Why a Mo metallization is used when Mo is not needed as seed layer for the AlN layer, as done typically in literature? Is the Mo layer optimized in e.g. microstructure, texture, thickness, etc.? Even more, what is the stress state of the material and how does it affect the device performance?

Response to Reviewer:

(1) The advantages of Mo as electrode

As summarized in **Table. R1**, Mo exhibits a unique balance of electrical, acoustic, and thermo-mechanical properties compared with other commonly used electrode metals. Al, despite its low resistivity (2.8 μΩ·cm), has a very low acoustic impedance (1.37×10^7 kg/m^2·s) and a high coefficient of thermal expansion (22.9 ppm/°C). Pt and

Ti, while chemically stable, suffer from either higher resistivity (10.7 μΩ·cm for Pt, 55 μΩ·cm for Ti) or large density/thermal mismatch, leading to degraded device performance. W shows high acoustic impedance (8.88×10^7 kg/m^2·s), which provides strong reflection but at the cost of very high density and stress issues in thin films. By contrast, Mo combines relatively low resistivity (5.7 μΩ·cm), moderate density (10200 kg/m^3), acoustic impedance (5.48×10^7 kg/m^2·s) well matched to AlN/ScAlN, and a low coefficient of thermal expansion (5.1 ppm/°C). This balance minimizes electrical loss, ensures efficient acoustic confinement, and reduces thermal mismatch stress during high-temperature processing. For these reasons, Mo has become a commonly used electrode material in FBAR and was therefore adopted in our study.

Table. R1 Comparison of typical electrode materials used in FBARs.

Electrode Material	Resistivity (μΩ·cm)	Density (kg/m^3)	Acoustic impedance (kg/m^2·s)	Coefficient of Thermal Expansion (ppm/°C)
Al	2.8	2700	1.37×10^7	22.9
Pt	10.7	2150	6.01×10^7	8.9
Ti	55	21500	2.28×10^7	8.9
W	5.3	19200	8.88×10^7	4.3
Mo	5.7	10200	5.48×10^7	5.1

(2) The limitations of Mo as seed layer

The molybdenum (Mo) electrode is well-suited as an electrode layer for resonators, but it is not suitable for use as a seed layer for the growth of AlN or ScAlN. The specific analysis is as follows.

a) Lattice mismatch

High-quality *c*-axis oriented AlN requires an underlying surface with symmetry compatible with its hexagonal wurtzite structure. The Mo (110) surface, which is the preferred orientation for electrodes commonly used in FBAR devices, exhibits rectangular symmetry that is incompatible with the hexagonal symmetry of AlN, shown in **Fig. R16b**. As a result, AlN deposited on Mo usually shows columnar, polycrystalline growth accompanied by increased surface roughness. By contrast, substrates such as Si (111) provide a triangular lattice projection that matches the hexagonal symmetry of AlN, thereby enabling high-quality epitaxy, as shown in **Fig. R16a**.

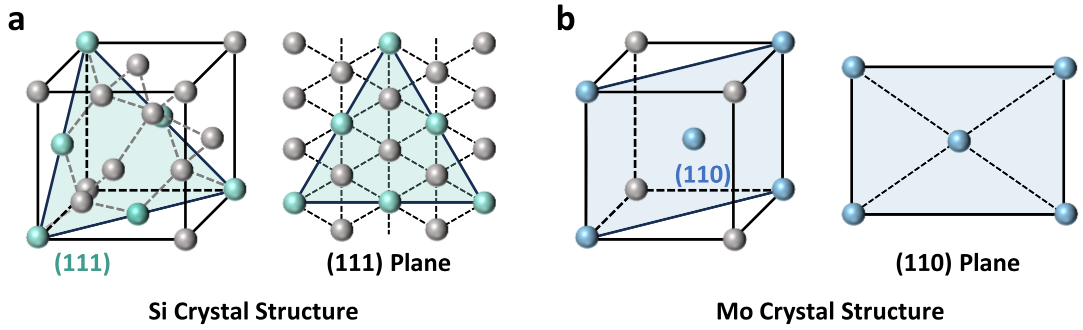

Fig. R16 Crystal structures of Si (111) and Mo (110) planes. a Si has a diamond-cubic structure, and the (111) plane exhibits an equilateral triangular lattice. **b** Mo has a body-centered cubic (bcc) structure, and the (110) plane exhibits a rectangular lattice.

b) Process compatibility

Typical MOCVD AlN growth conditions (1000-1400 °C, NH_3/H_2 ambient) are highly unfavorable for Mo stability. Mo readily nitrides to form Mo_2N/MoN, accompanied by volumetric expansion, embrittlement, and particle generation. These particles not only compromise the film crystallinity but also risk contaminating the reactor chamber. For this reason, Mo is more commonly employed as an electrode in device fabrication, rather than as a direct template for MOCVD AlN epitaxy.

Even so, during the initial stage of thin-film development we systematically examined the influence of Mo and AlN seed layers on the crystalline quality of ScAlN. As shown in **Fig. R17**, four samples were fabricated for comparison. In Sample 1 (**Fig. R17a**), a 60 nm-thick Mo electrode was sputtered on Si, followed by 280 nm-thick ScAlN. In Sample 2 (**Fig. R17b**), a 50 nm-thick PVD AlN seed layer and a 60 nm-thick Mo electrode were sputtered sequentially on Si, followed by 280 nm-thick ScAlN. In Sample 3 (**Fig. R17c**), a 50 nm-thick MOCVD AlN seed layer was epitaxially grown on Si, on top of which a 60 nm-thick Mo electrode and 280 nm-thick ScAlN were deposited. In Sample 4 (**Fig. R17d**), a 50 nm-thick MOCVD AlN seed layer was epitaxially grown on Si, followed directly by 280 nm ScAlN without Mo.

The X-ray rocking-curve FWHM values were 2.6°, 2.3°, 1.4°, and 0.94°, respectively, clearly showing the superiority of MOCVD AlN as a seed layer and the further improvement when ScAlN is deposited directly on MOCVD AlN/Si without an intermediate Mo layer. Taken together, these comparisons establish that Mo cannot act as a suitable seed layer for AlN or ScAlN, and that the epitaxial AlN/ScAlN stack offers the optimal crystalline quality.

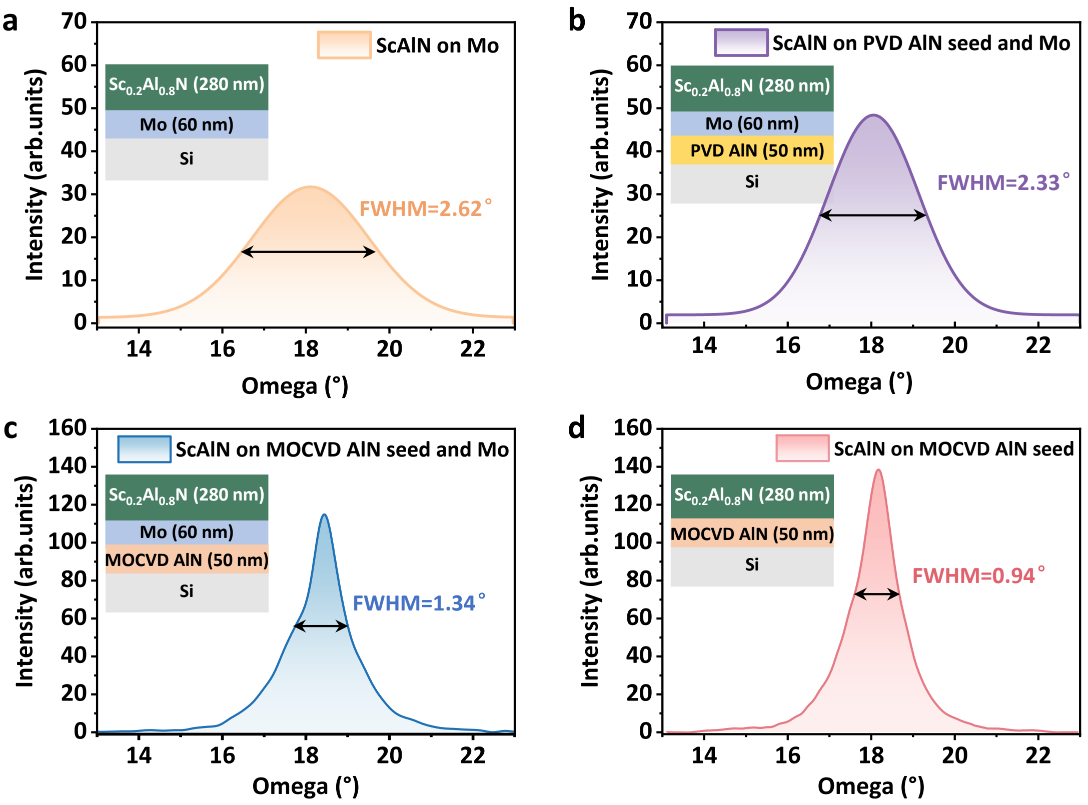

Fig. R17 (Fig. S6 in the newly revised Supplementary Information) X-ray rocking curve of the 280 nm-thick $Sc_{0.2}Al_{0.8}N$ film. a 280 nm-thick $Sc_{0.2}Al_{0.8}N$ deposited on a 60 nm-thick Mo layer on Si, FWHM = 2.62°. **b** 280 nm-thick $Sc_{0.2}Al_{0.8}N$ deposited on 60 nm-thick Mo with a 50 nm-thick PVD AlN seed layer on Si, FWHM = 2.33°. **c** 280 nm-thick $Sc_{0.2}Al_{0.8}N$ deposited on 60 nm-thick Mo with a 50 nm-thick MOCVD AlN seed layer on Si, FWHM = 1.34°. **d** 280 nm-thick $Sc_{0.2}Al_{0.8}N$ deposited directly on a 50 nm-thick MOCVD AlN seed layer on Si without Mo, FWHM = 0.94°.

(3) The characterization of Mo electrode

The Mo electrode in the work was deposited with optimized thickness and sputtering conditions to achieve a balance between conductivity, crystallinity, and stress. Wafer bow mapping shows a uniform curvature with an average residual stress of 76 MPa (**Fig. R18a**), well within the acceptable range and without inducing wafer warpage or cracking. Atomic force microscopy (10×10 μm^2) confirms a smooth surface with RMS roughness of 0.90 nm, as shown in **Fig. R18b**. X-ray diffraction pattern shown in **Fig. R18c** reveals that Mo is predominantly oriented along the (110) direction. The X-ray rocking curve measurement in **Fig. R18d** further yields a FWHM of 1.71°, indicating good crystalline quality. The residual stress of the Mo film is sufficiently low that it does not degrade structural integrity or acoustic performance. The primary effect of Mo on the device is a finite resistive loss, which slightly reduces Q_s. And this effect can be reduced by controlling the film thickness and structure.

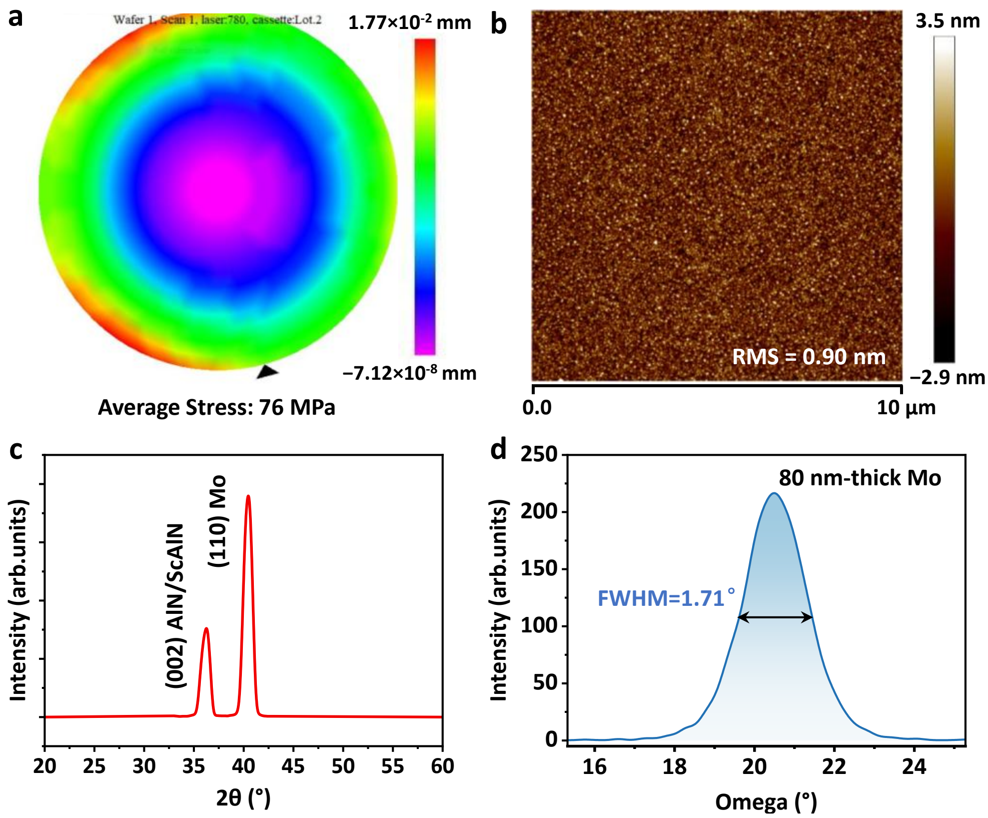

Fig. R18 Structural characterization of the sputtered Mo electrode. **a** Wafer bow mapping showing an average residual stress of 76 MPa. **b** AFM image (10×10 μm^2) revealing a smooth surface with an RMS roughness of 0.90 nm. **c** X-ray diffraction pattern indicating that Mo is predominantly oriented along the (110) direction. **d** X-ray rocking-curve scan of the Mo (110) reflection with a FWHM of 1.71°.

(4) The stress state of the material to the device performance

Residual stress in piezoelectric thin films is known to modify their lattice parameters and thereby influence both the intrinsic electromechanical coupling coefficient (K_t^2) and the effective coupling coefficient (k_{eff}^2) of resonators. Previous studies have demonstrated that tensile stress tends to enhance the piezoelectric constant e_{33} and increase K_t^2, whereas compressive stress leads to lattice expansion along the *c*-axis and a reduction in k_{eff}^2. For example, Gu et al. (Composite Structures, 2024, 340: 118203) revealed that the K_t^2 of AlN-based BAW resonators increases linearly with tensile stress up to ~200 MPa and decreases under compression. Similar conclusions were reported by Iborra et al. (Sens. Actuators A, 2004, 115, 501-507) and Tabaru et al. (Thin Solid Films, 2019, 692, 137625), showing that excessive residual stress (> 300

MPa) causes frequency drift and deteriorates filter bandwidth.

In this work, both the $Sc_{0.2}Al_{0.8}N$ piezoelectric layer and the Mo electrode exhibit residual stresses below 200 MPa. According to the aforementioned reports, such moderate stress produces negligible variation in lattice constants and exerts a minimal influence on K_t^2 and k_{eff}^2. Therefore, the observed device performance can be attributed primarily to the material quality rather than stress-induced effects.

i) ICP back etching of the AlN seed layer: is the ScAlN layer damaged surface-near by the dry etching process? Does that change the stress state of the thin film, does it impact the device performance by other material parameters?

Response to Reviewer:

Indeed, because AlN and ScAlN exhibit very similar chemical reactivity, the removal of the AlN seed layer is a critical step for ensuring device performance. This process is implemented using inductively coupled plasma (ICP) dry etching, where distinct etching recipes were optimized for AlN and ScAlN to achieve high selectivity (**Table S5** in the newly revised **Supplementary Information**). The AlN seed layer was etched with a Cl_2-based chemistry, while the ScAlN layer employed a BCl_3-based process. To ensure precise termination, in situ optical emission spectroscopy (OES) was introduced for endpoint detection **(Fig. S10a** in the newly revised **Supplementary Information**). OES monitors the characteristic light emitted by excited plasma species and volatile reaction by-products during etching, allowing real-time tracking of process evolution. When the AlN layer is completely removed and the underlying ScAlN is exposed, the reaction chemistry changes abruptly, producing a sharp drop in emission intensity that marks the etch endpoint (**Fig. S10a**). This approach ensures complete AlN removal while preserving the structural and functional integrity of the ScAlN film. The corresponding description and data have been supplemented in the revised manuscript.

Moreover, the residual stress distributions of $Sc_{0.2}Al_{0.8}N$ films on different AlN seed layers (PVD and MOCVD) in **Figs. S5 f-g** exhibit compressive stress profiles with good wafer-scale uniformity, averaging −133 MPa for PVD-seed films and −138 MPa for MOCVD-seed films. While seed layers possess distinct stress characteristics, the ScAlN maintains consistently low and uniform stress, a prerequisite for structural integrity during subsequent seed layer removal. This characteristic allows smooth post-etch surfaces and preserves the integrity of the remaining pure ScAlN film, as the minimal intrinsic stress during film growth ensures the etching process itself has negligible impact on device performance, provided the etching is properly implemented without significant surface damage. To improve clarity for readers, we have added a more detailed description of the AlN etching process in the revised manuscript and expanded the discussion of the device performance results accordingly.

Revised Supplementary Information:

Line 335:

AlN seed layer etching

After Au-Au bonding and Si substrate removal, the AlN seed layer in the second and third FBAR sets is selectively removed via ICP dry etching to assess its impact on device performance. Given the near-identical chemical reactivity of AlN and ScAlN, uncontrolled etching risks over-etching and damaging the ScAlN layer. Distinct etching recipes are optimized for each material to enhance selectivity, as detailed in **Table S4**. The AlN seed layer is etched using a Cl_2-based chemistry, while the ScAlN layer employs a BCl_3-based process. In Cl_2 plasma, AlN exhibits a significantly higher etch rate than ScAlN due to the greater reactivity of the Al–N bond with Cl radicals and the higher volatility of $AlCl_3$ compared to $ScCl_3$. This inherent etch rate difference ensures natural selectivity, protecting the underlying ScAlN when the endpoint is reached.

Table S5 ICP etching parameters for AlN and ScAlN films.

Target layer	Etching gas	Gas flow rate	Chamber pressure	RF power
AlN	Cl_2	50 sccm	8 mTorr	500 W
ScAlN	BCl_3	100 sccm	5 mTorr	500 W

The etching process is monitored in situ by optical emission spectroscopy (OES) (**Fig. S10a**), where the emission signal associated with AlN reaction products remains stable during etching. Upon complete removal of the AlN seed layer and exposure of the underlying ScAlN, a sudden change in reaction chemistry causes a pronounced intensity drop, identified as the etch endpoint. This non-invasive, real-time detection enables precise termination, preventing over-etching and preserving device performance. Validation using an AlN/ScAlN test sample confirms endpoint accuracy, optical microscopy images before etching (**Fig. S10b**) show uniform contrast with clear pattern boundaries, while post-etching (**Fig. S10c**) reveals a distinct color shift due to

ScAlN exposure, confirming complete AlN removal and a smooth, damage-free surface morphology.

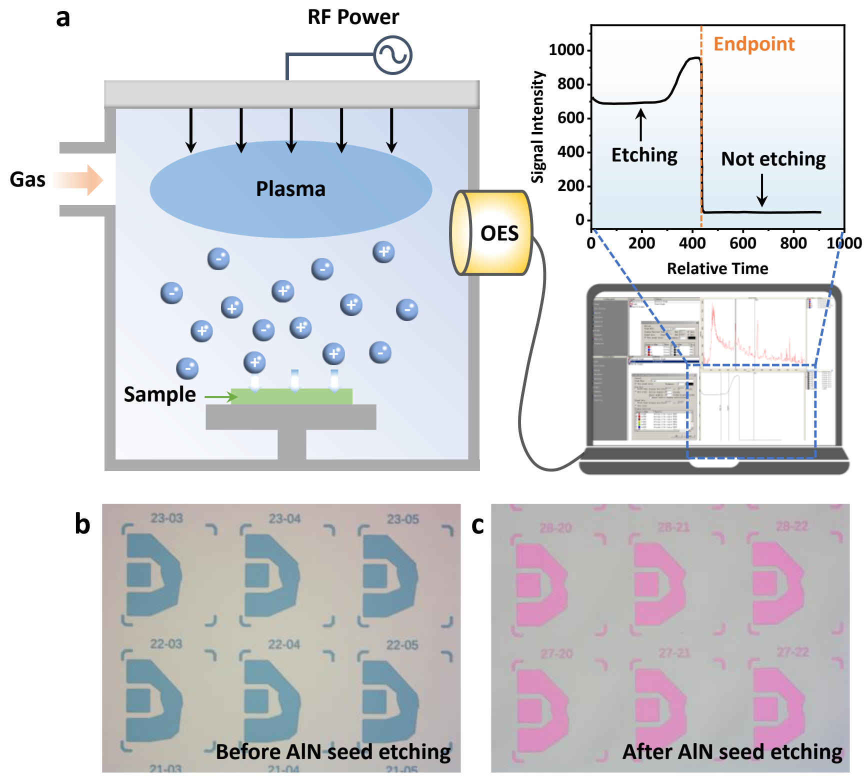

Fig. S10 The optical emission spectroscopy (OES)-based endpoint detection for AlN etching. a Schematic illustration of OES monitoring system used during the plasma etching of AlN. The RF-powered plasma generates reactive ions that bombard the sample surface, while the OES module detects the optical emission intensity of reaction products in real time. The inset shows a typical OES signal curve, where the sharp intensity drop indicates the endpoint corresponding to complete removal of the AlN seed layer. **b, c** Optical microscopy images of the MOCVD AlN seed layer before and after etching, respectively, confirming accurate endpoint control and a clean surface morphology.

j) How is the bonding process done and does the bonding process introduce stress to the multi-material stack?

Response to Reviewer:

We have now included the relevant data in the revised manuscript, with the bonding process detailed in Figs. S8 and S9 of the Supplementary Information.

(1) Wafer Preparation

After the deposition and patterning of the amorphous silicon (a-Si) sacrificial layer, a SiO_2 support layer is conformally deposited on the **device wafer**. Chemical mechanical polishing (CMP) is then performed to planarize the SiO_2 surface, ensuring intimate contact during wafer bonding. The **cap wafer** is a single-side polished silicon wafer with a thermally grown SiO_2 layer. The presence of SiO_2 on both wafers improves surface compatibility and helps suppress Au diffusion during bonding.

(2) Bonding Metal Deposition

A 200 nm-thick TiW adhesion layer is sputter-deposited on both wafer surfaces, followed by a 500 nm-thick Au bonding layer. TiW promotes adhesion to the SiO_2, while Au provides a ductile, low-resistance bonding interface.

(3) Wafer Bonding:

The two wafers are then aligned in vacuum and bonded via Au-Au thermo-compression bonding at a pressure of 100,000 N and a temperature of 350 °C for 1 h.

We acknowledge the reviewer's concern regarding residual stress from wafer bonding in multi-material stacks, primarily induced by thermal expansion mismatches and mechanical pressure causing interfacial stress concentration. To address this, our process employs three key mitigations: a low bonding temperature (350 °C) to reduce thermal stress, a ductile Au bonding layer that acts as a compliant medium to accommodate deformation, and CMP planarization ensuring uniform contact to minimize interfacial voids. SiO_2 layers on both wafers provide additional mechanical buffering. While stress evolution in such stacks remains complex, we have added a bonding schematic to the Supplementary Information for clarity and plan detailed stress distribution characterization in future work.

Revised Supplementary Information:

Wafer bonding process

Notably, wafer bonding **(Fig. S7e)** is a key step for transferring the multilayer stacks onto the cap wafer without compromising structural integrity. The process is elaborated in **Fig. S8**. Both the device wafer and the cap wafer are first coated with a TiW/Au metal stack via sputtering. A 200 nm-thick TiW adhesion layer is deposited on the planarized SiO_2 surface, followed by a 500 nm-thick Au bonding layer. The cap wafer used in this process is a single-side polished silicon wafer with a thermally grown SiO_2 layer. The presence of SiO_2 on both bonding surfaces not only provides mechanical compliance but also prevents interdiffusion of the Au layer into the underlying dielectric materials. Subsequently, the two wafers are then aligned in vacuum and bonded via Au-Au thermo-compression bonding at a pressure of 100,000 N and a temperature of 350 °C for 1 h.

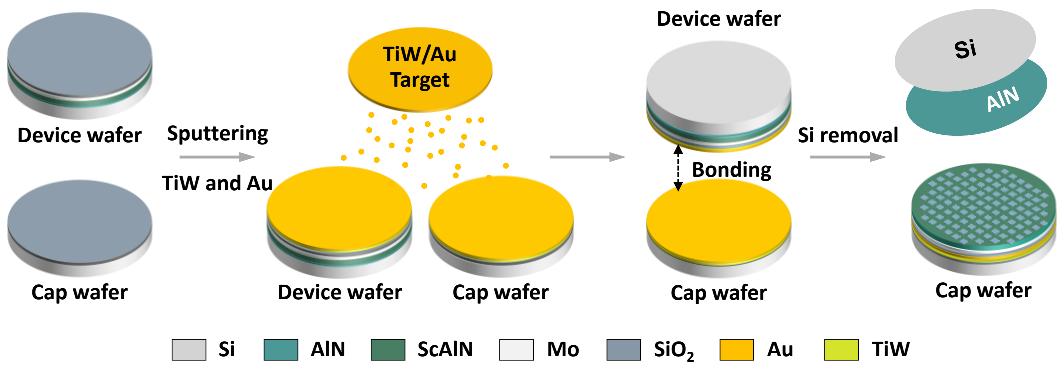

Fig. S8 Schematic illustration of the wafer bonding process.

Scanning acoustic microscopy (SAM) and cross-sectional SEM imaging evaluate the post-bonding structural quality (**Fig. S9**). The SAM map (**Fig. S9a**) reveals a generally uniform bonding interface across the wafer, with only sparse, isolated voids, some centrally located (highlighted), but no large-area delamination or continuous unbonded regions. Cross-sectional SEM (**Fig. S9b**) further confirms a well-defined, continuous Au-Au bonding interface between planarized SiO_2 layers, free of interfacial voids, warping, or distortion. After bonding, the device wafer's Si substrate is removed via dry/wet methods, and mechanical grinding thins Si to ~100 μm, followed by complete removal using HNO_3/HF mixture to expose the piezoelectric film. **Fig. S9c** shows the post-removal wafer exhibits a smooth, crack-free surface without device damage, confirming successful thin-film transfer.

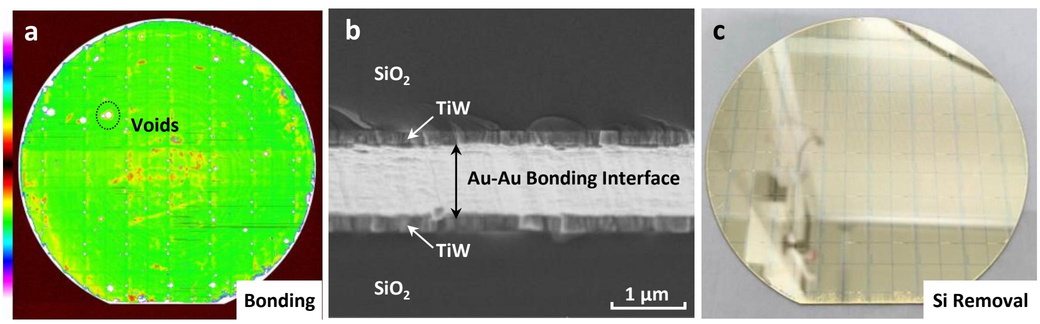

Fig. S9 Structural characterization of the thin-film transfer. a SAM image of the full bonded wafer. **b** Cross-sectional SEM image of the Au-Au bonding interface. **c** The wafer surface after Si removal.

k) In Fig. S4: The Sc concentration is 7.23 at.% in the insert, but in the figure

caption, a value of 20 at.% is stated. Please double-check.

Response to Reviewer:

The 7.23 at.% shown in the inset table of **Fig. S4** (Revised **Fig. S5** in the newly manuscript) corresponds to the atomic percentage of Sc relative to all detected elements in the EDS spectrum (including Al, N, Si, and Pt). In contrast, the "Sc concentration" given in the figure caption refers to the Sc doping level in $Sc_xAl_{1-x}N$, which we define as the fraction of Sc atoms relative to the total cations (Sc and Al) in the nitride lattice. Based on the EDS results (Al: 28.79 at.%, Sc: 7.23 at.%), the Sc doping concentration is calculated as:

$$\frac{\text{Sc at.\%}}{\text{Sc at.\%+Al at.\%}} = \frac{7.23}{7.23+28.79} \approx 20\%$$

Therefore, the stated value of 20 at.% is correct and consistent with the intended stoichiometry of $Sc_{0.2}Al_{0.8}N$. To avoid confusion, we have revised the relevant sections to explicitly describe the calculation method.

Revised Supplementary Information:

Line 233:

Energy-dispersive X-ray spectroscopy (EDS) is performed on the ScAlN film deposited on the MOCVD AlN seed layer. The measured atomic percentages were 7.23 at.% for Sc and 28.79 at.% for Al. Based on the ratio Sc/(Sc+Al), the Sc doping concentration is about 20 at.%, which is consistent with the designed composition of $Sc_{0.2}Al_{0.8}N$ (**Fig. S5h**).

l) What is the explanation that the stress state of the ScAlN on poly-AlN and single-crystalline AlN is that close (-132,7 MPa vs. -138,3 MPa), although the seed layer has completely different properties and hence, the ScAlN? What is the individual stress state of both AlN layers? The reviewer doubts that the authors can state an accuracy in the range of 0.1% in their stress measurements.

Response to Reviewer:

We thank the reviewer for the valuable comment. In this work, the reported values correspond to the residual stress of the ScAlN layer, obtained from wafer curvature measurements using the wafer state immediately after AlN seed deposition as the baseline. As the AlN seed layer is removed in the subsequent process, the reported values correspond solely to the ScAlN stress, not to the cumulative stress of the AlN/ScAlN bilayer. With identical thickness and deposition conditions, the ScAlN layers exhibit the same intrinsic properties, leading to similar stress values (−133 MPa vs. −138 MPa) as shown in the revised **Fig. S5**. Prior to this, we also measured the seed layers individually, as show in revised Figs. S4c and S4f. The average stress of the 50 nm-thick AlN deposited by PVD is about 81 MPa, while that of the 50 nm-thick AlN deposited by MOCVD reaches about 953 MPa. It can be seen that the MOCVD AlN film does exhibit higher stress, which is caused by the thermal expansion coefficient mismatch and epitaxial strain. In thicker films, this stress leads to cracking or delamination, which is why we employ only the MOCVD AlN as a template layer.

The residual stress was measured using a dual-laser wafer-curvature system (FSM FLX-500TC, Frontier Semiconductor, USA) with a typical stress resolution of ±1-2 MPa and repeatability better than ±0.5%. Stress mapping was performed along 3-6 radial scan paths intersecting at the wafer center, and the averaged value was taken as the wafer-level stress. The previously reported value (133 MPa) reflected the instrument's numerical output rather than absolute accuracy; it has been rounded to −133 MPa in the revised manuscript.

Revised Supplementary Information:

Line 190:

Residual stress mapping reveals an average stress of 81 MPa for PVD AlN (**Fig. S4c**) versus 953 MPa for MOCVD AlN (**Fig. S4f**).

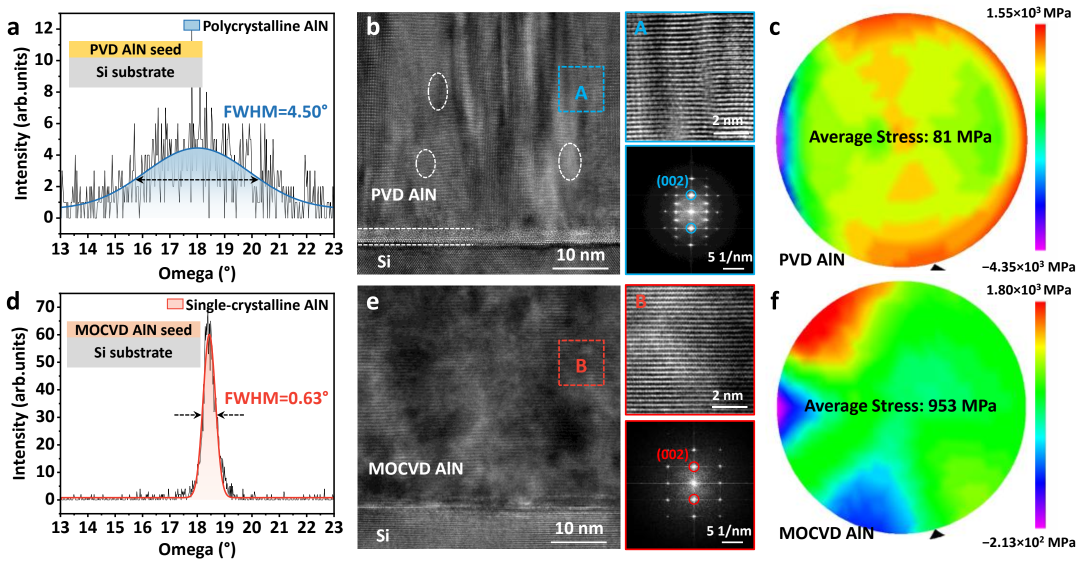

Fig. S4 c Residual stress map of the PVD AlN seed layer, with an average stress of ~81 MPa. **f** Residual stress map of the MOCVD AlN seed layer, with an average stress of ~953 MPa.…

Line 223:

The residual stress distributions of the $Sc_{0.2}Al_{0.8}N$ films on different AlN seed layers (PVD and MOCVD) are shown in **Figs. S5f** and **S5g**, exhibiting compressive stress profiles with good uniformity across the wafer for both samples. The average stress values are −133 MPa for the film grown on the PVD AlN seed layer and −138 MPa for that on the MOCVD AlN seed layer.

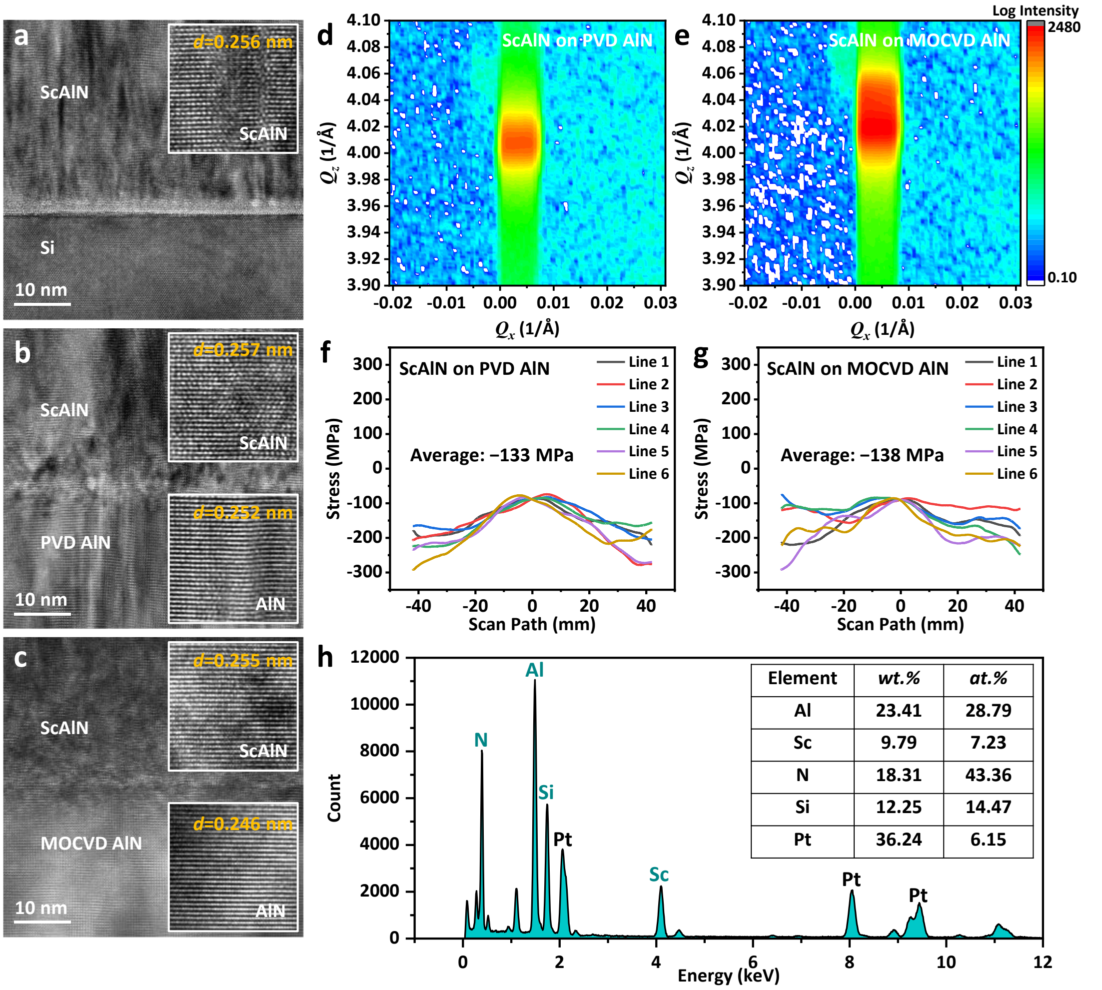

Fig. S5. **f, g** Residual stress map of $Sc_{0.2}Al_{0.8}N$ on (**f**) PVD AlN seed layer and (**g**) MOCVD AlN seed layer, with an average stress of −133 MPa and −138 MPa, respectively.